Physics Reports 1189 (2026) 1–49

Contents lists available at ScienceDirect

Physics Reports

journal homepage: www.elsevier.com/locate/physrep

Review article

Rosetta stone of neural mass models

Francesca Castaldo [a,d,*,1], Raul de Palma Aristides [b], Pau Clusella [c], Jordi Garcia-Ojalvo [b], Giulio Ruffini [a,d,1]

[a] Neuroelectrics, Barcelona, Spain
[b] Universitat Pompeu Fabra, Barcelona, Spain
[c] Universitat Politècnica de Catalunya, Barcelona, Spain
[d] Barcelona Computational Foundation, Barcelona, Spain

ARTICLE INFO

Article history:
Received 26 November 2025
Received in revised form 14 May 2026
Accepted 26 May 2026

Editor: Stefano Boccaletti

Keywords:
Computational neuroscience
Neural mass models
Brain oscillations
Dynamical systems
Whole-brain modeling
Harmonic oscillator
Stuart Landau oscillator
Wilson & Cowan model
Jansen–Rit model
Hopf bifurcation

ABSTRACT

Brain dynamics dominate every level of neural organization — from single-neuron spiking to the macroscopic waves captured by functional magnetic resonance imaging (fMRI), magnetoencephalography (MEG), and electroencephalography (EEG) — yet the mathematical tools used to interrogate those dynamics remain scattered across a patchwork of traditions. Neural mass models (NMMs) (aggregate neural models) provide one of the most popular gateways into this landscape, but their sheer variety — spanning lumped parameter models, firing-rate equations, and multi-layer generators — demands a unifying framework that situates diverse architectures along a continuum of abstraction and biological detail. Here, we start from the idea that oscillations originate from a simple push–pull interaction between two or more neural populations. We build from the undamped harmonic oscillator and, guided by a simple push–pull motif between excitatory and inhibitory populations, climb a systematic ladder of detail. Each rung is presented first in isolation, next under forcing, and then within a coupled network, reflecting the progression from single-node to whole-brain modeling. By transforming a repertoire of disparate formalisms into a navigable ladder, we hope to turn NMM choice from a subjective act into a principled design decision, helping both theorists and experimentalists translate between scales, modalities, and interventions. In doing so, we offer a *Rosetta Stone* for brain oscillation models—one that lets the field speak a common dynamical language while preserving the dialectical richness that fuels discovery.

Contents

* Corresponding author.
E-mail addresses: francesca.castaldo@neuroelectrics.com (F. Castaldo), giulio.ruffini@neuroelectrics.com (G. Ruffini).
[1] Equal contribution.

https://doi.org/10.1016/j.physrep.2026.05.004

List of abbreviations

AIT	Algorithmic information theory
AMPA	α-amino-3-hydroxy-5-methyl-4-isoxazolepropionic acid (receptor)
BOLD	Blood-oxygen-level-dependent (signal)
CSD	Current source density
DBS	Deep-brain stimulation
DCM	Dynamic causal modeling
DDE	Delay differential equation
DHO	Damped harmonic oscillator
dMRI	Diffusion MRI
DMF	Dynamic mean-field (model, Wong–Wang/Deco)
E–I	Excitatory–inhibitory (population motif)
EC	Effective connectivity
EEG	Electroencephalography
EIF	Exponential integrate-and-fire (neuron)
ERP	Event-related potential
FC	Functional connectivity
FCD	Functional connectivity dynamics
fMRI	Functional magnetic resonance imaging
GABA	γ-aminobutyric acid (receptor)
HFO	High-frequency oscillation
HH	Hodgkin–Huxley (model)
HWHM	Half-width at half-maximum
ING	Interneuron gamma (mechanism)
JR	Jansen–Rit (neural mass model)
LaNMM	Laminar neural mass model
LFP	Local field potential
LIF	Leaky integrate-and-fire (neuron)

MEG	Magnetoencephalography
M/EEG	Magneto- and electroencephalography
MOM	Metastable oscillatory mode
MOU	Multivariate Ornstein–Uhlenbeck (process)
MPR	Montbrió–Pazó–Roxin (mean-field reduction)
MRI	Magnetic resonance imaging
MSF	Master stability function
NMDA	N-methyl-D-aspartate (receptor)
NMM	Neural mass model
NMM1	First-generation neural mass model (second-order synapses, static sigmoid)
NMM2	Next-generation neural mass model (exact mean-field, dynamic (r, v) relation)
ODE	Ordinary differential equation
OU	Ornstein–Uhlenbeck (process)
PDE	Partial differential equation
PING	Pyramidal–interneuron gamma (mechanism)
PSD	Power spectral density
PSP	Postsynaptic potential
PV	Parvalbumin (interneuron type)
QIF	Quadratic integrate-and-fire (neuron)
RG	Renormalization group
RNG	Random number generator
SC	Structural connectivity
SDDE	Stochastic delay differential equation
SDE	Stochastic differential equation
SEEG	Stereo-electroencephalography
SL	Stuart–Landau (oscillator/Hopf normal form)
SOM	Somatostatin (interneuron type)
tACS	Transcranial alternating-current stimulation
tDCS	Transcranial direct-current stimulation
tES	Transcranial electrical stimulation
TMS	Transcranial magnetic stimulation
TVB	The Virtual Brain (simulator)
VIP	Vasoactive intestinal peptide (interneuron type)
WILCO	Wilson–Cowan (model)

1. Introduction

> "*Understanding is the ability to see one thing in many ways.*"
> —R. P. Feynman

Neural oscillations span every measurable scale, from subthreshold membrane resonances to the rhythms recorded by MEG/EEG and fMRI. While these dynamics may reflect critical computational roles or pathological signatures, bridging such empirical observations with a heterogeneous theoretical landscape remains a practical challenge.

Mathematical neural mass models (NMMs) provide a coarse-grained, biophysically informed description of population dynamics that bridges microcircuit mechanisms with macroscopic signals and enables principled inference and prediction. In this context, a "neural mass" refers to a "lumped", zero-dimensional representation in space: each region or circuit is summarized by a small set of population-averaged state variables, often (but not always) expressed in a firing-rate format.

A mass is associated with a single point in space — or, more commonly in whole-brain modeling, with a parcel of a brain parcellation that stands in for an extended cortical or subcortical region. The whole brain is then represented as a discrete network of such point-like masses, with anatomical connectivity encoded in their pairwise couplings. When continuous spatial variation is required — for example, traveling waves, cortical patterning, or laminar gradients — this discrete description generalizes to neural field models [1,2]. The discrete parcel indices are replaced by a continuous spatial coordinate, and the finite system of ordinary differential equations (ODEs) becomes a partial differential equation (PDE; or integro-differential equation) in space and time.

Earlier syntheses have shaped the field from complementary angles: Ermentrout (1998) [3] emphasized spatiotemporal pattern formation; Ashwin et al. (2016) [4] surveyed oscillatory network dynamics and phase-reduction perspectives. In parallel, however, connectome-based whole-brain modeling has become a standard way to link anatomy, delays, and neuroimaging observables [2,5–9], and recent exact mean-field reductions have begun to connect spiking-network models directly to low-dimensional mass equations. As a result, many scientists now move between oscillator normal forms, rate-based neural masses with explicit synaptic filtering/transfer functions, and exact spiking-to-mass reductions — without a shared notation in which the moves compose.

Links between these formalisms exist across the literature, but they are scattered and often use different conventions for coupling, forcing, and biological interpretation. The goal of this review is to provide a practical Rosetta Stone: a scoped, step-by-step mapping that starts from canonical oscillator theory and shows how successive modeling choices — damping, forcing, nonlinear saturation, synaptic filtering, and transfer functions — lead to the neural mass models most commonly used in large-scale brain modeling. Our aim is to provide a coherent "ladder" that (i) makes assumptions explicit, (ii) standardizes how exogenous inputs and inter-areal coupling enter at the node level, and (iii) offers concrete instructions for assembling and interpreting connectome-coupled network models and their perturbational responses.

We emphasize the limited scope of this exercise. The mappings we provide are *local* bridges: explicit reductions valid near specific bifurcations (typically Hopf), under specific limits (weak coupling, strong attraction, exact mean-field), or under specific structural assumptions (current-based coupling, identical populations). This review is not an exhaustive survey, and we do not propose a single global theory unifying all neural mass formalisms across all parameter regimes. Local bridges between models already exist in the literature but are obscured by mismatched conventions; a step-by-step walk across model space — in a single shared notation, with the assumptions of each bridge made explicit — turns these scattered equivalences into practical translation rules.

To this end, the paper's structure mirrors a spiral curriculum: each incremental step in model complexity is introduced first in its isolated, single-mass form and subsequently generalized to the networked or coupled scenario essential for whole-brain modeling. Key coupled equations are highlighted in light gray boxes.

We begin with the undamped harmonic oscillator — the archetype of pure phase dynamics — and sequentially introduce dissipation, external forcing, and nonlinearities. We emphasize how a basic push–pull motif underlies its oscillatory dynamics. This systematically leads us to the Stuart–Landau oscillator (SL), whose characteristic cubic nonlinearity delivers amplitude regulation with robust limit-cycle behavior. From this pivotal point, we pause to discuss some basic elements needed to establish firm connections with biology: synapses, which transform and delay signals arriving at populations, and transfer functions, which shape the response of accumulated synaptic perturbations into output firing rates. With this at hand, we jump to the Wilson–Cowan (WILCO) model, which provides a limit cycle linking back to the Hopf bifurcation in the SL model. Here we (typically) interpret abstract amplitude and phase coordinates as firing rates with biologically meaningful excitatory–inhibitory (E–I) population interactions, with the transfer function being the dynamical element. Second-order synaptic filters with static transfer functions naturally yield more nuanced models focusing on the dynamics of post-synaptic potentials, such as the Jansen–Rit and laminar neural-mass families (NMM1). This class of models can reproduce empirically observed alpha–gamma oscillatory interactions and respond realistically to physiological and pharmacological interventions. At each step a shared push–pull dynamical structure recurs, recognizing it across formalisms is what makes the cross-walk possible. Finally, we discuss next-generation neural mass models that can be derived exactly from spiking-network limits under mean-field assumptions — building on earlier exact macroscopic descriptions for theta-neuron networks and exemplified by the Montbrió–Pazó–Roxin reduction for quadratic integrate-and-fire (QIF) neuron populations — and we use this class (NMM2) to show how "dynamic" transfer functions arise from microscopic spiking mechanisms [10–12]. Beyond this lineage, the conductance-based, propagation-speed, decision-circuit, and dynamic causal modeling families listed in block (B) of Table 1.1 each sit at a one-step extension of the rate/PSP lineage; we credit them but do not re-derive them in detail.

1.1. Key concepts

We collect here the definitions used throughout the paper.

1. **Neurons, synapses, mesoscale.** We focus throughout on the *mesoscale*, or "lumped", description. Motivated by experimental measures like Local Field Potentials (LFPs) which aggregate activity over space, we replace the state of individual cells with variables representing the statistical mean of the population [13,14]. In this framework: (a) input spikes become a continuous *average firing rate* input (spikes per second). (b) synaptic dynamics act as a linear low-pass filter, smoothing average inputs into an *average membrane potential* perturbation. (c) the sharp firing threshold of single neurons is smoothed by population heterogeneity and timing (variance in thresholds and states, event timing), resulting in a continuous, non-linear *sigmoid transfer function* that maps average membrane potential to an output average firing rate (see Fig. 1.1).

2. **Computational modeling concepts**

   (a) **Neural mass vs. neural field.** A *neural mass model* is a *lumped* (point) description of a neuronal population (e.g. a cortical column, parcel, or nucleus), in which the collective activity of many neurons is summarized by a finite set of population-averaged state variables. These variables may represent firing rates, mean membrane potentials, synaptic currents, or other mesoscopic quantities, and are typically governed by low-dimensional ordinary differential equations (ODEs), stochastic differential equation (SDEs) or, when propagation delays are retained, delay differential equations (DDEs). A *neural field model* is the spatially continuous counterpart, in which the same variables depend on position and interact through spatial kernels or PDE/integral operators [2]. Both masses and fields can be rate-based, voltage-based, conductance-based, or derived as mean-field

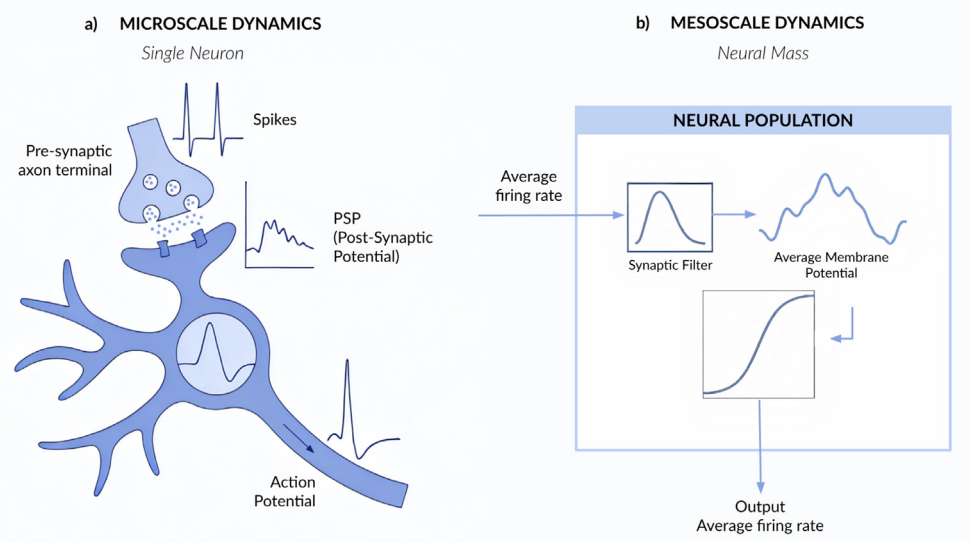

Fig. 1.1. The transition from microscopic physiology to mesoscale modeling. Left: Discrete spiking dynamics of a single neuron. Right: Continuous rate-based dynamics of a neural mass, where the sigmoid function replaces the hard firing threshold.

limits of spiking networks; thus, *mass* should be understood as *lumped vs. spatially extended*, not as a synonym for *rate*. We use a two-variable (x, y) representation as the minimal autonomous system that supports oscillation. Real neural mass models are typically higher-dimensional; the (x, y) pair is the recurring rotational sub-block, not a model in itself.

In this review, the concept of "neural mass model" is used in two related but distinguishable ways in the literature. In the Wilson–Cowan/Freeman / Lopes da Silva/Jansen–Rit/Wendling / laminar neural mass model (LaNMM) lineage, and in its exact next-generation extension by Montbrió, Pazó & Roxin (MPR/NMM2), "neural mass" is the family name of a specific modeling tradition: lumped population descriptions written in terms of firing rates and/or post-synaptic potentials, with current-based synaptic interactions through linear filters, and a population-level transfer relation linking input current to output firing rate. Within this tradition the transfer relation may be a static sigmoid (Jansen–Rit, Wendling, LaNMM), a dynamically filtered sigmoid (Wilson–Cowan, where the firing rate evolves through $\tau_m \dot{r} = -r + \varphi(I)$), or an exact dynamical (r, v) relation derived from the spiking microscale (MPR/NMM2). In the dynamical-systems and mathematical-neuroscience traditions, by contrast, "neural mass" simply means *lumped* (as opposed to *neural field*, spatially extended), and the term covers any zero-dimensional population description regardless of whether its dynamical variables are firing rates, mean voltages, conductances, or order parameters of an exact spiking-network reduction, and regardless of whether synaptic interactions are current- or conductance-based. Under this broader definition, the Liley conductance-based mean-field [15], the Robinson corticothalamic propagation model [16,17], the Wong–Wang/Dynamic-Mean-Field reduction [18,19], and the David–Friston canonical microcircuit [6] are all neural mass models. We adopt this broader (lumped-vs.-field) definition throughout the review. The derivations and cross-walks that follow, however, concentrate on the current-based rate/PSP lineage and its exact next-generation reduction, because that is the sub-family within which the chain of dynamical equivalences — phase oscillator ↔ damped oscillator ↔ Stuart–Landau ↔ Wilson–Cowan ↔ NMM1 ↔ NMM2 — is tightest, and where a unified notation yields the most leverage. The conductance-based, propagation-speed, decision-circuit, and dynamic causal modeling (DCM) lineages are credited in block (B) of the roadmap Table and revisited in the synthesis of Section 8, but they are not re-derived in detail here.

(b) **Oscillators and oscillations.** We use "oscillator" and "oscillation" in two related but non-identical senses. In the *dynamical-systems* sense, an oscillator is an autonomous system that supports persistent rhythmic motion, most commonly through an attracting periodic orbit (a stable limit cycle), but also through neutrally stable centers in idealized conservative models. In the *data-analysis* sense, an oscillation refers to a signal component with a dominant timescale (often visible as a narrow-band spectral peak). These notions overlap but need not coincide: for example, a damped linear focus driven by noise can produce *noise-sustained quasi-cycles* (spectral peaks without a deterministic limit cycle), whereas chaotic systems are *aperiodic* yet may still show prominent spectral structure. In algorithmic information theory terms, we would say that a signal is an oscillation if it can be efficiently compressed by exploiting its approximate periodicity. This reflects the scientific observer's perspective on modeling the phenomenon (see Appendix F for a more in-depth discussion).

Harmonic oscillators are prototypical oscillatory systems, linear and conservative models of a mass–spring system with an angular frequency and a sinusoid whose amplitude is fixed by initial conditions [20].
Limit-cycle oscillators are nonlinear and dissipative; after transients, they settle onto a stable closed orbit.

(c) A *node* is one neural mass; a *network* is a set of nodes connected by synaptic links, which can encode axonal delays and gains. Coupling just two nodes is enough for symmetry-breaking, phase locking, and collective bifurcations.

(d) **Push–pull motif as a local dynamical decomposition.** Across the models reviewed here, oscillations typically arise from an interplay between (i) a variable that tends to drive activity away from a reference state (“push”) and (ii) a variable (or process) that provides a restoring or damping effect (“pull”). In a harmonic oscillator these are displacement and momentum (or two quadrature variables); in E–I population models they correspond to excitatory and inhibitory components of the loop; in complex normal forms they appear as the real and imaginary parts of z. Importantly, in biophysically detailed *conductance-based* synapses, synaptic currents depend on the state through reversal potentials (“shunting”): the effective sign and strength of an interaction can therefore change with membrane potential. Throughout, the push–pull language should be read as an *operating-point-dependent* effective interaction (often after linearization and/or under current-based approximations), rather than as a universal, state-independent statement that “excitation always pushes” and “inhibition always pulls”.

(e) *Forcing* is any external drive that breaks the autonomy of a node: input from another node in the network (which we call *coupling* below), electrical stimulation, pharmacological modulation, sensory pulses, or broadband synaptic noise from sources not explicitly modeled. When the unforced system has a *strongly attracting* limit cycle and forcing is *weak*, its leading-order effect is typically a modulation of phase captured by a phase response curve [21]. When attraction is weak and/or forcing is strong, amplitude deviations and qualitative changes of the attractor can no longer be neglected, and a phase-only description may fail [22].

(f) *Coupling* is forcing generated by other nodes: one neural mass serves as a time-dependent drive for another. Coupling may be instantaneous or delayed, linear or nonlinear, and weak or strong. In the weak-coupling/strong-attraction regime, coupling often reduces to an effective interaction between phases (yielding generalized Kuramoto-type descriptions); outside that regime, amplitude effects (and possibly multistability) become central. External stimulation can be viewed as a degenerate form of coupling in which the “partner” signal is prescribed by the experimenter or device. [23,24].

3. Mathematical tools

(a) *Fixed points and* linear *stability.* Given a dynamical system $\dot{\mathbf{x}} = \mathbf{f}(\mathbf{x})$ with $\mathbf{x}(t) \in \mathbb{R}^n$ and $\mathbf{f} : \mathbb{R}^n \to \mathbb{R}^n$ at least continuously differentiable, a fixed point $\mathbf{x}^*$ satisfies $\mathbf{f}(\mathbf{x}^*) = \mathbf{0}$. Unless stated otherwise, “stability” in this review refers to *linear stability*: the local behavior is determined by the eigenvalues of the Jacobian $D\mathbf{f}(\mathbf{x}^*)$ (and, in delay systems, by the corresponding characteristic spectrum). A stable fixed point attracts nearby states, while an unstable one repels nearby states [25].

(b) *Hopf bifurcation (also Hopf–Andronov, HA).* A two-dimensional system can begin or cease to oscillate in four ways; we focus on HA bifurcation throughout, and refer the reader to [25–27] for the others. A Hopf bifurcation occurs when a complex-conjugate pair of eigenvalues of Df crosses the imaginary axis, exchanging the stability of a fixed point.

(c) *Differential Linear operator ($\hat{L}$):* Every synapse in the model behaves like a linear filter: it receives an incoming firing-rate trace $r(t)$ and converts it into a post-synaptic potential (PSP) $x(t)$. Written explicitly, this is a linear operation (convolution, see Appendix E)

$$x(t) = \hat{K}[r(t)], \tag{1.1}$$

or, equivalently,

$$r(t) = \hat{L}[x(t)], \tag{1.2}$$

where $\hat{K}$ is the synapse's impulse-response kernel and $\hat{L}$ the inverse operator of $\hat{K}$, $\hat{L}^{-1} = \hat{K}$. Framing the dynamics in terms of $\hat{L}$ makes the filter's gain, decay time and delay visible in a handful of coefficients and shows how the population amplifies, attenuates or phase-shifts small perturbations [25]. In the simplest push–pull oscillator, there are two such operators, one excitatory and one inhibitory; extending the network adds one $\hat{L}$ row per additional connections between populations.

(d) *Nonlinearity:* Models beyond the harmonic oscillator include nonlinear terms. They reflect the transformation of synaptic inputs into firing rates by the neuronal population. This is necessarily a nonlinear function because firing rates are bounded above and below.

(e) **Phase reduction and phase–amplitude reductions.** When a system possesses a stable limit cycle with strong attraction and is subject to weak forcing/coupling, its dynamics can often be reduced to a phase equation $\dot{\theta} = \omega +$ (interaction terms), leading to phase-oscillator networks. If amplitude excursions matter (e.g. near weak attraction, near bifurcations, or under stronger perturbations), one can extend this to phase–amplitude

Table 1.1
Coupled whole-brain node equations. Block (A) lists the canonical normal-form ladder used as the mathematical scaffold throughout this review. Block (B) lists representative whole-brain node models that are widely used in the literature but lie at one-step extensions of the rate/PSP lineage and are not re-derived here. *Shared notation:* C_{ij} structural-connectivity weights; $\tau_{ij} = d_{ij}/v$ conduction delays from tract length d_{ij} and effective conduction velocity $v \in [5, 10]$ m/s; $\hat{F}_{e;i}$ exogenous drive (see Eq. (2.12)). *Block (B) notation: Liley — $h_{a,i}$* mean cell-body potential of population $a \in \{e, i\}$ at node i, h_a^{rest} resting potential, $h_a^{\text{eq,b}}$ reversal potential at a for synapses from b, $\psi_{ab}(h_a)$ normalized shunting weight (1 at rest, 0 at reversal), $I_{ab,i}$ mean post-synaptic potential amplitude from $b \to a$, γ_{ab} inverse synaptic time constant, G_{ab} synaptic gain, $\rho_{a,i} = S(h_{a,i})$ population firing rate via sigmoid S, $p_{ab,i}$ external drive. *Robinson — ϕ_i* axonal pulse field, Q_i population firing rate, γ temporal damping rate of the propagation field ($\gamma \sim v/r$ with v axonal speed and r characteristic spatial scale), G global gain. *Reduced Wong–Wang/DMF — S_i* mean NMDA gating fraction at node i, $r_i = \phi(I_i)$ firing rate via the LIF mean-field transfer function ϕ, I_0 background current, w, J local recurrent self-coupling parameters, η_i noise. *David–Friston/DCM — $x_{i,p}$* state variable of intra-circuit population p at node i, $\mathcal{D}_a$ a second-order α-synaptic operator with kinetic rate a, g_{pq} intra-circuit gain matrix, σ sigmoidal voltage-to-rate map.

Model	Coupled node equation
(A) Normal-form ladder used as a mathematical scaffold in this review	
Phase-only (Kuramoto/undamped HO)	$\dot{\theta}_i(t) = \omega_i + G\sum_{j=1}^{N} C_{ij}\,\sin\big(\theta_j(t-\tau_{ij}) - \theta_i(t) - \varphi_{ij}\big) + \hat{F}_{e;i}(t), \quad i = 1, \dots, N.$
Linear damped oscillator network	$\dot{z}_i(t) = (\alpha_i + i\omega_i)\, z_i(t) + G\sum_{j=1}^{N} C_{ij}\big[z_j(t-\tau_{ij}) - z_i(t)\big] + \hat{F}_{e;i}(t), \quad i = 1, \dots, N.$
Stuart–Landau (Hopf) network	$\dot{z}_i(t) = (\alpha + i\omega_i)\, z_i(t) - (\gamma + i\beta)\,\lvert z_i(t)\rvert^2 z_i(t) + G\sum_{j=1}^{N} C_{ij}\big[z_j(t-\tau_{ij}) - z_i(t)\big] + \hat{F}_{e;i}(t), \quad i = 1, \dots, N.$
Wilson–Cowan (WILCO) E–I rate network	$\tau_x \dot{x}_i + x_i = \sigma_x\Big(w_{xx}x_i - w_{xy}y_i + P_{x,i} + \hat{F}_{e;i}(t) + \sum_{j\neq i} C_{ij}x_j\Big),$ $\tau_y \dot{y}_i + y_i = \sigma_y\big(w_{yx}x_i - w_{yy}y_i\big), \quad i = 1, \dots, N.$
NMM1 (second-order synapses, E–I motif)	$\hat{L}_x[x_i] = \sigma_x\Big(-w_{xy}y_i + \hat{F}_{e;i}(t) + \sum_{j\neq i} C_{ij}x_j(t-\tau_{ij})\Big),$ $\hat{L}_y[y_i] = \sigma_y\big(w_{yx}x_i\big), \quad i = 1, \dots, N,$ where $\hat{L}_\alpha = \dfrac{1}{\gamma_\alpha}\Big(\tau_\alpha^2 \dfrac{d^2}{dt^2} + 2\tau_\alpha \dfrac{d}{dt} + 1\Big).$
NMM2 (next-generation/QIF-based E–I motif)	$r_x^{(i)} = \hat{\Phi}_x\Big(C_{xx}s_x^{(i)} - C_{xy}s_y^{(i)} + \hat{F}_e^{(i)}(t) + \sum_{j\neq i} C_{ij}s_x^{(j)}\Big), \quad s_x^{(i)} = \hat{K}_x[r_x^{(i)}],$ $r_y^{(i)} = \hat{\Phi}_y\Big(-C_{yy}s_y^{(i)} + C_{yx}s_x^{(i)}\Big), \quad s_y^{(i)} = \hat{K}_y[r_y^{(i)}], \quad i = 1, \dots, N.$
(B) Other canonical whole-brain node models (listed for completeness; not derived here)	
Conductance-based/shunting mass (Liley-type) [15,28,29]	$\tau_a\, \dot{h}_{a,i} = -(h_{a,i} - h_a^{\text{rest}}) + \sum_b \psi_{ab}(h_{a,i})\, I_{ab,i}, \qquad \psi_{ab}(h_a) = \dfrac{h_a^{\text{eq,b}} - h_a}{\lvert h_a^{\text{eq,b}} - h_a^{\text{rest}}\rvert},$ $(\partial_t + \gamma_{ab})^2\, I_{ab,i} = G_{ab}\sum_{j=1}^{N} C_{ij}\,\rho_{b,j}(t-\tau_{ij}) + p_{ab,i}, \qquad \rho_{a,i} = S(h_{a,i}), \quad a, b \in \{e, i\}.$
Corticothalamic/propagation-speed model (Robinson-type) [16,17]	$\ddot{\phi}_i + 2\gamma\dot{\phi}_i + \gamma^2\phi_i = \gamma^2\Big(Q_i(t) + G\sum_{j\neq i} C_{ij}Q_j(t-\tau_{ij})\Big), \quad \tau_{ij} = d_{ij}/v.$
Reduced Wong–Wang/dynamic mean-field (DMF) node [18,19]	$\tau_s\dot{S}_i = -S_i + (1 - S_i)\gamma r_i, \quad r_i = \phi(I_i), \quad I_i = I_0 + wJS_i + G\sum_{j\neq i} C_{ij}S_j(t-\tau_{ij}) + \eta_i(t).$
David–Friston/DCM neural mass (canonical microcircuit family) [6]	$\mathcal{D}_{a_p}[x_{i,p}] = \sum_q g_{pq}\,\sigma(x_{i,q}) + \sum_{j\neq i} C_{ij}\,\sigma(x_{j,q}(t-\tau_{ij})), \qquad \mathcal{D}_a = \dfrac{d^2}{dt^2} + 2a\dfrac{d}{dt} + a^2.$

descriptions (e.g. phase–isostable reductions) that retain the leading amplitude modes in addition to phase. We will point out, as models become more biophysical, when phase-only reductions are appropriate and when full-state (amplitude-including) descriptions are required (see Fig. 1.2).

2. Linear response and phase-only limits

Linear and phase-only descriptions are a natural starting point in any physics-oriented review of neural mass models, for three concrete reasons. First, networks of linear (or linearized) damped oscillators admit closed-form expressions for stationary covariances, lagged covariances, and power spectra in terms of the Jacobian and the connectome, yielding analytic predictions for empirical observables — functional connectivity (FC), MEG/EEG power spectral densities — that are routinely fitted to data [30,31]. Second, every nonlinear neural mass model introduced later in this review (Stuart–Landau, Wilson–Cowan, NMM1, NMM2) reduces near a stable focus to a linear damped oscillator, so the present section supplies the universal local description that subsequent models inherit. Third, the linear network on a connectome is the natural setting for graph-spectral and connectome-harmonic decompositions, in which the dynamics diagonalize in

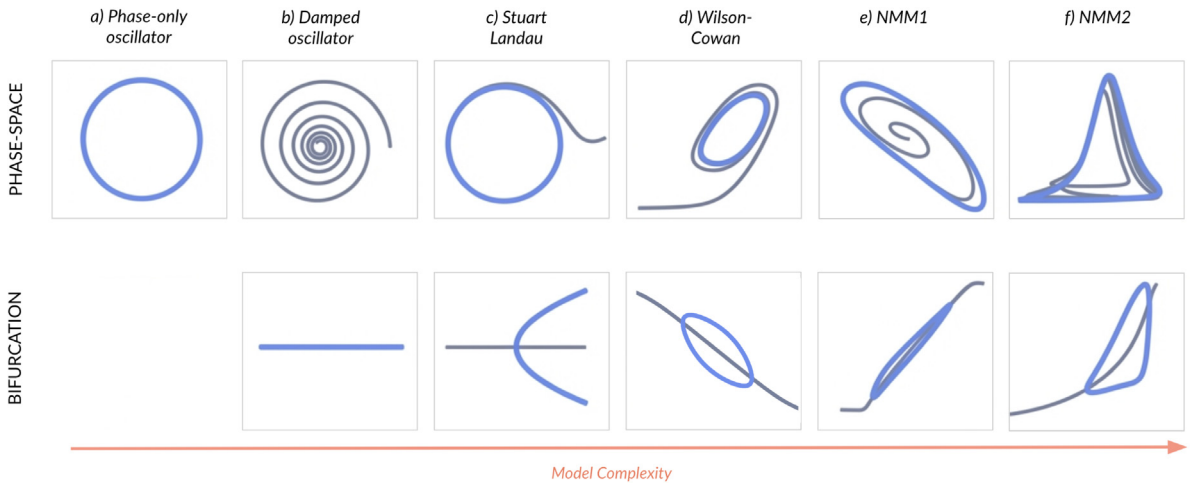

Fig. 1.2. Oscillatory dynamics across increasing model complexity. Top row: phase-space portraits. Bottom row: qualitative one-parameter bifurcation diagrams. The horizontal arrow indicates increasing model complexity from left to right. Blue traces highlight attracting (or neutrally stable) periodic orbits and their stable cycle branches; gray traces denote unstable invariant sets and illustrative transients. Panels: (a) phase-only oscillator (no amplitude dynamics); (b) damped oscillator with a globally attracting fixed point; (c) Stuart–Landau oscillator (SL) where a Hopf bifurcation creates a stable limit cycle; (d) Wilson–Cowan (WILCO) *E–I* model with coexistence of equilibria and oscillations; (e–f) two neural-mass models (NMM1, NMM2) showing parameter-dependent onset and growth of oscillations and possible bistability. Sketches are schematic and not to scale.

the eigenbasis of the connectivity Laplacian and link directly to large-scale brain modes observed in MEG/EEG [32]. At its core, an oscillation requires (i) at least two dynamical variables — or one complex variable whose real and imaginary parts exchange "energy" or activity, pushing or pulling on the another — and (ii) a mechanism to rotate or cycle continuously through phase space. The simplest realization of these requirements is the undamped, phase-only oscillator, in which a single phase variable advances uniformly while the amplitude remains fixed. This phase reduction is itself an explicit modeling choice — valid under weak forcing and strong attraction to a limit cycle — and serves throughout this review as the pedagogical starting point onto which damping, external forcing, and nonlinear amplitude dynamics are progressively grafted [33,34].

2.1. Undamped (phase-only) oscillator

The basal mechanism leading to oscillations in the activity of neuronal populations relies on the interplay between two subpopulations of neurons, one of them inhibitory and the other excitatory. We can represent the activity of these two populations by two variables $x(t)$ and $y(t)$, respectively. In the simplest description, we can assume that x decreases y linearly, whereas y increases x also linearly. Assuming that the proportionality coefficient is the same in the two cases, we obtain a simple set of two coupled linear differential equations:

$$\dot{x} = -\omega y, \tag{2.1}$$

$$\dot{y} = \omega x. \tag{2.2}$$

Defining

$$x = r\cos\theta, \qquad y = r\sin\theta, \tag{2.3}$$

one obtains directly a rescaled model in *polar form*:

$$\dot{\theta} = \omega, \tag{2.4}$$

$$\dot{r} = 0. \tag{2.5}$$

This is simply a phase (undamped) oscillator with natural angular frequency $\omega > 0$, which in our case determines the synaptic/membrane time constants of the populations. From (2.4)–(2.5) we immediately obtain $\theta(t) = \omega t + \theta(0)$, while $r(t) = r(0)$. Thus this system is characterized by a constant (conserved) amplitude $r(t) \geq 0$ and a linearly advancing phase $\theta(t) \in \mathbb{R}$.

Eqs. (2.1)–(2.2) provide the fundamental *push–pull motif* underlying oscillations in all our models: whenever y is positive, it drives $\dot{x}$ negative, acting like an inhibitory force on x; when y becomes negative, the sign flips and x is driven upward, as if released from inhibition into excitation. In turn, a positive x pushes $\dot{y}$ upward — exciting y — while a negative

x pulls $\dot{y}$ downward, inhibiting y. This continuous alternation of "push" and "pull" ensures that neither variable drifts off balance: instead, they chase each other around in a perfect circle of constant amplitude.

Introducing the complex variable

$$z = x + i\,y = r\,e^{i\theta}, \tag{2.6}$$

one finds

$$\dot{z} = \dot{x} + i\,\dot{y} = (-\omega\,y) + i\,(\omega\,x) = i\,\omega\,(x + i\,y) = i\,\omega\,z, \tag{2.7}$$

so that

$$\dot{z} = i\,\omega\,z. \tag{2.8}$$

Its solution is $z(t) = z(0)\,e^{i\,\omega\,t}$, from which r and θ can be determined.

2.1.1. Effect of forcing

To illustrate the effect of a tonic drive (deterministic or stochastic), we augment the undamped oscillator (2.8) with a complex forcing term $F(t)$. First, consider a constant $F \in \mathbb{C} = F_x + iF_y$:

$$\dot{x} = -\omega\,y + F_x, \tag{2.9}$$

$$\dot{y} = \omega\,x + F_y. \tag{2.10}$$

A purely real F produces a DC offset $(x^*, y^*) = (-F_x/\omega, 0)$, around which the trajectory circulates (see Appendix section D.5 for more details). When $F(t)$ varies in time, Eqs. (2.9)–(2.10) describe how the instantaneous bias modulates both amplitude and phase. To see this, we note that in the complex representation,

$$\dot{z} = i\,\omega\,z + F(t), \tag{2.11}$$

the term $F(t)$ gently shifts the oscillator's center and can transiently entrain or phase-shift the trajectory without altering its underlying circular geometry (see Appendix D.5 for further details on the effects of forcing).

2.1.2. Internal and external contributions to forcing; electric fields

Forcing appears in all models, internal (from other nodes, i.e., *coupling*) or external (unmodeled nodes, neuromodulation, electric fields). We allow for the possibility of forcing to be of a stochastic nature, indicating this with a hat notation ($\hat{F}$). Next, we divide forcing contributions between internal contributions from the network model in which the node lies (g_i, which we include in models typically as *coupling*), and external to it ($\hat{F}_e$). We also separate the latter into external driving of physiological origin (f) and perturbations from an external electric field E,

$$\hat{F}(t) = g_i(t) + \hat{F}_e(t) \tag{2.12}$$

$$\hat{F}_e(t) = f(t) + \Lambda[\vec{E}(t)] + \hat{\eta}(t) \tag{2.13}$$

where Λ is some operator or function of the electric field. Thus, we will normally model $\hat{F}_e$ as a sum of a deterministic component f — typically from inputs from external populations and an electric field contribution from transcranial electrical stimulation (tES), transcranial magnetic stimulation (TMS) or deep brain stimulation (DBS), for example —, and an additive zero-mean stochastic contribution to forcing $\eta(t)$.

For example, in the case of weak electric fields at low frequencies (*transcranial electrical stimulation* or tES), the contribution from the electric field is of the form,

$$\Lambda[\vec{E}] = \vec{\lambda} \cdot \vec{E}(t) \tag{2.14}$$

Here, the electric field effect is linear through a vectorial coupling constant ($\vec{\lambda}$) and captures ensuing membrane perturbations [35–39].

We will use the notation in Eq. (2.12) in the following sections, adding a node index if needed (i.e., $\hat{F}_{e;i}$ for the forcing on node i).

2.1.3. Network of undamped harmonic oscillators

Here, we provide the general coupled network model and show how it connects to the Kuramoto model presented below. Following the additive forcing model for coupling, the equation for a network of oscillators is

$$\dot{z}_i(t) = i\,\omega_i\,z_i(t) \;+\; \sum_{j\neq i}^{N} C_{ij} z_j(t), \qquad i = 1, \ldots, N. \tag{2.15}$$

To connect the coupled linear oscillator network in (2.15) with a phase-only description, we write each state in polar form

$$z_i(t) = r_i(t)\,e^{i\theta_i(t)}. \tag{2.16}$$

Substituting into (2.15) and separating real and imaginary parts yields coupled equations for amplitudes and phases. With $C_{ij} = |C_{ij}|\, e^{i\varphi_{ij}}$, the amplitude dynamics read

$$\dot{r}_i \;=\; \sum_{j\neq i} |C_{ij}|\, r_j\, \cos\!\big(\theta_j - \theta_i + \varphi_{ij}\big)\,, \tag{2.17}$$

and the phase dynamics

$$\dot{\theta}_i \;=\; \omega_i \;+\; \frac{1}{r_i}\sum_{j\neq i} |C_{ij}|\, r_j\, \sin\!\big(\theta_j - \theta_i + \varphi_{ij}\big)\,, \tag{2.18}$$

which already has Kuramoto–Sakaguchi structure, but with time-dependent amplitudes $r_i(t)$. A genuine phase-only model is recovered as an explicit *reduction choice*: when the amplitudes relax to a fixed spatial profile $r_i^* > 0$ (a slow manifold approached when the linear spectrum has a single marginal mode and all others decay), the amplitude equation (2.17) sets $\dot{r}_i \to 0$ and (2.18) reduces to the constant-coupling form of Eq. (2.19) below.

A convenient way to make this connection more concrete is to add a weak uniform decay term, $\dot{z}_i = (i\omega_i - \gamma)z_i + \sum_{j\neq i} C_{ij} z_j$, and to interpret the resulting dynamics in terms of the spectrum of the linear operator [40,41]. For appropriate choices of γ and C_{ij}, all but one eigenmode decay, while a single collective mode remains marginal and rotates at a common angular frequency. In this *collective oscillation* regime, the amplitudes $r_i(t)$ relax to a fixed spatial profile $r_i^* > 0$, so that (2.18) reduces asymptotically to a genuine phase model with constant effective couplings,

$$\dot{\theta}_i = \omega_i + \sum_{j\neq i} \tilde{K}_{ij}\, \sin\!\big(\theta_j - \theta_i + \varphi_{ij}\big), \qquad \tilde{K}_{ij} = |C_{ij}|\,\frac{r_j^*}{r_i^*}. \tag{2.19}$$

This construction shows how a linear complex network with global $U(1)$ phase symmetry naturally generates a low-dimensional manifold of phase dynamics that is well captured by Kuramoto-type equations [42–44]. At the same time, the Kuramoto model is usually taken in the opposite, more general direction: as a phenomenological phase description for weakly coupled limit cycles with $U(1)$ symmetry, where the coupling matrix and coupling function are not constrained to arise from any particular underlying linear operator.

2.1.4. The Kuramoto model

The canonical model for studying collective phase dynamics is the Kuramoto model — "the hydrogen atom of synchronisation" due to its simplicity, analytical tractability, and extraordinary reach across disciplines [34,45–47].

Starting from the undamped limit cycle in Eq. (2.4), Kuramoto assumed that each oscillator interacts with all others only through the difference of their phases. For a population of N units this yields

$$\dot{\theta}_i \;=\; \omega_i \;+\; \frac{G}{N}\sum_{j=1}^{N} \sin\!\big(\theta_j - \theta_i\big), \qquad i = 1, \ldots, N, \tag{2.20}$$

where ω_i is the natural frequency of oscillator i and G is a global coupling constant.

As additional motivation of this model, the sine term is the first (and usually dominant) Fourier component of any 2π-periodic interaction function [48], and retaining only this term might capture most of the essential physics. In the classic all-to-all case with a unimodal, symmetric frequency distribution and pure sine coupling (no phase lag), increasing K past a critical value produces a continuous (second-order) transition to synchrony that is solvable exactly in the thermodynamic limit ($N \to \infty$) [49]. More generally — depending on the frequency distribution, the presence of phase-lag or higher harmonics in the coupling, and the network structure — the transition can be abrupt and hysteretic (first-order) or continuous. No other phase-only coupling law has proved as analytically transparent or universally useful.

For whole-brain simulations, we couple phases over a weighted network and include drive and noise:

$$\dot{\theta}_i(t) = \omega_i + G\sum_{j=1}^{N} C_{ij}\, \sin\!\Big(\theta_j\big(t - t_{ij}\big) - \theta_i(t) - \varphi_{ij}\Big) + \hat{F}_{e;i}(t), \qquad i = 1, \ldots, N. \tag{2.21}$$

Here $C = [C_{ij}] \in \mathbb{R}_{\geq 0}^{N\times N}$ is the connectivity matrix, $G \in \mathbb{R}_{\geq 0}$ a global coupling gain, $\omega_i \in \mathbb{R}$ the intrinsic angular frequencies, $\tau_{ij} \geq 0$ the delays, $\varphi_{ij} \in (-\pi, \pi]$ fixed phase lags, and $\hat{F}_{e;i}(t) \in \mathbb{R}$ the external forcing. In whole-brain applications, C_{ij} is most commonly estimated from diffusion magnetic resonance imaging (dMRI; tractography from white-matter streamlines) and $\tau_{ij} = d_{ij}/v$ from tract lengths d_{ij} and an effective conduction velocity $v \in [5, 10]$ m/s.

The box below summarizes the parameters of the phase-oscillator description and gives guidelines for using it to model neural populations.

Coupled Undamped Harmonic Oscillators (***Eq.*** (2.21))	
Whole-brain Simulations Parameters & Physiological Meaning	
Node i	Coarse-grained neural population (e.g., cortical/subcortical parcel or column) treated as a single phase unit.
N	*Network size*: number of regions/nodes (parcels) modeled.
x, y	Quadrature *push–pull* components of a mesoscopic E/I loop. A positive y suppresses x (inhibitory-like), negative y releases x (excitatory-like), and vice versa, sustaining rotation.
$\hat{\eta}_i(t)$	Independent standard noise sources.
G	*Global coupling gain* scaling long-range synaptic influence; proxies neuromodulatory gain/arousal effects on inter-areal drive.
C_{ij}	*Connectivity weight* from region j to i. Typically structural (white-matter tract strength or streamline count); can also be functional (FC) or effective (EC) matrices when modeling phenomenology or directed influence; synthetic graphs (all-to-all/modular/distance-decay) if data are absent.
τ_{ij}	Propagation delay along $j \to i$ (conduction + synaptic). Estimate from tract length/velocity; typical few–tens of ms.
$\omega,\ \omega_i$	*Natural angular frequency* ($f_i = \omega_i/2\pi$); reflects effective synaptic/membrane time constants of the local E/I loop.
$\theta_i(t)$	Local *phase* (population timing/excitability window) of node i.
r(const.)	Baseline *amplitude*/power envelope of the population rhythm; held fixed in the phase-only reduction. $\dot{r} = 0$ (Eq. (2.5)).
φ_{ij}	*Fixed phase-lag* (Sakaguchi offset) capturing delays/filtering at a carrier frequency; $\varphi_{ij} = 0$ recovers pure Kuramoto coupling. If using explicit τ_{ij}, set φ_{ij}=0 or use $\varphi_{ij} \approx \bar{\omega} t_{ij}$.
$\hat{F}_{e;i}(t)$	Exogenous drive (external forcing from nodes or elements outside the network or an electric field, see Eq. (2.12)).
When to Use It	
Use this when phase relations matter more than amplitudes: synchrony, phase locking, entrainment.	
Assumptions near a stable limit cycle with approximately constant power.	
Best for large networks needing analytic clarity and light compute (order parameter, clustering, locking bandwidths).	
Inputs act mainly as phase biases/periodic drives.	
Avoid if envelope dynamics, amplitude quenching, or bursty power are essential—use an amplitude–phase model.	
How to Use It	
State phases only: $\theta_i(t)$; fix amplitude $r_i = r_0$.	
Provide C (connectome): *structural* (dMRI/tractography), *functional* (empirical FC weights), or *effective* (model-based directed EC); if unavailable, use all-to-all, modular, random, or distance-decay graphs. Also set G.	
Frequencies $\omega_i \approx 2\pi f_0$ with narrow spread (or heterogeneous if desired).	
Optional delays τ_{ij} (or static phase-lags φ_{ij}), drive $\hat{F}_{e;i}(t)$ (e.g., $A_i \sin(\Omega t + \phi_i)$).	
Defaults normalize $C \leftarrow C/\lambda_{\max}$; set $\varphi_{ij} = 0$ initially; $\theta_i(0) \sim \mathcal{U}(0, 2\pi)$; $\Delta t \le 1/(50 f_{\max})$.	
Integration & reproducibility (Δt).	
With non-zero delays $\tau_{ij} > 0$ and stochastic forcing, Eq. (2.21) is a stochastic delay differential equation (SDDE), *not* an ODE/SDE. In the deterministic limit ($\eta_i \equiv 0$), we recommend a method-of-steps DDE solver with adaptive step size and continuous interpolation of the delayed history (e.g. MATLAB `dde23`, Julia `DelayDiffEq.jl`). When stochastic forcing is included, no fully standard SDDE solver is universally adopted; in practice we use a fixed-step Euler–Maruyama scheme on the delayed system as a controlled approximation, with the following caveats: (i) the discretization is piecewise-constant (or piecewise-linear) noise on each step; (ii) delayed states are recovered from a circular history buffer with linear interpolation when $\tau_{ij}/\Delta t \notin \mathbb{Z}$; (iii) the step size must satisfy both the oscillation-resolution bound $\Delta t \le 1/(50 f_{\max})$ *and* the delay-resolution bound $\Delta t \le \min_{ij} \tau_{ij}/10$, with convergence verified by halving Δt and checking statistical observables.	
Reporting. For reproducibility, fix and report: solver name and version, the SDDE discretization scheme (noise model and interpolation), Δt, total simulated time, discarded transient length, and the seed of the random number generator.	
Readouts order parameter $Z(t) = \frac{1}{N}\sum_j e^{i\theta_j(t)}$, report $\langle \lvert Z \rvert \rangle$; synthesize $x_i(t) = r_0 \cos\theta_i(t)$ if needed.	

2.1.5. Applications

Historically, the phase-oscillator framework grew out of Winfree's program in theoretical biology, which showed how large populations of weakly coupled limit-cycle oscillators with heterogeneous natural frequencies could synchronize and be reduced to phase dynamics [50]. Kuramoto then analyzed an idealized continuum limit with sinusoidal coupling, deriving a closed mean-field description via a complex order parameter and predicting a continuous transition from desynchrony to partial synchrony [51]. His 1984 monograph consolidated the theory and notation used today, and later

Throughout this review, references to "alpha," "gamma," and other named rhythms follow the standard EEG/MEG band conventions:

δ **(1–4 Hz)** Slow-wave activity; dominant during deep (non-REM stage 3) sleep and unconsciousness; cortico-thalamic origin.

θ **(4–8 Hz)** Drowsiness, memory encoding, navigation; prominent in hippocampus and medial temporal lobe.

α **(8–13 Hz)** Relaxed wakefulness with eyes closed, posterior dominance; thalamo-cortical generator (Adrian–Berger rhythm).

β **(13–30 Hz)** Active cognition, sensorimotor processing; modulated by movement preparation.

γ **($\gtrsim$ 30 Hz, often 30–80 Hz)** Local cortical computation, feature binding; pyramidal–interneuron gamma (PING)/interneuron gamma (ING) interneuronal mechanisms.

The boundaries are conventional and vary slightly across the literature. We refer back to this box whenever a specific band is invoked in subsequent sections.

Box 2.1. EEG/MEG frequency bands.

expositions placed the model as a paradigm for collective synchronization across physics, chemistry, and neuroscience [42,52,53].

Kuramoto-type networks have become ubiquitous in computational neuroscience, appearing in everything from large-scale *cortex-as-a-graph* models that reproduce zero-lag synchrony, realistic blood-oxygen-level-dependent (BOLD) fluctuations, and structured MEG amplitude envelopes [5,54–56] to theories of how rhythmic sensory inputs entrain cortical circuits at the level of individual columns [57]. This popularity stems from the model's tight mapping to neural ingredients: each oscillator's intrinsic frequency ω_i can represent the diverse frequency content of cortical rhythms, and the coupling constant G collects the net gain of synaptic (as well as ephaptic or subcortical) interactions among neurons or brain regions. At the macroscopic scale, the emergence of phase coherence provides a principled analogue of the global signals captured by EEG/MEG [54,58].

As coupling increases, heterogeneous oscillators undergo a transition from desynchrony to partial synchrony [51,53], offering a mechanistic lens on how large-scale neural oscillations (e.g., alpha) can arise gradually as effective interactions strengthen. Within connectome-constrained implementations, this framework has clarified how zero-lag synchrony can occur across distant cortical areas, how hubs facilitate inter-modular coordination, and how network activity explores metastable, clustering regimes that wax and wane over time [59–62].

The same phase-only formalism is well suited to external drive: because inputs enter as phase biases, periodic stimulation can lock phases over predictable bandwidths, accounting for stimulus-locked entrainment and phase-reset phenomena in EEG/MEG [57]. This logic extends beyond the cortex—for example, circadian networks in the suprachiasmatic nucleus are naturally captured as forced phase-oscillator ensembles [63].

To bridge toward biological realism, neuroscience variants relax idealizations by introducing sparse/weighted structural connectomes, heterogeneous propagation delays, stochasticity, and higher-harmonic couplings. These "realism knobs" generate chimeras (coexistence of synchronized and desynchronized populations), metastable clustering, and frequency-dependent phase-lag structure—while retaining a tractable phase core [60,61,64–66]. Importantly, when these extras are set to zero, the models reduce to the canonical Kuramoto equation, preserving interpretability and analytical leverage.

Finally, the phase-only reduction is biologically insightful because many cortical E/I loops operate near a limit cycle, so the theory cleanly separates *when* a population fires (phase) from *how strongly* it fires (amplitude). This turns questions about perception, attention, communication-through-coherence [67], and intervention into questions about phase alignment and effective coupling—precisely the levers neuromodulators and stimulation can adjust. In practice, Kuramoto-type reductions have informed control strategies in deep-brain stimulation and desynchronization therapies [68–71], and physiologically motivated variants link coupling and phase shifts to transmitters and hemodynamics [72]; related approaches have begun to quantify coupling abnormalities in clinical cohorts [73].

2.2. Damped harmonic oscillator (DHO)

Introducing a real damping coefficient α ($\alpha < 0$ for decay, $\alpha > 0$ for growth) into Eq. (2.5) (*unforced* case) the equations of motion become

$$\dot{r} = \alpha\, r, \tag{2.22}$$

$$\dot{\theta} = \omega. \tag{2.23}$$

which, in Cartesian coordinates, reads

$$\dot{x} = -\omega\, y + \alpha\, x, \tag{2.24}$$

$$\dot{y} = \quad \omega\, x + \alpha\, y. \tag{2.25}$$

The fundamental "push–pull" interaction between x and y persists in the damped case: the term $-\omega\, y$ continues to inhibit (or disinhibit) x exactly as in the undamped case, while $\omega\, x$ drives y. On top of this reciprocal coupling, each variable now experiences its own leakage (if $\alpha < 0$) or intrinsic amplification (if $\alpha > 0$) through the terms αx and αy. As a result, the two-node loop still chases its 90° phase offset, but gradually spirals inward under leak or outward under growth. This interplay — orthogonal E/I feedback combined with uniform decay or gain — captures how real neural circuits blend balanced excitation and inhibition with membrane- or synaptic-level dissipation (or recruitment), producing damped (or growing) oscillations rather than perfect, constant-amplitude rotations.

Letting $z = x + i\, y$ yields the compact complex form

$$\dot{z} = (\alpha + i\omega)\, z. \tag{2.26}$$

2.2.1. Effect of forcing

To introduce a constant (or very slowly varying) drive, one again writes

$$\dot{z} \;=\; (\alpha + i\,\omega) z \;+\; F, \quad (F \in \mathbb{C}) \tag{2.27}$$

This moves the only fixed point of the system from $z^* = 0$ to

$$z^* \;=\; -\,\frac{F}{\alpha + i\,\omega}. \tag{2.28}$$

From the linear stability analysis, trajectories spiral into (for $\alpha < 0$) or out of (for $\alpha > 0$) the off-center equilibrium z^* (see details in Appendix A). In polar coordinates (see Eqs. (2.22)–(2.23)), $\mathrm{Re}[F\, e^{-i\theta}]$ can exactly balance the leakage term αr. A constant real F_x ensures that $x(t)$ does not decay to zero, mirroring how a steady current injection holds a neuron at a depolarized potential. More generally, time-dependent $F(t)$ encodes transient pushes and pulls that can transiently boost amplitude, shift phase, or perturb the equilibrium away from its natural damped focus—preparing the oscillator for subsequent coupling effects in network models.

2.2.2. Coupling: Network of damped harmonic oscillators

Consider N oscillators that, when uncoupled, each satisfy

$$\dot{z} = (\alpha + i\,\omega) z + \hat{F}(t),$$

where α (real) is the common damping ($\alpha < 0$) or growth ($\alpha > 0$) rate, ω is the natural frequency, and $\hat{F}(t)$ is any external (complex-valued) input. Introducing all-to-all diffusive coupling among these units yields the network equation

$$\dot{z}_i = (\alpha + i\,\omega_i) z_i + \frac{G}{N} \sum_{j=1}^{N} \big(z_j - z_i\big) + \hat{F}_{e;i}(t), \quad i = 1, \ldots, N. \tag{2.29}$$

Here, each ω_i denotes the intrinsic frequency of node i, $G \geq 0$ is the global coupling strength, and the term $\frac{G}{N}\sum_j (z_j - z_i)$ represents a diffusive interaction that pulls each oscillator toward the network centroid $\frac{1}{N}\sum_j z_j$. Consequently, this all-to-all linear network is precisely the *linearized* limit of the Stuart–Landau network (introduced in the next section).

For whole-brain simulations in the damped regime, we place a linear resonator at each node and couple them through a weighted connectome with optional delays, additive drive, and noise:

$$\dot{z}_i(t) = \big(\alpha_i + i\,\omega_i\big)\, z_i(t) \;+\; G \sum_{j=1}^{N} C_{ij} \left[z_j\big(t - t_{ij}\big) - z_i(t) \right] + \hat{F}_{e;i}(t), \qquad i = 1, \ldots, N. \tag{2.30}$$

Here $z_i = x_i + i\, y_i$ is the complex state of node i; $\alpha_i < 0$ sets linear damping (decay time $-1/\alpha_i$) and ω_i is the intrinsic angular frequency; G is an optional global coupling gain sometimes used to fit models; $C_{ij} \geq 0$ are (possibly directed) connectome weights; $\tau_{ij} \geq 0$ are propagation delays (set $\tau_{ij} \equiv 0$ if ignored) and $\hat{F}_{e;i}(t)$ is the external forcing; Setting $\tau_{ij} \equiv 0$ and taking $C_{ij} = 1/N$ recovers the all-to-all form in Eq. (2.29).

With linear coupling and real C_{ij}, the network coupling term $C_{ij}(z_j - z_i)$ in Eq. (2.30) unpacks as

$$\dot{x}_i = \cdots + C_{ij}(x_j - x_i), \qquad \dot{y}_i = \cdots + C_{ij}(y_j - y_i),$$

i.e., the connection links push to push and pull to pull at equal strength, with no cross-talk between the push of one node and the pull of another. Allowing $C_{ij} = |C_{ij}| e^{i\iota_{ij}}$ to be complex rotates the coupling by ι_{ij} and mixes the two channels

across nodes — the Sakaguchi–Kuramoto phase-lag structure that emerges in the polar reduction (2.18), with $\iota_{ij} \approx \bar{\omega}\,\tau_{ij}$ at a carrier frequency $\bar{\omega}$ identifying the offset with a conduction delay [74]. The interpretation is mode-agnostic: (x, y) may be a pair of firing rates, a post-synaptic potential and its time derivative, or any pair of variables that play the push–pull role of the local rhythm. Linear coupling in z thus corresponds to current-based, frequency-independent inter-areal drive linearized around a stable operating point.

Coupled Damped oscillator (***Eq.*** (2.30))	
Whole-brain Simulations Parameters & Physiological Meaning	
Node i	Neural mass (parcel/column or nucleus) represented as a linear damped resonator.
N	Number of nodes (parcels).
$z_i(t) = x_i + i\,y_i$	Complex mesoscopic activity; x, y are quadrature "push–pull" components (in-phase/quadrature of a local E/I loop).
α_i	Linear damping (leak/gain). $\alpha_i < 0$ gives a stable focus with decay time $-1/\alpha_i$; reflects local E/I balance, membrane and synaptic dissipation.
ω_i	Intrinsic angular frequency (preferred local timescale); set by effective synaptic/membrane constants. $f_i = \omega_i/(2\pi)$.
G	Global coupling gain controlling the overall strength of inter-areal drive.
C_{ij}	Connectivity from region j to i (structural connectivity (SC) from tractography by default; functional/effective connectivity (FC/EC) alternatives or synthetic graphs if needed).
τ_{ij}	Propagation delay on pathway $j \to i$ (axonal conduction & synaptic latency); typically estimated as $\tau_{ij} = d_{ij}/v$ from tract length d_{ij} and an effective conduction velocity $v \in [5, 10]$ m/s; induces frequency-dependent phase offsets.
$\hat{F}_{e;i}(t)$	Exogenous drive (external forcing from nodes or elements outside the network or an electric field, see Eq. (2.12)). Complex or real valued.
When to Use It	
Use this when you want brain-scale resonance with decay (stable focus): fitting FC/covariances, lag structures, and power spectra; probing linear entrainment and susceptibility. **Assumptions** small fluctuations around equilibrium ($\alpha_i < 0$), additive noise and/or weak drive; linear coupling over the connectome (optionally with delays). **Best for** closed-form second-order statistics (covariances, cross-spectra), rapid parameter sweeps, effective-connectivity estimation, graph-spectral analyses. **Avoid** if self-sustained oscillations, limit cycles, or multistability are essential—use full Stuart–Landau/Hopf bifurcation dynamics instead.	
How to Use It	
Provide C (SC default; FC/EC or synthetic graphs if SC unavailable), G, $\alpha_i<0$, ω_i (centered on target band), optional τ_{ij}, $F_i(t)$, and $\hat{\eta}_i(t)$. **Defaults** normalize $C \leftarrow C/\lambda_{\max}(W)$; pick $\alpha_i = -1/\tau_i$ with τ_i in a plausible range; set $\tau_{ij} = 0$ initially. Integration (Δt). With non-zero delays $\tau_{ij} > 0$ and stochastic forcing, Eq. (2.30) is a stochastic delay differential equation: prefer a method-of-steps DDE solver in the deterministic limit, or use fixed-step Euler–Maruyama on the delayed system as a controlled approximation with $\Delta t \le \min\{1/(100\,f_{\max}),\ \min_{ij}\tau_{ij}/10\}$ and convergence verified by step halving (cf. the Kuramoto-box discussion above). **Readouts** stationary covariance/lagged covariance, PSD and cross-spectra; impulse/transfer functions for linear response; reconstruct $x_i(t) = \mathrm{Re}\ z_i(t)$ if a real observable is needed.	

2.2.3. Applications

Eq. (2.26) is the small-amplitude (linearized) limit of the canonical Stuart–Landau (SL) oscillator, whose full version is introduced below. In this regime, each node behaves as a damped complex oscillator whose real and imaginary parts jointly encode a local E/I loop: the real part plays the role of in-phase activity, the imaginary part the quadrature component, and the linear coefficient $\alpha < 0$ sets the decay time back to equilibrium while ω fixes the resonance frequency.

Linearity means that second-order statistics — instantaneous and lagged covariances, cross-spectra, and power spectral densities — admit *closed-form* expressions involving the Jacobian and the connectome (with optional delays), so functional connectivity and spectra follow without simulation. This is worked out explicitly for the SL whole-brain model by Ponce-Alvarez and Deco, who derive analytic formulas and show their accuracy near the stable focus [75].

Because of that tractability, the linear damped-oscillator network has become a *standard baseline* in whole-brain modeling pipelines: (i) as a linearized SL model with analytically tractable functional connectivity (FC) and power spectral density (PSD) for rapid parameter sweeps and state comparisons; (ii) as a multivariate Ornstein–Uhlenbeck (MOU) model on the connectome to fit time-shifted covariances and estimate *effective connectivity*; and (iii) as graph-spectral neural-field approximations in which connectome eigenmodes diagonalize the dynamics. Representative examples include the SL-linearization for closed-form statistics and fast grid searches [75], MOU-based estimation of directed effective connectivity from fMRI [31], and analytic graph-neural-field or spectral-graph models that link Laplacian eigenmodes

to MEG/EEG spectra and spatial patterns [76–78]. Together, these works show that much of the large-scale resting-state phenomenology of the brain can be captured by linear (or linearized) dynamics, a point underscored by systematic model-selection studies arguing that macroscopic resting-state activity is often best described by linear models [79].

Biologically, this phase-linear description retains the features most relevant at mesoscopic scales. The damping α reflects local E/I balance and neuromodulatory tone; ω captures dominant local timescales; coupling rescales long-range synaptic, ephaptic or subcortical gain; and inputs $F(t)$ represent afferents or stimulation. In this light, *stimulation* acts as designed forcing that reveals the network's linear frequency response (and hence entrainment bandwidths). In contrast, *pharmacology* primarily shifts effective gain or damping and can therefore alter susceptibility and resonance.

Stimulation and pharmacology as perturbations of the linearized focus. Linearizing any of the network models in this review around a stable focus $\mathbf{x}^*$ and writing the deviation $\mathbf{u} = \mathbf{x} - \mathbf{x}^*$ recovers the complex damped network of Eq. (2.30), $\dot{\mathbf{u}} = J\,\mathbf{u} + \mathbf{f}(t) + \boldsymbol{\xi}(t)$, with Jacobian $J = -A + i\Omega + GC$, $A = \mathrm{diag}(\alpha_i)$, $\Omega = \mathrm{diag}(\omega_i)$, and $\boldsymbol{\xi}(t)$ Gaussian white noise of covariance D. For $\mathbf{f} \equiv 0$ the stationary covariance Σ satisfies the Lyapunov equation $J\Sigma + \Sigma J^* = -D$, and the cross-spectral density factorizes through the resolvent $G(\omega) = (i\omega I - J)^{-1}$: $S(\omega) = G(\omega)\,D\,G^*(\omega)$ [30,31]. A pharmacological intervention enters as a parameter shift δJ inherited from changes in local gain/damping ($\delta\alpha_i$) and effective coupling (δC_{ij}). To first order the covariance and PSD respond as

$$J\,\delta\Sigma + \delta\Sigma\,J^* = -\big(\delta J\;\Sigma + \Sigma\;\delta J^*\big), \tag{2.31}$$

$$\delta S(\omega) = G(\omega)\big[\delta J\;\Sigma + \Sigma\;\delta J^*\big]G^*(\omega). \tag{2.32}$$

A drug that nudges a region toward Hopf shrinks the real part of the corresponding eigenvalue of J and sharpens the spectral peak as the inverse of the eigenvalue's distance to the imaginary axis; an intervention that rescales effective coupling redistributes power across modes through the eigenstructure of C. Stimulation reads the same equation with $\mathbf{f}(t)$ active. A periodic drive $\mathbf{f}(t) = \mathbf{f}_0\,e^{i\omega_s t}$ (e.g., transcranial alternating current stimulation (tACS) at carrier frequency ω_s) admits the steady-state response $\langle\mathbf{u}\rangle(t) = G(\omega_s)\,\mathbf{f}_0\,e^{i\omega_s t}$: the same resolvent that sets the spectrum also sets the entrainment bandwidth and its spatial selectivity, with regional response amplified along eigenmodes of J whose imaginary part lies near ω_s. Pharmacology and stimulation are two readouts of the same linearized susceptibility, identifiable from the same fits [80].

Finally, the linear network sits naturally at the base of a modeling "ladder", where it has already provided evidence for the functional relevance of oscillations in the brain [81]. When nonlinear terms are reintroduced (full SL), one recovers amplitude dynamics, multistability, and turbulence-like regimes exploited to explain state-dependent changes (e.g., wake vs. sedation, psychedelic modulation) and nonequilibrium signatures. Yet even there, linear-response or linear-noise approximations remain invaluable for deriving analytic perturbation metrics (e.g. fluctuation–dissipation measures of nonequilibrium) and for mapping empirical changes onto interpretable parameter shifts [82–86].

3. Stuart–Landau oscillator (SL)

The Stuart–Landau (SL) oscillator extends the linear damped oscillator of Section 2 by adding a cubic amplitude saturation, producing a self-sustained limit cycle through a Hopf bifurcation. As the normal form of that bifurcation, SL is the minimal phase–amplitude model into which every nonlinear neural mass model considered in later sections (Wilson–Cowan, NMM1, NMM2) locally reduces near oscillation onset, so it serves as the universal local bridge for the cross-walk this review develops. Biologically, the cubic term abstracts a family of self-regulating mechanisms—synaptic depression, spike-frequency adaptation, inhibitory plasticity, and other homeostatic feedbacks—which together prevent the runaway dynamics of unregulated linear models.

In *polar form* writing $z = r\,e^{i\theta}$ yields

$$\dot{r} = \alpha\,r \;-\; \gamma\,r^3, \tag{3.1}$$

$$\dot{\theta} = \omega \;-\; \beta\,r^2. \tag{3.2}$$

Here, the linear terms $(\alpha,\ \omega)$ generate growth and rotation, while the amplitude-dependent nonlinearities $(\gamma,\ \beta)$ self-regulate both amplitude and frequency, stabilizing the limit cycle at $r = r^*$. More specifically, $\alpha \in \mathbb{R}$ is the linear growth ($\alpha > 0$) or decay ($\alpha < 0$) rate, $\omega > 0$ is the intrinsic oscillation frequency, $\gamma > 0$ governs nonlinear amplitude saturation, $\beta \in \mathbb{R}$ introduces nonlinear frequency modulation, coupling amplitude and phase. Equations ((3.1), (3.2)) represent the normal form of a Hopf bifurcation [87], which gives rise to the sustained oscillations characteristic of the SL (or sometimes called Hopf) model (see Fig. 3.1 and Appendix A for details).

The amplitude equation drives r toward

$$r^* = \sqrt{\frac{\alpha}{\gamma}}, \tag{3.3}$$

while the phase evolves at an amplitude-dependent rate $\dot{\theta} = \omega - \beta\,r^2$.

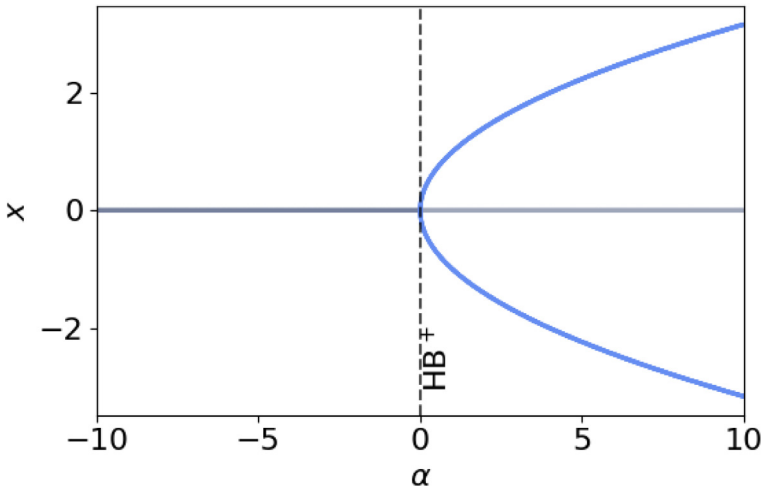

Fig. 3.1. Bifurcation diagram of the Stuart-Landau oscillator with bifurcation parameter α. Dark (light) gray lines indicate stable (unstable) fixed points. The amplitude of oscillations is indicated by the blue lines. The dashed line marks the supercritical Hopf bifurcation. See Table A.1 for details.

In *Cartesian form* with $x = r\cos\theta$ and $y = r\sin\theta$, one obtains

$$\dot{x} = \alpha x - \omega y - \gamma (x^2 + y^2)x + \beta (x^2 + y^2)y, \tag{3.4}$$

$$\dot{y} = \alpha y + \omega x - \gamma (x^2 + y^2)y - \beta (x^2 + y^2)x, \tag{3.5}$$

which makes explicit once again the dominating, push–pull motif in the first-order terms. In *complex form*, in turn, we have:

$$\dot{z} = (\alpha + i\omega)z - (\gamma + i\beta)|z|^2 z. \tag{3.6}$$

3.1. Effect of forcing

To model constant or time-varying synaptic inputs, we add a complex forcing term $F(t)$,

$$\dot{z} = (\alpha + i\omega)z - (\gamma + i\beta)|z|^2 z + F(t). \tag{3.7}$$

A constant F displaces the limit cycle to a new fixed point z^*, implicitly given by

$$(\alpha + i\omega)z^* - (\gamma + i\beta)|z^*|^2 z^* + F = 0,$$

generally yielding $|z^*| \neq \sqrt{\alpha/\gamma}$. Thus, $F(t)$ provides a biologically plausible mechanism for input-dependent modulation of both amplitude and frequency, although it may also alter the stability of the attractor (see Appendix D.5).

3.2. Coupling

Extending to a network of N diffusively coupled SL oscillators, each node i obeys

$$\dot{z}_i = (\alpha + i\omega_i)z_i - (\gamma + i\beta)|z_i|^2 z_i + \frac{G}{N}\sum_{j=1}^{N}(z_j - z_i) + \hat{F}_{e;i}(t), \tag{3.8}$$

where ω_i is the intrinsic frequency of node i, G the coupling strength, and $\hat{F}_{e;i}(t)$ any external input. The diffusive term synchronizes the network by pulling each oscillator toward the ensemble mean, while nonlinear saturation ensures bounded amplitudes, giving rise to collective phenomena such as synchronization, amplitude death, and clustering.

For whole-brain simulations with nonlinear nodes, we couple Stuart–Landau oscillators over a weighted connectome with optional delays, additive drive, and noise:

$$\begin{aligned}\dot{z}_i(t) &= (\alpha + i\omega_i)z_i(t) - (\gamma + i\beta)|z_i(t)|^2 z_i(t) \\ &\quad + G\sum_{j=1}^{N} C_{ij}\left[z_j(t - t_{ij}) - z_i(t)\right] + \hat{F}_{e;i}(t), \qquad i = 1, \ldots, N.\end{aligned} \tag{3.9}$$

where $z_i = x_i + i\,y_i$ is the complex state; $\alpha, \gamma, \beta \in \mathbb{R}$ and $\omega_i \in \mathbb{R}$ are the local SL parameters; $G \geq 0$ is a global coupling gain; $C = [C_{ij}] \in \mathbb{R}_{\geq 0}^{N\times N}$ is the (possibly directed) connectivity matrix (set $C_{ij} = 1/N$ for all-to-all if no connectome is used); $\tau_{ij} \geq 0$ are propagation delays (set $\tau_{ij} \equiv 0$ if ignored) and $\hat{F}_{e;i}(t)$ is the external forcing. We can rewrite these equations in polar coordinates to reconnect with the Kuramoto model [88]. For phase-oscillator networks with distance-dependent conduction delays — directly relevant to whole-brain SL models with heterogeneous tract lengths — Budzinski et al. [89] derive analytical predictions for the resulting spatiotemporal patterns by analyzing the spectrum of a delay operator combined with the adjacency matrix, providing closed-form access to the locked, twisted, and wave-like states observed in delayed Kuramoto-type whole-brain simulations.

Stuart-Landau Network (***Eq.*** (3.9))	
Whole-brain Simulations Parameters & Physiological Meaning	
Node i	Neural mass (parcel/column or nucleus) with nonlinear self–limiting dynamics.
N	Number of nodes (parcels).
$z_i(t) = x_i + i\,y_i$	Complex mesoscopic state; x, y are quadrature "push–pull" components (E/I-like in-phase and quadrature).
$r_i,\ \theta_i$	Amplitude and phase: $z_i = r_i e^{i\theta_i}$. Isolated steady amplitude (if $\alpha_i > 0$): $r_i^* = \sqrt{\alpha_i/\gamma_i}$; mean rotation $\Omega_i = \omega_i - \beta_i r_i^{*2}$.
α_i	Linear growth/decay (Hopf bifurcation parameter). $\alpha_i > 0$: self-sustained rhythm; $\alpha_i < 0$: decay to rest. Physiologically: net local gain/E–I balance, neuromodulatory tone.
ω_i	Intrinsic angular frequency (preferred local timescale) set by effective membrane/synaptic constants.
$\gamma_i > 0$	Nonlinear amplitude saturation (self-limiting gain); prevents runaway activity, sets r_i^*.
β_i	Amplitude–phase coupling ("shear"): amplitude changes shift instantaneous frequency; captures nonlinear dispersion/adaptation effects.
G	Global coupling gain scaling inter-areal drive over the connectome.
C_{ij}	Connectivity weight from region j to i (SC by default; FC/EC or synthetic graphs when needed).
τ_{ij}	Propagation delay $j \to i$ (conduction + synaptic latency); introduces frequency-dependent phase offsets.
$\hat{F}_{e;i}(t)$	Exogenous drive (external forcing from nodes or elements outside the network or an electric field, see Eq. (2.12)). Complex or real valued.
When to Use It	
Use this when you need *self-sustained rhythms with amplitude regulation* and phase–amplitude coupling; to place nodes near a Hopf bifurcation point and study metastability, envelopes, and input-dependent modulation. Coupled form Diffusively coupled SL nodes on a connectome; nonlinear saturation keeps amplitudes bounded and supports synchrony, clustering, chimeras, waves, and amplitude death (all-to-all in (3.8); connectome form in (3.9)). **How forcing enters** Add a complex input per node to shift the working point, entrain, or reshape amplitude and instantaneous frequency; constant biases displace the attractor, periodic drives yield nonlinear locking (single-node in (3.1)–(3.2); forcing in (3.7)). **Strengths** Minimal nonlinear phase–amplitude model; explicit control of oscillation onset via α; captures band-limited power, envelope FC/FCD, metastability/turbulence; reduces to linear analytics near the stable focus. **Limitations** Abstract (few biophysical knobs); parameter identifiability harder far from the Hopf bifurcation; sensitive to delays/coupling very close to the bifurcation; multi-timescale adaptation needs extensions. **Typical analyses** Fit FC/FCD and spectra; map working point vs. coupling/delays; quantify metastability/turbulence; assess entrainment and phase–amplitude metrics; graph-eigenmode/wave analyses. **Good defaults** Set $\gamma > 0$; place $\alpha \approx 0$ (slightly negative for subcritical "fluctuating" regime, slightly positive for limit cycles); modest ω heterogeneity; empirical W (optional delays τ_{ij}); small noise σ; tune β to match frequency–amplitude shifts. **Report** Working point (α), coupling/delay model, frequency distribution, input/noise statistics, and fitted readouts (PSD, FC/FCD, envelopes, metastability).	
How to Use It	
Model (drop-in): Provide C (SC default; FC/EC or synthetic graphs if SC unavailable), G, local (α_i, ω_i, $\gamma_i > 0$, β_i), optional τ_{ij}, $F_i(t)$, and $\hat{\eta}_i(t)$. Defaults normalize $C \leftarrow C/\lambda_{\max}(W)$; choose small α_i (tune distance to Hopf bifurcation: < 0 damped, > 0 limit cycle), set γ_i=1 for scaling, $\beta_i \approx 0$ initially; initialize $z_i(0)$ with small random amplitude; Euler–Maruyama or RK methods with $\Delta t \leq 1/(200 f_{\max})$. With non-zero delays $\tau_{ij} > 0$ and stochastic forcing, Eq. (3.9) is an SDDE; prefer method-of-steps DDE solvers in the deterministic limit, otherwise use Euler–Maruyama on the delayed system as a controlled approximation with the dual bound $\Delta t \leq \min\{1/(200 f_{\max}),\ \min_{ij} \tau_{ij}/10\}$ and convergence verified by step halving. **Readouts** amplitudes $r_i(t)$, phases $\theta_i(t)$, PSD/cross-spectra, spatial/temporal FC, order parameters for phase and amplitude; compare r_i to $r_i^* = \sqrt{\alpha_i/\gamma_i}$ when $\alpha_i > 0$.	

3.3. Applications

The Stuart–Landau equation arose as the weakly nonlinear amplitude equation for the laminar–turbulent transition in shear flows [90–92] and is now understood as the normal form of a Hopf bifurcation. Any sustained oscillation that emerges from an instability with weak nonlinearity admits a local SL description, which is what makes SL the natural meeting point for the rate, oscillator, and exact mean-field formalisms compared in this review.

In computational neuroscience, these same properties make SL a natural generative model for whole-brain dynamics. At the node level, the bifurcation parameter a controls the local working point — negative a gives noise-driven, damped fluctuations; $a \approx 0$ yields large, susceptible excursions; and positive a produces self-sustained rhythms — while ω sets the intrinsic timescale. Network coupling on the structural connectome, together with finite conduction delays and stochastic drive, then determines how local oscillators form transient coalitions, travel as waves, or lock into metastable patterns. In resting-state fMRI, SL networks tuned close to the edge of the Hopf bifurcation reproduce both static functional connectivity (FC) and its time variability (FCD), with the best fits occupying a narrow corridor of high *metastability* that effectively defines a dynamical cortical core [93]. Incorporating realistic delays in the same framework explains how fast local generators can coalesce into slow, spatially organized *metastable oscillatory modes* (MOMs) that appear and dissolve at reduced collective frequencies, linking anatomy to itinerant large-scale patterns observed across modalities [94].

Electrophysiologically, SL models provide a bridge between structure and spectra. Allowing one or multiple resonant channels per region improves the correspondence to resting MEG: SL networks account for band-limited envelope correlations, the location of spectral peaks, and the transient alignment of modes, with multi-frequency instantiations offering the best cross-band fits [95]. These same phase–amplitude dynamics, when embedded on the connectome with delays, rationalize why modest shifts in global coupling or delay reorganize band-limited power and envelope FC without changing anatomy, providing a mechanistic map from structure to oscillatory phenomenology [94,96]. Multimodal comparisons (fMRI+MEG) using common structural priors further demonstrate that SL's small, interpretable parameter set can jointly capture FC, FCD, and transient mode structure across measurements [7].

Casting SL network behavior in the language of *turbulence* sharpens the operational regime. When the model is fit to empirical amplitude turbulence and FC, the best-performing working point is typically *subcritical fluctuating*—just below the Hopf bifurcation—where susceptibility and information-encoding capacity are maximal; strength-dependent perturbations in this regime reveal richer responsiveness than in supercritical limit cycling [85,97]. A particularly clean neuroscience instantiation of these ideas is provided by Freyer et al. [98], who showed that an SL-type model with multiplicative noise operating near a subcritical Hopf bifurcation reproduces the scale-invariant bistability of the alpha rhythm observed in resting-state MEG. In their formulation, noise drives stochastic switching between a low-amplitude focus and a coexisting limit cycle, generating the heavy-tailed amplitude distributions and $1/f$-like spectral signatures characteristic of empirical alpha activity. This canonical example illustrates that noise near criticality is an organizing principle that supports physiologically realistic multistability in neural mass dynamics, and motivates the subcritical-fluctuating working point favored by SL whole-brain fits. Using closely related SL formulations, local-coherence ("turbulence") readouts distinguish wake, sleep, anesthesia, and pharmacologically altered states, positioning SL as a compact generative lens on state-dependent information flow [99]. The same perturbative logic extends to psychedelics: after fitting LSD and placebo states, SL-based *in silico* stimulations predict enhanced sensitivity to strong inputs and characteristic turbulence signatures under LSD, consistent with empirical observations of expanded dynamical repertoires [100,101]. A complementary perspective frames such state changes through the geometry and complexity of the underlying state space, with plasticity-induced reshaping of attractors as the mechanistic substrate of psychedelic-driven dynamics [102].

Biologically, SL's parameters expose the very levers experiments can turn. Interpreting the bifurcation parameter as net local E/I gain and neuromodulatory tone frames drugs as *parameter shifts* that move regions toward or away from oscillatory onset; interpreting external input as *forcing* turns stimulation into a probe of the network's susceptibility, mode by mode. Personalizing SL fits thus yields subject-specific maps of working points and delays that generate testable predictions about which regions and frequencies will respond most — and how those responses reorganize whole-brain dynamics. Building on this, dynamic sensitivity analysis quantifies how localized stimulation perturbs subject-specific SL/WC fits and identifies the regions whose targeted modulation most efficiently drives transitions between brain states [103]. Finally, because SL admits a linear approximation near the stable focus, one can derive closed-form spectra and covariances for rapid exploration and uncertainty quantification, then reintroduce nonlinearity as needed; this provides a transparent bridge between analytic tractability and the rich nonlinear phenomena that motivate the model in the first place [30].

4. Interlude: Synapses and transfer functionals

The discussion below interchanges neurotransmitter release, ionic currents, and membrane potential perturbations. These quantities are related by linear operators, and composition of linear operators is itself a linear operator (see Appendix E); The chain from presynaptic action potential through conductance, synaptic current, and membrane voltage is the receiving cell therefore collapses to a single first- ore second-order differential equation.

Table 4.1
Generic ranges for the values of τ_r and τ_d, extracted from [112] and references therein.

Neurotransmitter	τ_r [ms]	τ_d [ms]
AMPA	0–2	2-5
NMDA	3–15	40-100
$GABA_A$	0–2	6-20
$GABA_B$	25–50	100-300

4.1. Synaptic dynamics and operator formalism

Neurons have two main forms of communication: chemical and electrical. The first happens through neurotransmitters emitted by the presynaptic neuron after a spike [104]. The second is bound to the existence of gap-junctions between nearby cells [105]. It is estimated that chemical synapses drive the vast majority of neural communication in the mammalian brain, and for this reason, electrical coupling has often been considered as a secondary character in neural dynamics (see, however, [106–108]). Thus, earlier work on NMMs focused on chemical coupling only.

For a single synaptic connection, the dynamics of neurotransmitter binding can be modeled as kinetic reactions [109–111]. Ultimately, both experimental and modeling results show that, typically, upon receiving a spike, the effect of neurotransmitter release to a postsynaptic neuron will first undergo an exponential increase of post-synaptic potential, followed by an exponential decay. Therefore, the postsynaptic-potential $s_j(t)$ (mV) of a single, isolated neuron is usually modeled by the *second order ordinary differential equation* [111,112]

$$\tau_r \tau_d \ddot{s}_j = \gamma r(t) - (\tau_r + \tau_d)\dot{s}_j - s_j \tag{4.1}$$

where τ_r and τ_d are the rise and decay times (ms), γ is the amplitude of the PSP (mV/kHz), and $r(t)$ is the input term, modeling the arrival of presynaptic spikes.

While Eq. (4.1) corresponds to that of a single neuron j, its linearity allows us to quantify the mean synaptic activity of N neurons receiving and reacting identically to the same inputs as $s(t) = \frac{1}{N}\sum_{j=1}^{N} s_j(t)$. Then, we obtain the same equation for the mean synaptic activity,

$$\tau_r \tau_d \ddot{s}(t) = \gamma\, r(t) - (\tau_r + \tau_d)\dot{s} - s\ . \tag{4.2}$$

Interestingly, Eq. (4.2) shares the same structure as the equation of a damped, driven harmonic oscillator, which, as we will show in the following sections, allows it to display oscillations and exhibit diverse dynamical responses.

For a single pulse received at time zero ($r(t) = \delta(t)$), the solution to (4.2) is

$$s(t) = \frac{\gamma}{\tau_d - \tau_r}\left(e^{-t/\tau_d} - e^{-t/\tau_r}\right)\ . \tag{4.3}$$

Usually, different types of neurotransmitters will result in different timescales. Table 4.1 contains some putative quantities for these parameters. Considering this variety of time scales, there are two limiting cases of Eq. (4.2) that are widely used in the literature. In some cases, one can simplify this equation by assuming that the rise and decay times are identical, $\tau = \tau_r = \tau_d$. Then Eq. (4.2) reads

$$\tau^2 \ddot{s}(t) = \gamma\, r(t) - 2\tau\, \dot{s} - s\ . \tag{4.4}$$

The solution of this equation for a single pulse at time zero ($r(t) = \delta(t)$) reads

$$s(t) = \frac{\gamma\, t}{\tau^2}\, e^{-t/\tau} \tag{4.5}$$

which is sometimes referred to as *alpha synapse*.

Time constants for the principal receptor types — α-amino-3-hydroxy-5-methyl-4-isoxazolepropionic acid (AMPA), N-methyl-D-aspartate (NMDA), and γ-aminobutyric acid ($GABA_A$, $GABA_B$) — are summarized in Table 4.1.

On the other hand, if one considers that the rise time is almost instantaneous, $\tau_r \to 0$, then Eq. (4.2) reads

$$\tau_d \dot{s} = \gamma r(t) - s(t) \tag{4.6}$$

which is just an equation for exponential decay, thus a single pulse at $r(t) = \delta(t)$ gives the solution

$$s(t) = \frac{\gamma}{\tau_d} e^{-t/\tau_d}. \tag{4.7}$$

Other types of neurotransmitter kinetics might result in more complex synaptic dynamics [109,110]. Of particular importance is the glutamate NMDA receptors, whose dynamics also depend on the voltage of the postsynaptic neuron [111,112].

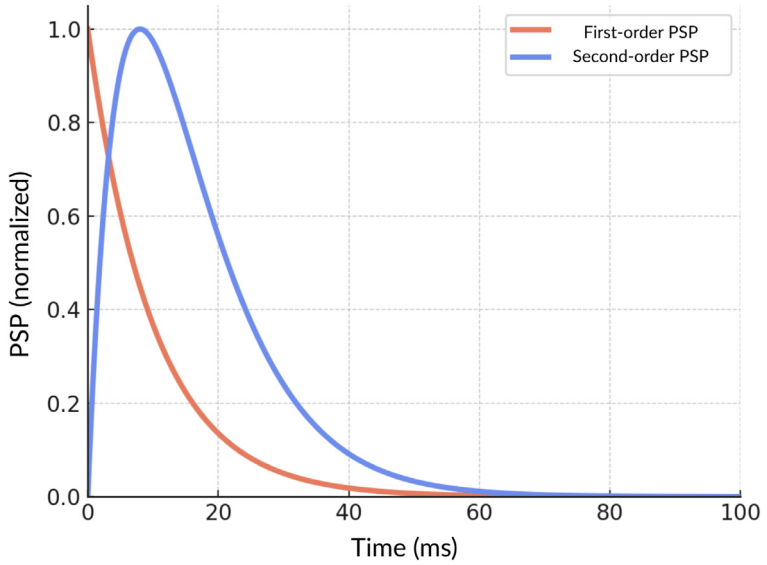

Fig. 4.1. Post synaptic potentials in the first-order or the more realistic second-order synapse models. These plots are the response to an "impulse" at time zero, i.e., the solutions to $\hat{L}[x] = \delta(t)$.

The synapse as filter: Operator form

How should the synapse equations be read? To shed some light on this, we recast Eq. (4.2) into operator form by rewriting it first,

$$\tau_r \tau_d \ddot{s}(t) + (\tau_r + \tau_d)\dot{s} + s = \gamma r(t),$$

and defining the synapse linear operator

$$\hat{L}_s[s(t)] = \frac{1}{\gamma}\Big[\tau_r \tau_d \frac{d^2}{dt} + (\tau_r + \tau_d)\frac{d}{dt} + 1\Big]s(t). \tag{4.8}$$

Then Eq. (4.2) can be written succinctly as

$$\hat{L}_s[s(t)] = r(t). \tag{4.9}$$

The synapse operator $\hat{L}$ can be derived using the properties of linear time-invariant systems, and the impulse response of the neural mass has the form of Eq. (4.7), which is a model supported by experimental and theoretical studies [113–116] (see Appendix E for details).

The synapse operation can be cast as a causal filter. Since $\hat{L}$ is a linear differential operator, using proper boundary conditions, we can define its inverse $\hat{L}^{-1} = \hat{K}$ (another linear operator),

$$s(t) = \hat{K}_s[r(t)]. \tag{4.10}$$

This shows that the synapse response (membrane voltage perturbation) is a filtered version of its firing rate input.

The same logic applies to Eq. (4.6), but this time the operator is first order,

$$\hat{L}_s[s(t)] = \frac{1}{\gamma}[\tau_d\, d/dt + 1]s(t). \tag{4.11}$$

Synapses are *linear operators*: filters that transduce incoming firing rate inputs into currents or PSPs. The effect of such a filter is to distort and delay the incoming signals. Their action can be characterized by the impulse response, i.e., how it responds to a sharp (delta function) input, $\hat{L}[x] = \delta(t - t_0)$. In the case of Wilson–Cowan, where the operator is first order, the response is simply a decaying exponential (see Fig. 4.1).

In more realistic models, such as Jansen–Rit (JR) [117], Wendling [118], or LaNMM [119,120], the linear operator is *second order*. The second-order operator is essential for realistically capturing synaptic conductance dynamics, as biological PSPs do not rise instantaneously. While a simple first-order exponential decay adequately describes passive membrane voltage relaxation, it neglects the finite time required for neurotransmitter binding, ion channel opening, and resulting conductance increase. Introducing separate rise (τ_{rise}) and decay (τ_{decay}) time constants (which may be the same numerically), the second-order operator accurately represents this two-phase process: a rapid initial conductance increase followed by slower conductance closure. This explicitly accounts for physiological delays and ensures PSP dynamics

Table 4.2
Analytical expressions for the transfer functions of some heuristic models and static approximations of integrate-and-fire models, including leaky integrate-and-fire (LIF), exponential integrate-and-fire (EIF) and quadratic-integrate-and-fire (QIF). In the case of EIF, $F(v) = -\frac{v^2}{2} + Iv + \Delta_T^2 \exp\left(\frac{v-V_T}{\Delta_T}\right)$.

Model	$\varphi[I]$	Refs.
Sigmoid	$\frac{2e_0}{1+e^{\rho(I_0-I)}}$	[117,122]
LIF (Gaussian noise)	$\left\{\tau_m\sqrt{\pi}\int_{\frac{V_r-I}{\sigma}}^{\frac{V_{th}-I}{\sigma}} \exp\left(x^2\right)[1+\mathrm{erf}(x)]\mathrm{d}x\right\}^{-1}$	[123–125]
EIF (Gaussian noise)	$\left\{\frac{2\tau_m}{\sigma^2}\int_{-\infty}^{V_{th}}\int_{\max(V,V_r)}^{V_{th}} e^{\frac{2}{\sigma^2}(F(v)-F(u))}\mathrm{d}u\mathrm{d}v\right\}^{-1}$	[126,127]
QIF (Gaussian noise)	$\left\{\tau_m\sqrt{\pi}\int_{-\infty}^{\infty}\exp\left(-\frac{\sigma^4}{48}x^6 - Ix^2\right)\mathrm{d}x\right\}^{-1}$	[128]
QIF (Cauchy noise)	$\frac{1}{\tau_m\pi\sqrt{2}}\sqrt{I+\sqrt{I^2+\Delta^2}}$	[129,130]

include a biologically realistic temporal scale, crucial for correctly modeling neuronal integration and timing-dependent neural computations.

Synaptic dynamics depend on the firing rate of the presynaptic population, which we now turn to.

4.2. Current-based versus conductance-based synapses

Throughout this review we adopt a *current-based* description of synaptic interaction, in which the synaptic input is treated as an additive perturbation to a postsynaptic state variable through the linear filter $\hat{L}_s$. This is a deliberate idealization. Real chemical synapses are *conductance-based*: the synaptic current depends explicitly on the postsynaptic membrane potential through the reversal potential E_{rev} of the relevant ion channel,

$$I_{\mathrm{syn}}(t) \;=\; g(t)\big(E_{\mathrm{rev}} - V(t)\big), \tag{4.12}$$

where $g(t) \geq 0$ is the time-dependent synaptic conductance, generated by the same kinetic mechanisms that produce the second-order PSP shape derived above [109,110]. The dependence on $V(t)$ is the source of *shunting*: as the membrane potential approaches E_{rev}, the driving force $(E_{\mathrm{rev}} - V)$ vanishes and the synapse delivers no current despite the elevated conductance, and if V overshoots E_{rev} the effective sign of the interaction reverses. An "inhibitory push" can therefore become a "pull" or vanish entirely depending on the operating point, a property absent from the current-based filter. For the cross-walk developed in this review, the current-based form is retained because the rate-based and exact-mean-field neural mass models compared in Sections 5–7 are themselves formulated in current-based terms, and because near a stable operating point the conductance-based interaction linearizes to a current-based effective coupling with state-independent effective gain. The conductance-based / shunting Liley-type mass listed in block (B) of the roadmap Table retains the full V-dependence and is the natural starting point for readers requiring explicit shunting effects, including the voltage-dependence of NMDA-receptor dynamics noted at the end of Section 4.1.

4.3. Transfer functional

Experimental results characterize the firing rate of a population of neurons as a function of its total input current or membrane potential. This approach extends the concept of f-I curve, used to characterize the dynamics of single neurons [14,121], to a neural population. Accordingly, a population receiving an input current $I(t)$ produces a firing rate given by

$$r(t) = \hat{\Phi}[I(t)], \tag{4.13}$$

where $\hat{\Phi}$ is some operator (the *transfer functional*) that describes the process, including delays in response and non-linearity. For simplicity, this is sometimes simplified to a static and instantaneous nonlinear relation between the input and the output of a neural mass. The functional becomes then a function φ with

$$r = \varphi(I), \tag{4.14}$$

which receives the name of *transfer function*.

There are several possible choices for the shape of the transfer function φ (see Table 4.2). A common choice is the sigmoid function considered by Wilson and Cowan [122],

$$\varphi(I) = \frac{2e_0}{1+e^{\rho(I_0-I)}} \equiv \sigma[I] \tag{4.15}$$

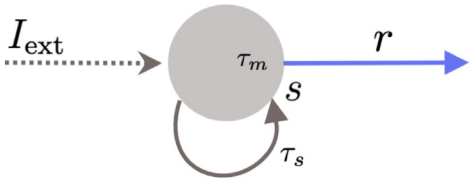

Fig. 4.2. Simple recurrent population model. Here, the population receives an external current I_{ext} and self-input via a synapse s, and outputs its firing rate r. Two time scales (delays) enter: the membrane response time constant τ_m for updating the firing rate r, and the synaptic current time constant τ_s. See Eq. (4.19) in the text for details.

where e_0 is half of the maximum firing rate of each neuronal population, I_0 is the value of the current when the firing rate is e_0, and ρ determines the slope of the sigmoid at the central symmetry point (I_0, e_0). Wilson and Cowan argued that such a sigmoidal shape accounts for heterogeneity in either neural connectivity or excitability threshold. Freeman proposed another expression that he fitted to experimental data, obtaining a similar sigmoid shape [131,132].

Further theoretical and experimental research has validated that, indeed, neurons subject to an increasing input current $I(t)$ produce a firing rate that, in many cases, can be captured by a nonlinear function. However, these functions do not always follow a sigmoid function. For instance, Amit and Brunel derived the transfer function that follows from considering a network of leaky integrate-and-fire neurons subject to Gaussian noise [124] Similarly, transfer functions for exponential integrate-and-fire, quadratic integrate-and-fire and others have been derived analytically [126–129]. We provide the transfer functions of some of these cases in Table 4.2.

Dynamical transfer functions, where the response of the population is not instantaneous, were addressed by Wilson and Cowan, who proposed a filtered, exponential decay dynamics towards the firing rate activity,

$$\tau_m \dot{r} = -r + \varphi(I(t)), \tag{4.16}$$

where τ_m is a time scale controlling the response time of the neuron. As mentioned at the beginning of this section, this exponential decay response has often been used interchangeably with the exponential decay dynamics presented in Eq. (4.6), although notice that the time constants τ_m and τ_d account for different biophysical quantities.

Using operator language with $\hat{L}_m = \tau_m d/dt + 1$ and inverse $\hat{K}_m = \hat{L}_m^{-1}$ (a linear filter or convolution), this can be expressed as a non-linear filter

$$r = \hat{\Phi}_m[I(t)] \tag{4.17}$$

with the *transfer functional* is $\hat{\Phi}_m[\cdot] = \hat{K}_m\big[\varphi[\cdot]\big]$. In this case, we talk of a transfer *functional* and not function: a nonlinear operator mapping total input currents to firing rate time series with delay governed by the time scale τ_m.

4.4. A simple self-coupled model and different limits

Let us consider now a population of neurons of the same type that receive an external input $I_{\text{ext}}(t)$ and has recurrent connectivity given with a strength κ (see Fig. 4.2). Then, we can assume that the total input received by the population is

$$I(t) = \kappa s(t) + I_{\text{ext}} \tag{4.18}$$

where κ is an electrical admittance relating membrane potential perturbation and current. Notice that to derive the expression of the total input (4.18) we have assumed that the current flux generated by the recurrent coupling is proportional to the post-synaptic potential. This is an additional hypothesis that we will revisit later on.

Therefore, the dynamics of the average PSP of this population is given by

$$\begin{aligned} &\tau_m \dot{r} = -r + \varphi[\kappa s + I_{\text{ext}}]\ , \\ &\hat{L}_s[s] = r. \end{aligned} \tag{4.19}$$

which we can rewrite in full operator form as the*master neural mass model equation*

$$\boxed{\begin{aligned} r &= \hat{\Phi}_m[\kappa s + I_{\text{ext}}], \\ s &= \hat{K}_s[r]. \end{aligned}} \tag{4.20}$$

with $\hat{\Phi}_m$ the transfer functional and $\hat{K}_s$ the usual synaptic filter inverse operator characterized by some time scales τ_s — see Eqs. (4.17) and (4.10).

Eq. (4.20) provides the minimal building blocks to derive a range of NMMs from simple principles. As we discuss next, taking $\tau_m \to 0$ or $\tau_s \to 0$ with first or second order synaptic operators, it covers the Wilson–Cowan (see Section 5), NMM1 (Section 6) and NMM2 (Section 7) formalisms. Finally, it also encompasses other logical variants — for example, a Wilson–Cowan style transfer function paired with second-order synapses. Although extensions of the Wilson–Cowan model do

incorporate synaptic filtering or plasticity dynamics [133], to the best of our knowledge there exists no commonly adopted neural-mass model that preserves the original Wilson–Cowan architecture while explicitly modeling separate finite time constants for the membrane and the synaptic stages and, in particular, uses second-order synaptic operators — as proposed in our 'master NMM' formalism.

Limit of fast synapses (Wilson-Cowan model). Taking the synaptic time constant to be much smaller than the membrane constant, $\tau_s \ll \tau_m$, leads to the *limit of fast synapses,*

$$\begin{aligned} r &= \hat{\Phi}_m[\kappa s + I_{\text{ext}}] \,, \\ s &= \gamma r, \end{aligned} \tag{4.21}$$

with γ the scaling constant associated with the $\hat{L}$ operator. This is the stance taken by Wilson–Cowan (see Section 5), which we can rewrite in firing rate form as

$$r = \hat{\Phi}_m[\omega r + I_{\text{ext}}], \tag{4.22}$$

with $\omega = \gamma\kappa$, or, equivalently in synapse potential (PSP) form as

$$s = \gamma \hat{\Phi}_m[\kappa s + I_{\text{ext}}]. \tag{4.23}$$

In this limit, we can think of firing rate and synaptic PSPs as the same up to scale (there is no delay, only a rescaling). Thus, the Wilson–Cowan equations can be read as firing rate or synaptic equations, although the dynamics are due to membrane capacitance rather than synaptic currents.

Limit of fast membrane. Conversely, if $\tau_m \ll \tau_s$ — the *limit of fast membrane* —, the firing rate ODE becomes a static equation,

$$\begin{aligned} r &= \varphi[\kappa s + I_{\text{ext}}] \,, \\ \hat{L}_s[s] &= r. \end{aligned} \tag{4.24}$$

This is the approach taken in the Jansen–Rit formalism (NMM1) when the synaptic equations are second-order, for example.

Delays and refractory period. Finally, Eq. (4.19) contains two time constants (τ_m and τ_s). However, there are two more time constants that play an important role in neural dynamics, and which we briefly mention here: *time delays* and *refractory periods*. Time delays introduce additional time scales that account for the latency of neurons or connecting circuit elements for reaching the threshold voltage and releasing the neurotransmitters. This effect might be due to different elements, for instance, the propagation of signals along the axon. This might be simply modeled by adding a delay in the synaptic dynamics

$$\hat{L}[s] = r(t - \tau_l). \tag{4.25}$$

Notice that delay-differential equations have some special properties. For instance, their dynamics are infinite-dimensional, and thus, phenomena such as oscillatory activity can arise in instances where this was not previously considered.

On the other hand, refractory periods correspond to the inability of neurons to respond to external stimuli for a few milliseconds after an action potential. Whether refractory periods have a major role in the collective dynamics and function of neural populations is still a matter of debate. In the simple framework explained so far, there are two main ways to include a refractory period. On one hand, some researchers assume that transfer functions with a sigmoid function, i.e., a saturation for higher input, are already accounting for these refractory periods, hence the saturation. However, many researchers consider transfer functions derived from models, which do not saturate for large inputs. On the other hand, following Wilson and Cowan [134], the fraction of neurons susceptible to external inputs at any time t is given by

$$1 - \int_{t-\tau_f}^{t} r(t)\mathrm{d}t \tag{4.26}$$

where τ_f (ms) is the refractory period. Therefore, Eq. (4.16) should instead read

$$\tau_m \dot{r} = -r + \left(1 - \int_{t-\tau_f}^{t} r(t)\mathrm{d}t\right) \Phi[I(t)] \,. \tag{4.27}$$

By considering that $\tau_f \ll \tau_m$, the integral can be approximated as $\int_{t-\tau_f}^{t} r(t)\mathrm{d}t \approx \tau_f r(t)$ and the previous equation then reads

$$\tau_m \dot{r} = -r + \left(1 - \tau_f r\right) \Phi[I(t)] \,. \tag{4.28}$$

For the sake of completeness, we now reproduce Eq. (4.19) with both time delays and refractory period:

$$\begin{aligned} \tau_m \dot{r} &= -r + (1 - \tau_f r)\Phi[\kappa s(t) + I_{\text{ext}}] \,, \\ \hat{L}[s] &= r(t - \tau_l) \end{aligned} \tag{4.29}$$

5. The Wilson–Cowan model (WILCO)

As a phenomenological normal form, the Stuart–Landau (SL) oscillator captures the universal signature of a Hopf bifurcation. Yet real neural tissue is not a single abstract amplitude, but excitation and inhibition speaking in tandem. Wilson–Cowan (WILCO) portrays that biological dialogue transparently: two real variables x, y, representing firing rates or PSPs, interacting via synaptic weights, membrane time-constants, sigmoid gains, and neural drives. But compared with the simpler oscillator models, WILCO is not only biologically transparent but dynamically richer. Near a Hopf bifurcation that it sits on the edge between a quiescent (damped) fixed point and a self-sustaining oscillation, WILCO reduces on its center manifold to the SL normal form (see Appendix C). This equivalence is local: away from the bifurcation, and depending on parameter choices, WILCO supports saturation regimes, multistability between fixed points, and pattern-formation regimes that are not captured by the SL normal form. Finally, while the Wilson–Cowan model was originally conceived with x and y representing firing rates, its dynamics can also be used to represent first-order synaptic activity, with x, y representing PSPs.

Following Eq. (4.21) (fast synapse limit, where firing rate input and PSP are related linearly without delay), or more concretely the form in Eq. (4.23), for a single population, we consider the model for a pair of coupled populations introduced by Wilson and Cowan [134],

$$\begin{aligned} \tau_x \dot{x} + x &= \gamma_x \, \sigma_x\big(\kappa_{xx} x - \kappa_{xy} y + P_x\big), \\ \tau_y \dot{y} + y &= \gamma_y \, \sigma_y\big(\kappa_{yx} x - \kappa_{yy} y\big), \end{aligned} \tag{5.1}$$

with x and y representing synapse PSPs and τ_α are membrane time-constants, $\kappa_{\alpha\beta}$ the effective synaptic weights (positive for excitation, negative for inhibition), P_x a tonic slowly varying drive that acts as the bifurcation (control) parameter, and γ_α the synapse gain term [48]. The sigmoid functions (see Eq. (4.15)) are specific for each population.

In the form corresponding to Eq. (4.22), where x, y represent firing rates, we have

$$\begin{aligned} \tau_x \dot{x} + x &= \sigma_x\big(w_{xx} x - w_{xy} y + P_x\big), \\ \tau_y \dot{y} + y &= \sigma_y\big(w_{yx} x - w_{yy} y\big). \end{aligned} \tag{5.2}$$

Regardless of its synaptic or firing rate form, the original WILCO model describes dynamics stemming from transfer function delays. Despite its origins, the model is sometimes interpreted as describing first-order synapse dynamics. The form remains the same, but the interpretation changes (dynamics are induced by synaptic, not membrane delays).

A Taylor expansion shows that Eq. (5.2) contains the Hopf bifurcation machinery in the SL normal form plus additional bifurcations. Moreover, each coefficient is anchored to a biophysical mechanism (e.g. self-excitation w_{xx} or synaptic delay τ_x).

WILCO contains the Stuart–Landau oscillator as one of its parameter-tuned limits. When the cross-coupling is weak, the model supports a clean Hopf bubble ($\text{HB}^- \to \text{LC} \to \text{HB}^+$) with no fold or SNIC anywhere on the slice, and the center-manifold reduction at either end is the Stuart–Landau normal form. In this limit WILCO is SL. Once the cross-coupling product $\kappa_{xy}\kappa_{yx}$ crosses a threshold set by the diagonal terms, a Bogdanov–Takens point enters the oscillatory window. The saddle–node, SNIC, and Hopf curves emerge from it as three branches of a single codimension-2 unfolding: the cusp brings bistability, the SNIC brings Class I excitability, and the system displays dynamics genuinely beyond SL's reach. In this regime WILCO is more than SL. The two regimes are 1-parameter slices through the same equations, separated by exactly one codimension-2 point in parameter space. This is what gives WILCO its place in the Rosetta Stone: it specializes to SL — and to the PING/Jansen–Rit gamma rhythm — at one limit, extends to bistability and Class I excitability at the other, and the hinge between them is a single locatable point.

5.1. Effect of forcing

Shifting the tonic drive P_x moves the mean input along the sigmoid with respect to the sigmoid threshold, i.e., the population *operating point*; because the slope $\sigma_x'(\cdot)$ changes with input, the effective linear gain and thus the distance to Hopf vary smoothly [135].

Introducing an additional term $\hat{F}_e(t)$ to the excitatory equation in firing rate form reads

$$\tau_x \dot{x} + x = \sigma_x\big(w_{xx} x - w_{xy} y + P_x + \hat{F}_e(t)\big). \tag{5.3}$$

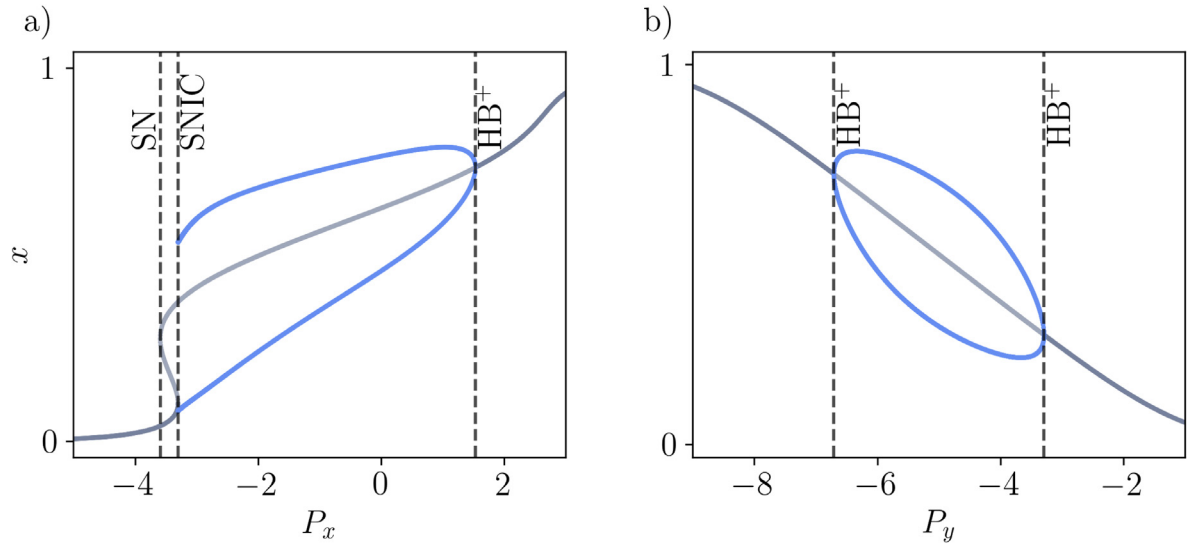

Fig. 5.1. The two oscillator personalities of WILCO. Both panels display the x-component of fixed points and limit cycles as a function of external inputs. Solid gray lines indicate stable/unstable fixed points, while blue curves denote limit-cycle minima and maxima. (a) Transitioning through P_x from left to right, the system exhibits a progression from a saddle–node (SN) to a saddle–node-on-invariant-circle (SNIC) bifurcation, eventually terminating at a supercritical Hopf bifurcation (HB^+). This configuration allows the model to switch between Class I excitability (near the SNIC) and Class II excitability (near the HB^+). (b) The pure Hopf bubble: In this regime, the oscillatory activity is isolated within a "bubble" bounded by two supercritical Hopf bifurcations (HB^+), with no fold or SNIC bifurcations present. Here, the system functions as a pure Class II oscillator, locally equivalent to a Stuart–Landau oscillator.

Near its bifurcation, the model becomes a forced SL oscillator [136]. $\hat{F}_e(t)$ may represent noise or a time-varying (e.g. sinusoidal, noisy, pulsed), or constant but transiently switched on and off forcing; in either case, it probes or entrains the dynamics without altering the underlying bifurcation point set by P_x. Sinusoidal forcing carves out Arnol'd tongues of n:m phase locking whose geometry parallels that of the analytical SL normal form, yet the effective tongue width is filtered by the sigmoid slope σ'_x, a feature absent from purely polynomial descriptions.

5.2. Minimal ingredients for a Hopf bifurcation

Linearizing (5.2) around its fixed point (x_0, y_0) and applying the Routh–Hurwitz criteria, a Hopf bifurcation occurs when $\mathrm{tr}J = 0$ with $\det J > 0$ [137]. Physiologically, this translates into three rules:

1. *Reciprocal E–I coupling* ($w_{xy}w_{yx} < 0$) is indispensable; a single self-exciting pool cannot realize a Hopf bifurcation.
2. *Sigmoid slope.* Either recurrent excitation $w_{xx} > 0$ or an external drive P_x must position the operating point on the steep part of σ_x so that $\sigma'_x(\cdot) \neq 0$, recovering Ermentrout's criterion for "sufficient self-coupling or bias" [138].
3. *Cubic saturation.* The curvature of S_α supplies the cubic term that tames the growth of infinitesimal oscillations; piece-wise linear gains suppress this mechanism.

Projecting the WILCO equations onto their two-dimensional center manifold yields — after normal-form transformation — the complex Stuart–Landau equation [139]

$$\dot{z} \;=\; (\alpha + i\,\omega)z \;-\; (\gamma + i\,\beta)\,|z|^2 z, \tag{5.4}$$

where the real coefficients α, γ and their imaginary counterparts ω, β are explicit functions of τ_α, $w_{\alpha\beta}$ and the first two derivatives of S_α; their signs decide whether the Hopf is super- or sub-critical. Conversely, the physiological variables follow $(x, y)^\top \approx \mathrm{Re}[z\, v]$, with v the critical eigenvector. See Appendix C for more details.

The logistic transfer curve packages dendritic saturation, membrane noise, and threshold heterogeneity into one analytic function [2]. Its first derivative shapes the linear gain, its second derivative injects the cubic non-linearity that stabilizes the limit cycle—precisely the $-(\gamma + i\beta)|z|^2 z$ term in (5.4). In other words, the WILCO sigmoid is a *built-in normal-form generator*.

Two examples of WILCO bifurcation diagrams are provided in Fig. 5.1; they are 1-parameter slices through the same model equations, differing only in which external input parameter is varied (P_x or P_y) while the others remain fixed.

The model in panel (a) — P_x-driven regime (see Table A.1 for parameters) — exhibits three different bifurcations as the external input to the excitatory population, P_x, is increased. Initially, for low P_x, the system has a single stable fixed point. As P_x increases, the system undergoes a saddle–node (SN) bifurcation, where two unstable fixed points emerge. Further increasing P_x leads to the collision and annihilation of a stable and an unstable fixed point, and, beyond this point, a limit cycle emerges. This transition corresponds to a saddle–node on an invariant circle (SNIC) bifurcation. Finally, the limit cycle vanishes in an HB^+ bifurcation, and from that point the system only has a stable fixed point. Thus, near HB^+, WILCO reduces on its center manifold to a Stuart–Landau oscillator (Class II onset, finite frequency, vanishing amplitude); near SNIC it reduces to a theta-neuron/QIF normal form (Class I onset, finite amplitude, vanishing frequency); and near SN, to a saddle–node normal form (bistability, no oscillation). All three reductions are local pieces of the same Bogdanov–Takens (BT) unfolding, of which panel (a) is a 1-parameter slice.

The model in panel (b) — the P_y driven regime-coupling (see Table A.1 for parameters) — exhibits a different bifurcation structure: a clean Hopf bubble bounded by HB^- at one end and HB^+ at the other, with no fold and no SNIC anywhere on the slice. The cycle is born of small amplitude at HB^-, grows smoothly across the bubble, and dies of small amplitude at HB^+. The center-manifold reduction at *both* ends of the bubble is the Stuart–Landau normal form, and the cycle is locally Stuart–Landau across the whole window (Class II only, no Class I, no bistability).

By navigating this parameter space, WILCO effectively contains the Stuart–Landau oscillator as a parameter-tuned limit while adding the BT-organized cusp and SNIC structures as a functional extension. This allows the same model equations to switch between acting as a simple harmonic-like oscillator and a complex neural integrator.

5.3. Coupling

To build a whole-brain network of equal Wilson–Cowan E-I motifs, the excitatory populations are usually coupled via long-range glutamatergic projections [7]. Introducing both tonic/exogenous inputs ($P_{x,i}$) and dynamic drives ($\hat{F}_e(t)$) at the excitatory nodes, the coupled system reads (firing rate version)

$$\begin{aligned} \tau_x \dot{x}_i + x_i &= \sigma_x\Big(w_{xx}\, x_i - w_{xy}\, y_i + P_{x,i} + \hat{F}_{e;i}(t) + \sum_{j\neq i}^{N} C_{ij}\, x_j\Big), \\ \tau_y \dot{y}_i + y_i &= \sigma_y\big(w_{yx}\, x_i - w_{yy}\, y_i\big). \end{aligned} \tag{5.5}$$

Here C_{ij} denotes the (row-normalized) structural connectivity weight from node j to node i, typically estimated from diffusion-MRI tractography.

Long-range excitation $\sum_j C_{ij}x_j$ is integrated inside the sigmoid: distant axonal currents enter the same dendritic current pool through instantaneous synapses; the non-linearity then converts the total current into a bounded firing rate, preserving the physiological ceiling set by σ_x.

The network form in Eq. (5.5) has been the subject of extensive analysis in the dynamical-systems and computational-neuroscience literature, going well beyond the original two-population formulation of Wilson and Cowan. Foundational mathematical analyses of coupled WILCO units characterized the phase-plane structure, oscillation onset, and bifurcation skeleton of the canonical pair [140,141], and subsequent work has mapped the multistability, metastability, and pattern-forming regimes that arise when many WILCO nodes are coupled through delayed connectivity [142,143]. The treatment in the present section is therefore best understood as a unified-notation summary of an established line of work, repositioned to serve the cross-walk to the Stuart–Landau, NMM1, and NMM2 formalisms developed in subsequent sections.

Of particular relevance to the cross-walk this review develops, WILCO networks admit phase and phase–amplitude reductions back to generalized Kuramoto-type oscillator networks of the form discussed in Section 2. Hlinka & Coombes [144] demonstrated that phase reductions of WILCO networks reproduce empirically observed structural–functional connectivity relationships in resting-state fMRI, providing an explicit bridge between the rate-based formulation and the phase-oscillator analyses of Section 2. Daffertshofer & van Wijk [142] further analyzed how the amplitude dynamics of WILCO modulate phase connectivity, clarifying the regime in which the phase-only description remains predictive. These reductions are the operational bridge that makes the WILCO $\rightarrow$ Kuramoto leg of the cross-walk explicit.

Eq. (5.5) implement *additive* coupling: each excitatory node i receives the transduced firing rates x_j of its peers weighted by C_{ij}. This choice reflects the physiology of long-range excitatory fibers and avoids the homeostatic constraints of diffusive schemes, allowing the network to exhibit rich collective dynamics — from large-scale synchrony and traveling waves to stimulus-induced entrainment — while preserving the local Wilson–Cowan bifurcation structure.

Eq. (5.5) is one among many possible combinations of populations, couplings, and forcings.

Wilson-Cowan Network (***Eq.*** (5.5)) **Whole-brain Simulations Parameters & Physiological Meaning**	
Node i	Coarse-grained cortical/subcortical region represented by two interacting subpopulations: excitatory (x_i) and inhibitory (y_i).
N	Number of regions (E–I motifs) in the network.
$x_i(t),\ y_i(t)$	Population activities (firing rates or PSP proxies, depending on the form used); the E/I push–pull loop produces oscillations and multistability (*cf.* (5.1), (5.2)).
$\tau_x,\ \tau_y$	Membrane/synaptic time constants (ms) setting local response speeds and the E–I timescale separation.
$\sigma_x(\cdot),\ \sigma_y(\cdot)$	Static input–output (sigmoid) of each population; typical logistic with slope ρ_α and threshold θ_α controlling gain and saturation.
$w_{xx}, w_{xy}, w_{yx}, w_{yy}$	Local coupling weights (E→E, I→E, E→I, I→I). Signs follow (5.2): $-w_{xy}y_i$ implements inhibition of E by I; $-w_{yy}y_i$ self-inhibition of I.
$P_{x,i}$ ($P_{y,i}$)	Tonic drives (bias currents) shifting the operating point along the sigmoids and hence the effective linear gains.
G	Global coupling gain scaling long-range excitation from other regions into x_i.
C_{ij}	Long-range (row-normalized) connectivity weight from region j to i (typically structural; functional/effective or synthetic graphs are alternatives). Enters additively inside σ_x in (5.5).
τ_{ij}	Propagation delay on pathway $j \to i$ (conduction + synaptic latencies); optional.
$\hat{F}_{e;i}(t)$	Exogenous drive (external forcing from nodes or elements outside the network or an electric field, see Eq. (2.12)).
When to Use It	
Use this when explicit excitation–inhibition, saturating gains, and operating-point control are central (Hopf onset, multistability, stimulus responses, seizure-like dynamics). **Assumptions** mean-field population description; first-order E/I kinetics; static sigmoids capturing dendritic saturation and threshold dispersion; long-range inputs summed into E. **Best for** whole-brain simulations with biophysical levers (E/I balance, gains, delays) and macroscopic readouts (FC/FCD, spectra, waves, metastability). **Avoid** if only phase relations matter (prefer Kuramoto) or small-fluctuation linear analytics suffice (prefer linear damped resonators).	
How to Use It	
Provide C (SC by default; FC/EC or synthetic if SC absent), G, local (τ_x, τ_y), ($w_{..}$), σ_α parameters ($\rho_\alpha, \theta_\alpha$), biases $P_{x,i}$ (and optionally $P_{y,i}$), plus optional τ_{ij}, $F_i(t)$, noise. **Defaults** normalize $C \leftarrow C/\lambda_{\max}(C)$; choose $\tau_x > \tau_y$ for gamma-like loops or comparable for alpha/theta; start near Hopf by tuning $P_{x,i}$ and w_{xx} to place the operating point on the steep part of σ_x; Euler/Heun or RK with $\Delta t \leq 1/(100 f_{\max})$. **Readouts** $x_i(t), y_i(t)$ time series; PSD/cross-spectra; FC/FCD; phase–amplitude metrics; wave/cluster structure; operating-point maps (via linearization around (x_0, y_0)).	

5.4. Applications

Historically, the Wilson–Cowan (WILCO) equations were introduced in two seminal papers in the early 1970s to capture the coarse-grained dynamics of interacting excitatory and inhibitory neuronal populations [145,146]. By replacing spikes with smooth population activity and embedding saturating input–output nonlinearities, the framework established a tractable mean-field language for multistability, oscillations, and pattern formation. Later syntheses clarified when the mean-field approximation is valid, how fluctuations and delays can be incorporated, and how WC relates to other neural-mass and field formalisms [147–149].

As a modeling workhorse, WILCO now spans scales — from local microcircuits to whole-brain simulations coupled with connectomes derived from diffusion MRI — precisely because its parameters map cleanly to biology (excitatory/inhibitory gains, operating points, time constants, inputs) while retaining enough nonlinearity to express the canonical dynamical regimes. On the electrophysiology side, delay-coupled WC networks fitted to human MEG reproduce band-limited amplitude-envelope correlations and phase-locking across subjects when equipped with biologically plausible ingredients such as inhibitory synaptic plasticity and heterogeneous conduction delays; they naturally exhibit waxing–waning synchrony (metastability) and predict how changes in E/I balance or propagation speed reshape macroscopic spectra and coupling structure [150]. Related firing-rate analyses show how excitatory and inhibitory feedback loops jointly regulate gamma rhythms—useful for interpreting resonance and entrainment bandwidths observed in M/EEG [151].

For fMRI, WILCO nodes embedded on the structural connectome have been used in multiscale pipelines that connect anatomy to resting-state BOLD statistics and clinical phenotypes. Personalized WC-based models in major depressive disorder, for example, identified executive–limbic dysregulation consistent with empirical FC and symptom profiles [152]. Within *The Virtual Brain* ecosystem, WILCO is a standard regional model for synthesizing MEG/EEG/fMRI observables and

probing how inter-regional coupling, local gains, and delays generate subject-specific variability in FC and its dynamics [153,154]. In task and method-development contexts, WILCO local dynamics frequently serve as the generative "ground truth" for benchmarking estimators of frequency-specific or task-modulated connectivity from MEG/fMRI [155,156].

Because WILCO encodes excitation and inhibition explicitly, it offers a clean bridge to perturbation and inference. In Dynamic Causal Modeling (DCM) for fMRI, replacing the usual bilinear neuronal state equation with a WILCO-type nonlinearity improves model evidence on multiple datasets while preserving physiological interpretability of effective connectivity and local transfer functions [157]. Clinically, introducing a non-monotone (depolarization-block) activation into a single WILCO microcircuit reproduces focal epileptiform activity and its spread, providing mechanistic handles for presurgical hypothesis testing [158]; conversely, disease-specific applications at the whole-brain scale use WILCO oscillators to explore how regional vulnerabilities and synaptic downscaling alter global connectivity and responsiveness [159]. Stochastic variants poised near critical points reproduce avalanche statistics and scaling of spontaneous activity, offering a testbed for hypotheses about critical brain dynamics and their departures under pathology [160–162].

Comparative studies situate WILCO among other whole-brain models. Multi-modal head-to-head work reports that WILCO and SL networks achieve broadly comparable fits to MEG and fMRI benchmarks once conduction delays and local E/I homeostasis are respected; WC often affords advantages on spatiotemporal measures (e.g., functional-connectivity dynamics, the size distribution of transient oscillatory modes) thanks to its explicit rate saturation and E/I partition, whereas SL's normal-form compactness facilitates analytic reductions and turbulence-style analyses [7]. Systematic benchmarking across cohorts further underscores that no single model dominates all metrics: for some summary statistics and parcellations, simpler linear baselines can rival or exceed nonlinear formalisms, and reliability/subject-specificity depend strongly on the targets of fit [163]. In practice, WILCO is most compelling when questions hinge on mechanistic E/I balance, pharmacology, stimulation, seizure dynamics or nonequilibrium signatures; when phase-only timing, graph-spectral tractability or normal-form universality are paramount, Kuramoto/SL (and linear surrogates) may be the better lens. In all cases, WILCO's strengths and limitations are transparent. WILCO is a phenomenological rate model, originally formulated at the population level rather than derived from spiking dynamics: a compact E/I mean-field that is expressive enough to capture oscillations, multistability, and metastability while staying close to the biological levers experiments can manipulate.

6. NMM with second-order synapses (NMM1)

In the Jansen-Rit or NMM1 formalism,[a] synaptic and somatic stages are separated explicitly. Rather than collapsing synaptic dynamics into a single firing–rate equation, NMM1 treats each post-synaptic potential $x(t)$ and $y(t)$ as the output of a biologically grounded linear filter $\hat{L}_\tau$ (with separate rise and decay time constants), sums these to form the membrane perturbation v, and then applies a sigmoidal transfer $S(v)$ to yield the population firing rate. This separation of synapse (impulse-response filters) and soma (sigmoid) provides a clear physiological connection and endows the model with proper delay time scales and intrinsic phase shifts that can sustain oscillations without the need for self-coupling.

The biological ontology includes synapses, post-synaptic potentials (PSPs), the population membrane potential (the perturbation from its baseline), and the transfer function from membrane potential to firing rate output of the population (the sigmoid).

Accordingly, the variables in the equations include the postsynaptic potentials or PSPs (x and y in the E-I model we will discuss), the membrane potential v, the firing rates r_x and r_y, and the sigmoid S. As usual, all dynamical quantities refer to "mean" population averages.

[a] (We use the term here NMM1 to avoid confusion with the specific model of three populations of Jansen and Rit).

The equations in NMM1 are similar to the Wilson–Cowan, but introduce second-order derivatives. Here we present them without self-coupling for simplicity (unlike in WILCO, it is not needed for a stable limit cycle)—see Fig. 6.1(a),

$$\begin{aligned} \tau_x^2\,\ddot{x} + 2\,\tau_x\,\dot{x} + x &= \gamma_x\,\sigma_x\big(-w_{xy}\,y + \hat{F}_e\big), \\ \tau_y^2\,\ddot{y} + 2\,\tau_y\,\dot{y} + y &= \gamma_y\,\sigma_y\big(w_{yx}\,x\big) \end{aligned} \tag{6.1}$$

which can be expressed in operator formalism as

$$\begin{aligned} L_x[x] &= \sigma_x\big(-w_{xy}\,y + \hat{F}_e\big), \\ L_y[y] &= \sigma_y\big(w_{yx}\,x\big) \end{aligned} \tag{6.2}$$

with second order operator notation. For example, for the case of equal rising and decay times,

$$L_\alpha = \frac{1}{\gamma_\alpha}\Big[\tau_\alpha^2\frac{d^2}{dt^2} + 2\tau_\alpha\frac{d}{dt} + 1\Big] \tag{6.3}$$

As in WILCO, the sigmoid function $\sigma(\cdot)$ represents the integration carried out by the "soma" of the population. The argument of the sigmoid is therefore the total membrane perturbation caused by the PSPs from all synapses and other effects, such as electric fields. The γs represent the coupling strength of the synapse — the synaptic gain.

Because the synaptic dynamics are governed by second-order operators (with rise and decay impulse response), the neuronal circuit can sustain oscillations even without explicit self-coupling. Specifically, the second-order filter introduces a frequency-dependent phase shift in the system response. According to the Barkhausen stability criterion, sustained oscillations occur if the total loop gain equals unity and the total loop phase shift reaches an integer multiple of 360°. In a push–pull arrangement — excitatory coupled to inhibitory populations and back — this intrinsic phase shift, arising purely from synaptic kinetics (distinct rise and decay constants), can fulfill the Barkhausen criterion. Thus, unlike the Wilson–Cowan case, even in the absence of explicit self-feedback, second-order dynamics inherently provide the necessary conditions for sustained oscillations. We make this argument precise in the next paragraph.

Why second-order synapses sustain oscillations: the Barkhausen condition. The defining dynamical feature of NMM1 is its capacity to sustain oscillations *without* explicit self-coupling, in contrast to WILCO. The mechanism is most cleanly understood through the classical Barkhausen criterion for closed-loop oscillation, which states that a feedback loop sustains a self-oscillation at angular frequency ω_0 when (a) the loop gain $|G(\mathrm{i}\omega_0)|$ equals unity and (b) the total loop phase shift $\arg G(\mathrm{i}\omega_0)$ is an integer multiple of 2π. In the linear regime around a fixed point, the NMM1 push–pull motif (E→I→E) realizes a closed loop whose loop transfer function reads

$$G(\mathrm{i}\omega) \;=\; -\,w_{xy}\,w_{yx}\,\sigma_x'(v_x^*)\,\sigma_y'(v_y^*)\,L_x(\mathrm{i}\omega)\,L_y(\mathrm{i}\omega), \tag{6.4}$$

where $\sigma_\alpha'(v_\alpha^*)$ is the sigmoid slope at the operating point and $L_\alpha(\mathrm{i}\omega)$ is the frequency response of the second-order synaptic operator (cf. Eq. (6.3). Two features distinguish NMM1 from WILCO here. First, the second-order filter L_α contributes a frequency-dependent phase shift bounded by π, so the two synapses together can supply the full 2π required to close the loop, with the explicit minus sign of the inhibitory pathway providing the remaining π. Second, the rise and decay constants $\tau_{\alpha,r}$, $\tau_{\alpha,d}$ control *both* the magnitude and the phase of $L_\alpha(\mathrm{i}\omega)$, so synaptic kinetics alone determine where the loop-phase condition is met — and hence the resonance frequency. The loop-gain condition then selects the operating point at which oscillations onset through a Hopf bifurcation. The push–pull architecture is in this sense the *minimal* architecture that satisfies the Barkhausen criterion in NMM1: a single population with second-order synapses and no self-coupling cannot supply both the gain inversion and the loop phase. The full algebraic derivation of (6.4) and the explicit oscillation-onset condition are given in Appendix E.3.

6.1. Forcing and coupling

Because of its realistic biological origins, accounting for the effects of coupling to other populations or of an electric field is straightforward: they produce additive voltage perturbation terms to the membrane potential, i.e., the argument of the corresponding sigmoid. So more generally, the equations with multiple synapses in a population reflect the additive combination of synaptic inputs.

The generalization of Eq. (6.2) to *multi-populations node*s and *whole brain models* consists of one for each synapse (m, n) and neuron m,

$$\begin{aligned} \hat{L}_{m\leftarrow n}\big[u_{m\leftarrow n}\big] &= C_{m\leftarrow n}\, r_n \\ v_m &= \Lambda[\hat{E}] + \sum_{n:\, C_{m\leftarrow n}\neq 0} u_{m\leftarrow n} \\ r_m &= \sigma_m\big(v_m\big) \end{aligned} \tag{6.5}$$

(forcing can be represented through synaptic coupling). As before, the first equation transduces connectivity-weighted firing rate inputs into PSPs using the $\hat{L}$ operator, the second sums all the PSPs and other perturbations affecting the neuron (e.g., an electric field in the equation), and the last one produces the firing rate output using the sigmoid.

The first equation links the input firing rate r_n to its associated membrane perturbation (PSP). It can be read as the synapse equation for the input from neuron n to neuron m. The input r_n may also reflect an input to the model from some external neuron, in which case $r_n = f(t)$ for some function (constant, noise, etc.).

The second equation evaluates the membrane potential v_m of neuron m as the sum of the synaptic voltage perturbations plus an electrical field E perturbation (if present) [164].

The last equation is a static transfer function: it evaluates the firing rate of a cell as a function of its total membrane perturbation.

The connectome in Eq. (6.5) includes intra-parcel (defining, e.g., Jansen–Rit or LaNMM nodes) and inter-parcel connectivities in whole-brain models. The latter are usually derived from diffusion MRI or from Ising modeling of fMRI [165].

NMM1 Network (***Eq.*** 6.6)	
Whole-brain Simulations Parameters & Physiological Meaning	
Node i	Neural mass with explicit *synapse* and *soma*: PSP states drive a membrane perturbation v_i, which passes through a sigmoid to yield a firing rate r_i.
$x_i(t),\ y_i(t)$	Excitatory and inhibitory *postsynaptic potentials* (PSPs). They are the outputs of second-order synaptic filters (rise/decay), not directly the rates.
$v_i(t)$	Membrane potential perturbation (sum of PSPs and exogenous terms), i.e., the *input* to the soma/nonlinearity.
$r_{x,i}(t),\ r_{y,i}(t)$	Excitatory/inhibitory *firing rates* (soma outputs). These feed other synapses locally and across the network.
$\sigma_x(\cdot),\ \sigma_y(\cdot)$	Static sigmoids (e.g., logistic) mapping v to firing rate; slope controls effective gain; saturation bounds activity.
$L_x,\ L_y$	Second-order synaptic operators (cf. (6.3)): implement biophysical PSP kinetics with rise/decay; supply intrinsic phase lags that can sustain oscillations.
τ_α, $(\tau_{\alpha,r},\ \tau_{\alpha,d})$	Synaptic time constants (single or separate rise/decay); set resonance frequency and phase lag of each synapse.
γ_α	Synaptic gains (PSP amplitude scale).
$w_{yx},\ w_{xy}$	Local E$\mapsto$I and I$\mapsto$E coupling (push–pull loop); self-coupling often omitted in NMM1 because synaptic phase lags can close the Barkhausen loop.
$\hat{F}_{e;i}(t)$	Exogenous drive (external forcing from nodes or elements outside the network or an electric field)—see Eq. (2.12)).
C_{ij}	Long-range connectivity from node j to i (SC default; FC/EC or synthetic graphs if needed); typically targets the excitatory pathway.
N	Number of nodes (parcels).
When to Use It	
Use this when explicit synaptic kinetics and their phase lags matter (evoked responses, resonance, photic entrainment, band-limited power and envelope dynamics) or when linking parameters to PSP amplitudes/time-constants is essential. **Assumptions** linear synaptic filters (second order) feeding a static nonlinearity; E/I pathways combined at the soma; long-range excitation enters via excitatory synapses. **Best for** EEG/MEG/fMRI generative modeling (spectra and event-related potentials (ERPs)), seizure phenomenology (fast/slow inhibition variants), and whole-brain simulations where synaptic time constants set rhythms. **Relations** near a stable focus it reduces to linear resonators; near Hopf it displays SL-like amplitude–phase dynamics but with biophysical PSP knobs (gains/time-constants). **Avoid** if only relative phase is of interest (Kuramoto) or if closed-form linear statistics suffice (damped linear network).	
How to Use It	
Model (drop-in) use the operator form (6.5) or the E–I pair with coupling (6.6)–(6.7). **Provide** synaptic operators L_α (choose τ_α or $(\tau_{\alpha,r},\ \tau_{\alpha,d})$) and gains γ_α; local couplings w_{yx}, w_{xy}; soma sigmoids σ_α (gain, midpoint, max rate); drives $F_i(t)$ (and optionally $\vec{\lambda}\cdot\vec{E}_i$). **Network** supply C (SC default; FC/EC or synthetic if SC is absent), optional delays τ_{ij}; long-range input enters the excitatory pathway. **Defaults** normalize $C \leftarrow C/\lambda_{\max}(C)$; start with standard JR-style kinetics (faster E than I or vice-versa depending on band); small noise; Euler–Maruyama/RK with $\Delta t \leq 1/(200 f_{\max})$. With non-zero delays $\tau_{ij} > 0$ and stochastic forcing, the system is an SDDE; prefer method-of-steps DDE solvers in the deterministic limit, otherwise use Euler–Maruyama on the delayed system as a controlled approximation with the dual bound $\Delta t \leq \min\{1/(200 f_{\max}),\ \min_{ij}\tau_{ij}/10\}$. **Readouts** PSPs (x_i, y_i), membrane v_i, rates r_i; PSD/cross-spectra and ERPs; envelope/FC/FCD; assess resonance by scanning τ's and gains.	

As a simple network example of inter-parcel coupling from excitatory to excitatory populations in the simple E-I motif model in Eq. (6.2) (with all parcels equal), we have

$$\begin{aligned} L_x[x_i] &= \sigma_x\big(-w_{xy}\, y_i + \hat{F}_{e;i}(t) + \sum_{j\neq i} C_{ij}\, x_j(t-\tau_{ij})\big), \\ L_y[y_i] &= \sigma_y\big(w_{yx}\, x_i\big) \end{aligned} \tag{6.6}$$

with $\hat{F}_e(t)$ as before, including noise or deterministic forcing.

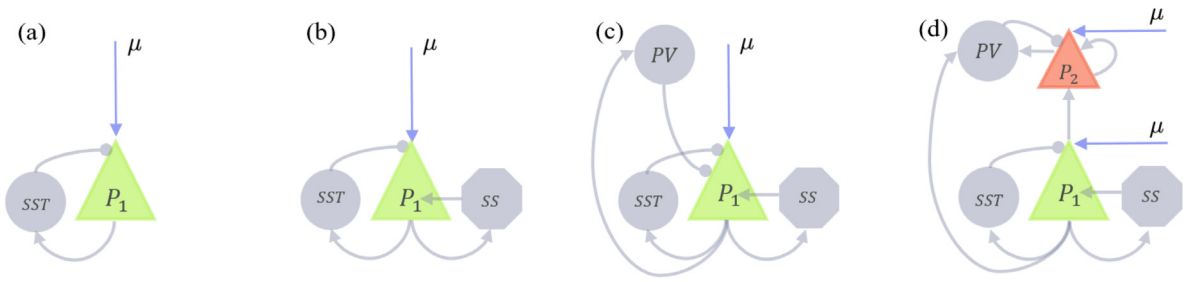

Fig. 6.1. Four models using the second-order formalism: (a) PING-like push–pull motif, (b) Jansen–Rit model [167,168], (c) Wendling model [169], (d) Laminar model [8,170]. Synapses are shown as arrowheads (excitatory) or buttons (inhibitory). Noise or external inputs are indicated on pyramidal cells, although other targets (μ) are also possible.

As a further example, an electric field perturbation can be computed from the local electric field in the population. For example, in the case of weak electric fields at low frequencies (transcranial electrical stimulation), the perturbation is the dot product of the coupling constant $\vec{\lambda}$ and the electric field vector $\vec{E}$ [35–38]. Adding this perturbation to the simple example leads to (see Eq. (2.12))

$$\begin{aligned} L_x[x_i] &= \sigma_x\Big(-w_{xy}\, y_i + f_i(t) + \vec{\lambda}_i \cdot \vec{E}_i(t) + \hat{\eta}_i(t) + \sum_{j\neq i}^{N} C_{ij}\, x_j(t-\tau_{ij})\Big), \\ L_y[y_i] &= \sigma_y\big(w_{yx}\, x_i\big) \end{aligned} \tag{6.7}$$

As with the WILCO networks of Section 5, the rate-based formulation here admits explicit phase reductions back to generalized Kuramoto-type oscillator networks. Forrester et al. [166] derive such a reduction for Jansen–Rit-type NMM1 networks and use it to show how local node dynamics shape the emergent functional connectivity patterns observed in whole-brain simulations, providing the explicit operational bridge between NMM1 and the phase-oscillator descriptions of Section 2.

6.2. Applications

We review canonical models using the second-order synapse formalism (see Fig. 6.1) and summarize their characteristic features and uses.

Simple push–pull motif (PING-like) model

The simplest second-order neural mass captures the push–pull loop between an excitatory and an inhibitory population, the canonical PING motif. Second-order synapses (distinct rise and decay) provide the phase lag needed to meet Barkhausen's condition for sustained oscillations without explicit self-coupling. Minimal two-population models reproduce gamma-band rhythms and noise-sustained oscillations near Hopf; frequency depends mainly on inhibitory decay and E→I gain and can be shifted by drive or kinetics. Applications include modeling high-frequency oscillations (HFOs) at seizure onset [171]; mechanistic context from spiking/mean-field work on PING/ING is reviewed in Buzsáki & Wang (2012) [172] and Tiesinga & Sejnowski (2009) [173], and synchronization analyses such as in Börgers & Kopell (2003) [174] and Whittington et al. (2000) [175].

The Jansen–Rit model

The Jansen–Rit (JR) model [117] comprises three populations (pyramidal, excitatory interneurons, inhibitory interneurons) interconnected with second-order synapses and a static transfer function. It generates alpha-band activity and realistic evoked responses; its regimes (fixed point, alpha, spike-like) are organized by Hopf and other bifurcations [176,177]. JR serves as the neuronal model in Dynamic Causal Modeling (DCM) for M/EEG steady-state and evoked responses [6,178,179], linking synaptic gains/time constants to observed spectra and ERPs.

The model dynamics can be written as

$$\begin{aligned} \hat{L}[y_0] &= Aa\,\sigma(y_1 - y_2), \\ \hat{L}[y_1] &= Aa\,\big(P + C_2\,\sigma(C_1 y_0)\big), \\ \hat{L}[y_2] &= Bb\,C_4\,\sigma(C_3 y_0). \end{aligned} \tag{6.8}$$

The bifurcation diagram of the Jansen–Rit model is shown in Fig. 6.2. Going from left to right, an SN bifurcation creates two unstable fixed points. As the external input P is increased, the system exhibits a subcritical Hopf bifurcation (HB^-); beyond this point, the stability of the fixed point shifts and an unstable limit cycle (depicted in light blue) is created, and

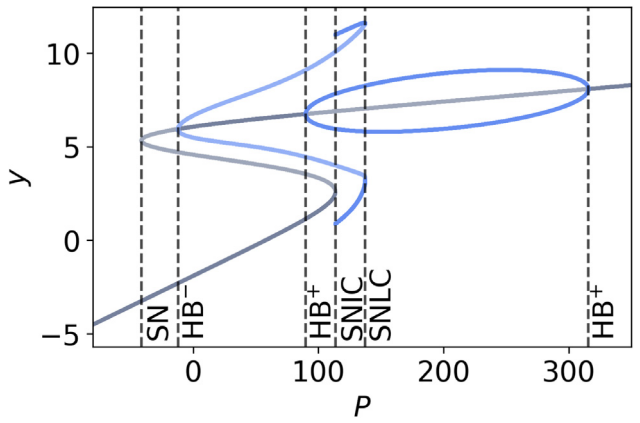

Fig. 6.2. Bifurcation diagram of the Jansen–Rit model (Eq. (6.8)) showing $y = y_1 - y_2$, with bifurcation parameter P. Dark (light) gray lines represent the stable (unstable) fixed points, while the dark (light) blue curves indicate the maximum and minimum amplitudes of the stable (unstable) limit cycles. See Table A.1 for parameters.

the system exhibits two stable fixed points after the HB^- bifurcation. This bistability persists as the system undergoes another Hopf bifurcation, this time a supercritical one (HB^+), where the upper fixed point loses stability and a stable limit cycle emerges. In this regime, the system can display either oscillatory or stationary behavior, depending on its initial conditions. Further increasing P causes the two lower fixed points to collide in a saddle–node on invariant circle (SNIC) bifurcation. Beyond this point, the system exhibits two stable limit cycles, corresponding to oscillations with different frequencies. Eventually, a saddle–node of limit cycles (SNLC) bifurcation occurs, where an outer stable and an unstable limit cycle collide and annihilate, leaving a single remaining limit cycle. This final oscillatory state persists until a last supercritical Hopf bifurcation (HB^+), after which the system returns to a stationary regime.

The Wendling model and its extensions

Wendling's CA1-inspired extension adds fast and slow inhibitory subpopulations ($GABA_A$, $GABA_B$) to the JR scaffold. By tuning inhibitory gains and kinetics, it reproduces background alpha, interictal spikes/spike–waves, and low-voltage fast activity; seizure onset emerges with impaired dendritic inhibition [180]. The model is widely used for interpreting stereo-electroencephalography (SEEG) / EEG patterns, exploring ictogenesis mechanisms, and assessing interventions [181], making it a standard computational tool in epilepsy. Recent extensions include chloride dynamics and laminar integration [182]. *Whole-brain use:* Wendling nodes have been used for resting-state whole-brain network modeling that matches empirical FC [183] and for patient-specific whole-brain simulations of interictal SEEG to aid clinical interpretation [184]. They have been embedded in realistic forward models to synthesize SEEG and personalize local epileptogenic dynamics [182]; the same group reports personalized whole-brain seizure-propagation models that integrate SEEG, MRI, and dMRI to simulate patient-specific responses to surgical, stimulation, and pharmacological interventions within a unified physiological framework [185].

As in the Jansen–Rit model, the core architecture is built around a pyramidal cell population interacting with both SS and SST neurons. The Wendling model extends this structure by introducing a parvalbumin-positive (PV) interneuron population, which both receives input from and projects back to the pyramidal cells. Incorporating this additional inhibitory loop results in the following system of equations:

$$\begin{aligned}
\hat{L}[y_0] &= Ab\,\sigma(y_1 - y_2 - y_3),\\
\hat{L}[y_1] &= Ab\,(P - C_2\,\sigma(C_1 y_0))\,,\\
\hat{L}[y_2] &= Bb\,C_4\,\sigma(C_3 y_0),\\
\hat{L}[y_3] &= Dd\,C_7\,\sigma(C_5 y_0 - C_6 y_2).
\end{aligned} \tag{6.9}$$

The bifurcation diagram in Fig. 6.3 illustrates the steady-state membrane potential of the pyramidal population as a function of its external input P. As P increases, the system undergoes a supercritical Hopf bifurcation (HB^+) at approximately $P \approx 600$, giving rise to oscillations that persist until $P \approx 1750$.

The laminar model (LaNMM)

The laminar neural mass model (LaNMM) [119,120] extends the NMM1 framework to capture the layered organization of cortical microcircuits, addressing observables that single-population JR or Wendling models cannot reach. LaNMM couples two NMM1 generators with distinct anatomical and dynamical roles. A *deep* Jansen–Rit-like generator, situated in infragranular layers, produces alpha/theta-band rhythms through the standard three-population JR architecture. A

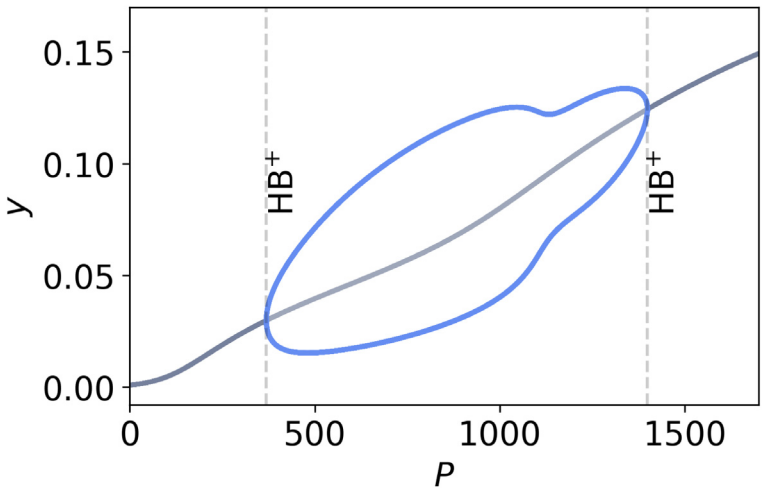

Fig. 6.3. Bifurcation diagram of the Wendling model (Eq. (6.9)) showing $y = y_0$, with bifurcation parameter P. Dark (light) gray lines represent the stable (unstable) fixed points, while the dark (light) blue curves indicate the maximum and minimum amplitudes of the stable (unstable) limit cycles. See Table A.1 for details.

superficial PING-like generator, situated in supragranular layers, produces gamma-band rhythms through the second-order push–pull motif of Section 6. The two generators are coupled according to cortical laminar anatomy, with the deep generator modulating the superficial one through ascending projections that gate gamma amplitude on the slow phase, producing the empirically observed cross-frequency phase–amplitude coupling characteristic of laminar recordings. Because the model is anchored to specific cortical layers, the synthetic local field potential (LFP) and current source density (CSD) signals it generates inherit realistic depth-dependent polarity and phase relations through volume-conduction physics, allowing direct comparison with depth-electrode recordings rather than only with surface EEG/MEG.

Based on the connectivity scheme shown in Fig. 6.1(d), the model is governed by the following system of equations

$$\hat{L}[y_1(t)] = A_A a_A \sigma_{P_1}(C_1 y_2 + C_2 y_3 + C_{11} y_4 + P) \tag{6.10}$$

$$\hat{L}[y_2(t)] = A_A a_A \sigma_{SST}(C_4 y_1) \tag{6.11}$$

$$\hat{L}[y_3(t)] = A_{G_s} a_{G_s} \sigma_{P_1}(C_5 y_1) \tag{6.12}$$

$$\hat{L}[y_4(t)] = A_A a_A \sigma_{P_2}(C_6 y_4 + C_7 y_5 + C_{12} y_1) \tag{6.13}$$

$$\hat{L}[y_5(t)] = A_{G_f} a_{G_f} \sigma_{P_2}(C_9 y_4 + C_{10} y_5 + C_{13} y_1) \tag{6.14}$$

The bifurcation diagram of the LaNMM is shown in Fig. 6.4. It depicts the steady-state membrane potential of the bottom pyramidal population ($v_{P1} = C_1 y_2 + C_2 y_3 + C_{11} y_4 + P$) as a function of its external input (P). The overall structure of the diagram closely resembles that of the Jansen–Rit (JR) model, as expected, since the LaNMM combines features of both the JR and PING models. As the external input increases, the system undergoes a saddle–node (SN) bifurcation where two unstable fixed points emerge. However, unlike the JR model, the LaNMM does not exhibit bistability. Oscillations then arise through a saddle–node on invariant circle (SNIC) bifurcation. Further increases in P lead to a pair of fold-of-limit-cycle (FLC) bifurcations, where the oscillation amplitude decreases while the frequency increases (see [186] for details). This behavior continues until the system passes through a Hopf bifurcation (HB^+). Beyond this point, and in contrast to the JR model, the system undergoes an additional HB^+ bifurcation, associated with the PING mechanism, giving rise to faster oscillatory activity. A systematic bifurcation analysis of the LaNMM identifies the parameter regimes that sustain coupled multifrequency oscillations when an external input is also introduced to the top pyramidal population, in addition to the previously considered input to the bottom population, and determines the conditions under which AD-like alterations disrupt these dynamics [186].

Applications span (i) reproducing laminar spectral peaks and CSD sinks/sources observed in primate and rodent cortex [187–190]; (ii) explaining the cross-frequency coupling signatures observed in laminar recordings; (iii) capturing the alpha-slowing, gamma-loss, and disrupted theta–gamma coupling that characterize the oscillatory phenotype of Alzheimer's disease [191], and the differential effects of psychedelic compounds in AD [192]; (iv) integration with stimulation physics for transcranial electrical stimulation (tES/tACS) studies through coupling to the local electric field as in Eq. (6.7); and (v) deployment as a regional model in connectome-scale simulations to study gamma-band coordination and cooperative/competitive network rhythms [193]. LaNMM has also been used as a generative model for predictive-coding interpretations of laminar dynamics [194].

In the disease-modeling space, modulation of fast-interneuron coupling within LaNMM reproduces the biphasic oscillatory progression of Alzheimer's disease — early hyperexcitability with elevated alpha and gamma power, followed

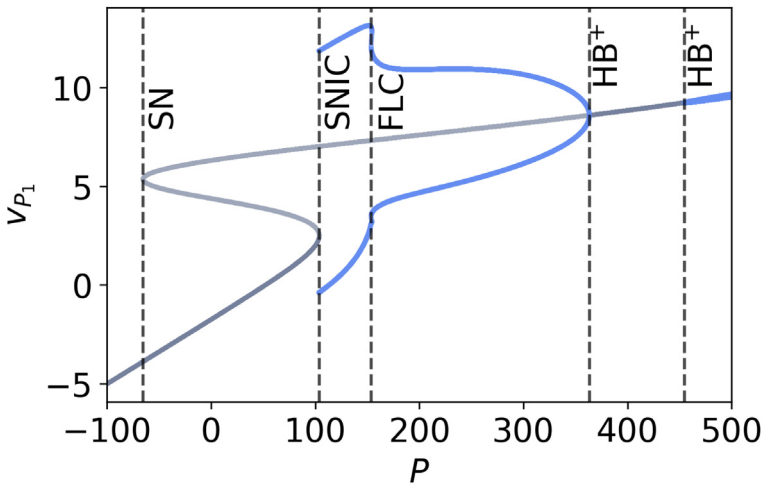

Fig. 6.4. Bifurcation diagram of the LaNMM model (Eq. (6.14)), showing v_{P_1} with bifurcation parameter P. Dark (light) gray lines represent the stable (unstable) fixed points, while the dark (light) blue curves indicate the maximum and minimum amplitudes of the stable (unstable) limit cycles. See Table A.1 for details.

by oscillatory slowing and reduced spectral power consistent with empirical biomarkers [191] — and the corresponding modulation of layer-5 pyramidal excitability characteristic of 5-HT_{2A}-receptor activation reproduces the spectral signatures of serotonergic psychedelics, suggesting a candidate therapeutic axis for the prodromal and early phases of Alzheimer's disease [192].

7. Next-generation models (NMM2)

The neural mass models we have discussed so far, such as the Jansen-Rit, Wendling systems or LaNMM, provide a practical framework for representing and interpreting electrophysiological activity in both local and global brain models [119,134,167,191,195–203]. However, NMM1 mixes biophysically grounded and phenomenological elements: the synaptic operator $\hat{L}$ has direct biophysical content, since its impulse response is set by the kinetics of receptor binding and channel opening and can be matched to recorded post-synaptic potentials [138,204,205], but the static wave-to-pulse sigmoid function [206–208] that maps membrane potential to firing rate rests on a weaker theoretical foundation, having been postulated phenomenologically by Freeman from population recordings rather than derived from spiking dynamics.

Recently, Montbrió et al. [10] derived an exact mean-field theory (MPR) for a population of quadratic integrate-and-fire neurons under some simplifying assumptions, thereby connecting microscale neural mechanisms and meso/macroscopic phenomena.

> The MPR model can be seen to replace Freeman's sigmoid function with a pair of differential equations for the mean membrane potential and firing rate variables—a dynamical relation between firing rate and membrane potential—, providing a more fundamental interpretation of the semi-empirical NMM sigmoid parameters. In doing so, it sheds light on the mechanisms behind enhanced network response to weak but uniform perturbations.
> In the exact mean-field theory, intrinsic population connectivity modulates the steady-state firing rate sigmoid relation in a monotonic manner, with increasing excitatory self-connectivity leading to higher firing rates. This provides a plausible mechanism for the enhanced response of densely connected networks to weak, uniform inputs such as the electric fields produced by non-invasive brain stimulation. This new, "dynamic sigmoid" also endows the neural mass model with a form of "inertia", an intrinsic delay to external inputs that depends on, e.g., self-coupling strength and state of the system.

Models resulting from the MPR mean-field theory can be completed by adding the first or second-order equations for delayed post-synaptic currents and the coupling term with an external electric field [209–211], bringing together the MPR and the usual NMM formalisms into a unified exact mean-field theory (NMM2, for short) displaying rich dynamical features. In the single population model, we show that the resonant sensitivity to a weak alternating electric field is enhanced by increased self-connectivity and slow synapses.

Classical NMMs are *coarse-grained* descriptions: they compress the high-dimensional, spike-resolved dynamics of local circuits into a few mesoscale order parameters (typically, population firing rate and a filtered postsynaptic potential). Conceptually, this follows Kadanoff–Wilson coarse-graining: integrate out fast, microscopic degrees of freedom, retain

slow collective variables, and allow parameters (gains, time constants, noise) to be *renormalized* by the elimination of small scales [212,213]. Empirically, data-driven coarse-graining of population activity can approach non-Gaussian fixed forms with static and dynamic scaling—evidence that mesoscale statistics can be approximately scale-invariant near special operating points [214].

Early NMMs (e.g., Wilson–Cowan, Jansen–Rit) thus combine a biophysically grounded synaptic filter with a phenomenological static nonlinearity — the same split made explicit in the previous paragraph. Population-density and mean-field limits provide a more principled route from spiking to masses [215,216], and field-theoretic expansions make explicit how fluctuations and finite-size effects correct mean-field behavior—precisely the kinds of corrections induced by coarse-graining [217]. In large-scale modeling, these ideas motivate dynamic mean-field reductions of biophysical networks into mesoscale nodes with a few state variables [9].

The mathematical foundation for these exact reductions was laid by the analysis of theta-neuron networks via the Ott–Antonsen ansatz: Luke, Barreto & So [12] provided the complete classification of macroscopic behavior for heterogeneous theta-neuron networks, and So, Luke & Barreto [11] extended this analysis to networks with non-trivial topologies, in both cases obtaining low-dimensional ODEs for collective phase coherence. Because the QIF and theta-neuron models are equivalent under the standard quadratic-to-theta change of variables $V = \tan(\theta/2)$, these reductions and the parallel reduction of QIF networks via the same Ott–Antonsen manifold capture the same macroscopic dynamics expressed in different coordinate systems. Montbrió, Pazó & Roxin [218] (henceforth MPR) reformulated the reduction directly in physiological coordinates — population firing rate $r(t)$ and mean membrane potential $v(t)$ — yielding the two macroscopic ODEs that anchor the present section. The QIF coordinate system is convenient because it expresses the macroscopic dynamics directly in terms of measurable observables (r, v); the theta coordinate system is convenient for the underlying Ott–Antonsen analysis. NMM2 inherits results from both lines of work; see also subsequent reviews and extensions [210,211,219–222]. In the MPR framework, the steady-state relationship between firing rate r and mean voltage v defines a *sigmoid-type* input–output curve (i.e., a static transfer function). However, when the full two-dimensional dynamical system is considered (with $r(t)$ and $v(t)$ evolving in time), the effective gain becomes *state- and history-dependent*, rather than being a fixed static curve.

Positive self-coupling (J) shifts fixed points to higher rates and can bring the system closer to resonant/oscillatory regimes, aligning with the intuition that denser local recurrence enhances responsiveness to weak, spatially uniform drives (e.g., uniform electric fields) [218,223]. Exact mean-field extensions capture synaptic filtering, electrical coupling, and other biophysics [209–211], and have been leveraged to model working-memory circuits with short-term plasticity [224].

NMM2 can be read as a principled *coarse-grained* synthesis: it replaces Freeman's static nonlinearity by the MPR *dynamic* firing-rate relation, and *completes* it with biophysical synaptic filters (e.g., second-order α-synapses) and exogenous field coupling. In renormalization group (RG), r and v are the relevant mesoscale variables; synaptic and coupling parameters are effective (*renormalized*) couplings that depend on the level of coarse-graining and circuit state. This yields (i) a physics-based "dynamic sigmoid" with inertia and state-dependent gain, (ii) a transparent link between microparameters (η, Δ, J) and mesoscale responsiveness, and (iii) a natural path to incorporate fluctuation corrections when needed (finite-size, correlations) [217].

In their uniform, mean-field derivation for a population of N quadratic integrate and fire (QIF) neurons, Montbrió et al. [10] start from the equations for the neuron membrane potential perturbation from baseline,

$$\dot{V}_j = V_j^2 + \eta_j + Js(t) + I(t), \text{ if } V_j \geq V_p, \text{ then } V_r \leftarrow V_j \tag{7.1}$$

In this equation, the total input current in neuron j is $I_j = \eta_j + Js(t) + I(t)$ and includes a quenched noise constant component η_j drawn from a Lorentzian (Cauchy) distribution, the input from other neurons $s(t)$ per connection received (the mean synaptic activation) with uniform coupling J, and a common input $I(t)$. The common input $I(t)$ can represent both a common external input or the effect of an electric field, e.g.,

$$I(t) = p(t) + \vec{\lambda} \cdot \vec{E}(t) \tag{7.2}$$

for weak electric fields. Here $p(t)$ is an external uniform current, and λ is the dipole conductance term in the spherical harmonic expansion of the response of the neuron to an external, uniform electric field. This is a good approximation if the neuron is in its subthreshold, linear regime and can be computed using realistic compartment models of the (see, e.g., [225,226]).

The mean synaptic activation is given by

$$s(t) = \frac{1}{N} \sum_{j=1}^{N} \sum_{k|t_j^k<t} \int_{-\infty}^{t} dt' \, a_\tau(t - t') \, \delta(t' - t_j^k) \tag{7.3}$$

where t_j^k is the arrival time of the kth spike from the jth neuron, and $a(t)$ the synaptic activation function, e.g., $a(t) = e^{-t/\tau}/\tau$. Note that we can write $J = j \cdot N$, where j is the synapse coupling strength (charge delivered to the neuron per action potential at the synapse) of each synapse the cell receives from the network (there are N of them in a fully connected architecture with N neurons).

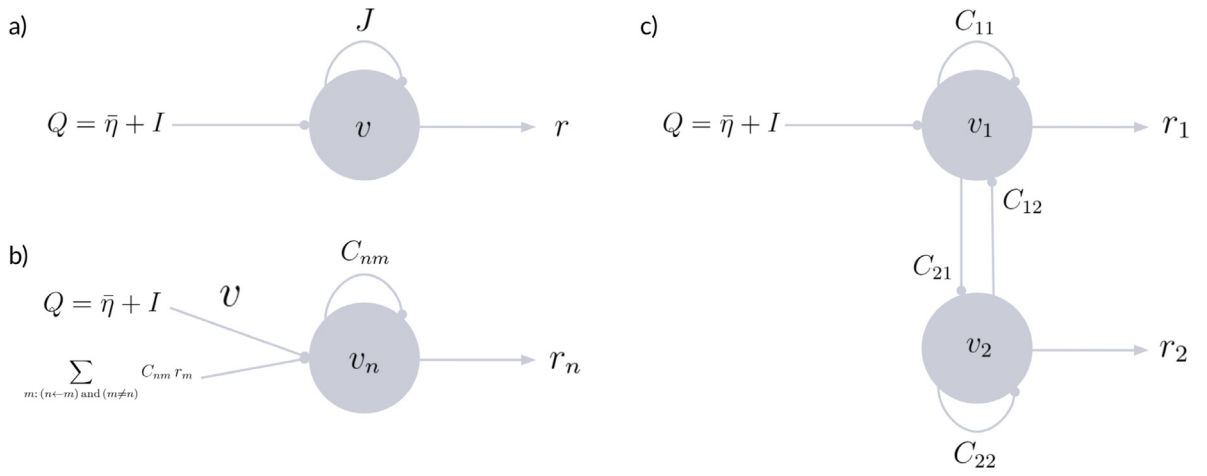

Fig. 7.1. NMM2 diagrams. (A): Diagram for self-coupled population with connectivity J receiving and external input Q. (B): generalization for multiple populations. (C): A generic two-population model.

We assume here, for simplicity, that all neurons are equally oriented with respect to the electric field. If the electric field is constant, variations in orientation can be absorbed by the quenched noise term. The total input $p(t)+\vec{\lambda}\cdot\vec{E}(t)+J\,s(t)$ is thus homogeneous across the population (does not depend on the neuron).

Starting from these, Montbrió et al. derive an effective theory *for a single population* in the large N limit (Eq 12 in [10]),

$$\dot{r} = \Delta/\pi + 2rv \tag{7.4}$$

$$\dot{v} = v^2 - \pi^2 r^2 + J\,s + \bar{\eta} + I(t) \tag{7.5}$$

To this equation, we add the usual operator dynamics for the synapse activation,

$$\hat{L}_s[s] = r, \text{ or, equivalently, } s = \hat{K}_s[r] \tag{7.6}$$

(see Fig. 6.1 (A)). Here v and r are the population mean membrane potential and firing rate, respectively. The new parameters $\bar{\eta}$ and Δ refer to the center and half-width-at-half-maximum (HWHM) of the Lorentzian (Cauchy) distribution for the quenched noise input η_j. Note that the Lorentzian distribution does not admit moments of order ≥ 1 in the conventional sense (the integral defining the mean is divergent), so $\bar{\eta}$ is a location parameter rather than an expectation; under the Cauchy principal value, $\bar{\eta}$ formally equals the median. The analysis in [10] hinges on the assumptions of all-to-all uniform connectivity (with synaptic weight J) and common input $I(t)$.

These equations can be read as a transfer functional mapping input currents into an output firing rate, as in the master NMM Eq. (4.20),

$$\begin{aligned} r &= \hat{\Phi}_m[J\,s + I(t)]\,, \\ s &= \hat{K}_s[r]. \end{aligned} \tag{7.7}$$

The transfer functional is captured by Eq. (7.4). For a self-coupled inhibitory population (ING) with second-order synapses, the system of equations reads

$$\begin{aligned} \tau_m \dot{v} &= \bar{\eta} - (\pi r \tau_m)^2 + v^2 - \tau_m\,(J_{ii} s) + I \\ \tau_m \dot{r} &= \Delta + 2rv \\ \tau_s \dot{s} &= z \\ \tau_s \dot{z} &= r - 2z - s \end{aligned} \tag{7.8}$$

where τ_s is the synaptic time constant, and where we explicitly introduce τ_m, the membrane constant of the population [211].

7.1. Forcing and coupling

Forcing and coupling are natural in this model, inheriting naturally from the single neuron biophysics in Eq. (7.1) through the term $I(t)$. We converge here on the notation used in Eq. (2.12), where $\hat{F}_e$ represents the input external to the network.

E-I push–pull motif. For two coupled populations (see Fig. 7.1), we have the six equations

$$\begin{aligned}
\tau_x \dot{r}_x &= \Delta_x/(\pi\tau_x) + 2 r_x v_x, \\
\tau_x \dot{v}_x &= v_x^2 + \bar{\eta}_x + \tau_x J_x s_x - (\pi r_x \tau_x)^2 - \tau_x C_{xy} s_y + I + \hat{F}_{e;x}, \\
s_x &= \hat{K}_x[r_x], \\
\tau_y \dot{r}_y &= \Delta_y/(\pi\tau_y) + 2 r_y v_y, \\
\tau_y \dot{v}_y &= v_y^2 + \bar{\eta}_y - \tau_y J_y s_y - (\pi r_y \tau_y)^2 + \tau_y C_{yx} s_x, \\
s_y &= \hat{K}_y[r_y].
\end{aligned} \tag{7.9}$$

with $\tau_{x,y}$ the membrane time constants of each population. The sign conventions follow the rest of the manuscript: $J_x > 0$ denotes excitatory self-coupling within the E population, $J_y > 0$ denotes inhibitory self-coupling within the I population (entering with an explicit minus sign in the $\dot{v}_y$ equation), and $C_{yx} > 0$, $C_{xy} > 0$ denote the magnitudes of the cross-couplings (E→I positive, I→E negative as a consequence of the explicit minus in the $\dot{v}_x$ equation). The forcing term $\hat{F}_{e;x}$ enters only the excitatory population, consistent with the convention used throughout this review. In operator form, following Eq. (7.7), we express the complete set more compactly,

$$\begin{aligned}
r_x &= \hat{\Phi}_x[\tau_x(J_x s_x - C_{xy} s_y) + \hat{F}_{e;x}], \quad & s_x &= \hat{K}_x[r_x]. \\
r_y &= \hat{\Phi}_y[\tau_y(-J_y s_y + C_{yx} s_x)], & s_y &= \hat{K}_y[r_y],
\end{aligned} \tag{7.10}$$

where, as usual, we drive only the excitatory population. The push–pull motif is present through the nonlinearity.

General equations for multiple coupled populations. The general equations for multiple interacting populations become

$$\begin{aligned}
\tau_n \dot{r}_n &= \frac{\Delta_n}{\pi\tau_n} + 2 r_n v_n \\
\tau_n \dot{v}_n &= v_n^2 - (\pi r_n \tau_n)^2 + \bar{\eta}_n + \hat{F}_{e;n} + \tau_n \sum_{m:n\leftarrow m} C_{nm} s_{nm} \\
s_{nm} &= \hat{K}_{nm}[r_m]
\end{aligned} \tag{7.11}$$

or

$$\begin{aligned}
r_n &= \hat{\Phi}_n[\tau_n\big(J_n s_n + \sum_{m:n\leftarrow m} C_{nm} s_{nm}\big) + \hat{F}_{e;n}], \\
s_{nm} &= \hat{K}_{nm}[r_m]
\end{aligned} \tag{7.12}$$

Equations for coupled E-I push–pull motif. We can also write equations for multiple E-I motif as in the previous sections, where each E-I motif is identical and we only connect excitatory to excitatory populations (with, e.g., $J_x = C_{xx}$ and only two types of synapses),

$$\begin{aligned}
\tau_x \dot{r}_x^{(i)} &= \frac{\Delta_x}{\pi\tau_x} + 2 r_x^{(i)} v_x^{(i)}, \\
\tau_x \dot{v}_x^{(i)} &= \big(v_x^{(i)}\big)^2 - \big(\pi r_x^{(i)} \tau_x\big)^2 + \bar{\eta}_x + \tau_x\Big(C_{xx} s_x^{(i)} - C_{xy} s_y^{(i)} + \sum_{j\neq i} C_{ij} s_x^{(j)}\Big) + \hat{F}_e^{(i)}, \\
s_x^{(i)} &= \hat{K}_x\big[r_x^{(i)}\big], \\
\tau_y \dot{r}_y^{(i)} &= \frac{\Delta_y}{\pi\tau_y} + 2 r_y^{(i)} v_y^{(i)}, \\
\tau_y \dot{v}_y^{(i)} &= \big(v_y^{(i)}\big)^2 - \big(\pi r_y^{(i)} \tau_y\big)^2 + \bar{\eta}_y + \tau_y\Big(-C_{yy} s_y^{(i)} + C_{yx} s_x^{(i)}\Big), \\
s_y^{(i)} &= \hat{K}_y\big[r_y^{(i)}\big].
\end{aligned} \tag{7.13}$$

All coupling magnitudes are taken non-negative, $C_{\alpha\beta} \geq 0$; the signs in the voltage equations encode the dynamical role of each connection: + for excitatory drive (C_{xx} self-recurrence, C_{yx} E→I, long-range C_{ij} for E→E) and − for inhibitory drive (C_{yy} self-recurrence, C_{xy} I→E). The swap-and-flip rule from the excitatory (x) to the inhibitory (y) population is then read directly off the equations: swap the population index and flip the sign of each cross-coupling term according to the role (excitatory vs. inhibitory) it plays in the receiving population.

The bifurcation diagram of Eq. (7.8) is shown in Fig. 7.2. It illustrates the steady-state firing rate r as a function of the external input I. As in the previous models, increasing the external input induces a transition from a stable fixed point to oscillatory activity via a supercritical Hopf bifurcation (HB^+). The resulting limit-cycle oscillations persist over a range of input values and are terminated at a second HB^+, with both bifurcation points indicated by the vertical dashed lines.

The bifurcation diagram of Eq. (7.9), which yields a PING model, is shown in Fig. 7.3. It depicts the steady-state firing rate as a function of the external input (I). From left to right, as the external input increases, the system first undergoes a pair of saddle–node (SN) bifurcations, indicating the creation and annihilation of fixed points. Following these, the system experiences a supercritical Hopf bifurcation (HB^+), giving rise to stable oscillatory dynamics. The resulting limit-cycle oscillations persist over a range of input values until the system passes through another HB^+ bifurcation, at which the oscillations disappear and the system returns to a stable fixed point.

NMM2 Network (***Eq.*** (7.11))	
Whole-brain Simulations Parameters & Physiological Meaning	
Node n	Neural mass with explicit *synapse* and *soma*: PSP states drive a membrane perturbation s_{nm}, which adds, with others, to v_n and passes through a sigmoid to yield a firing rate r_n.
$r_i(t)$	Population firing rate (Hz or normalized).
$v_n(t)$	Mean membrane potential.
$\tau_{m,x,y},\ \tau_s$	Membrane and synaptic time constants.
$\bar{\eta}_n,\ \Delta_n$	Center (location parameter) and HWHM of the Lorentzian excitability distribution (bias and heterogeneity of population elements). Larger Δ_n broadens dispersion and damps coherence.
J_n	Local recurrent self-coupling of population n (excitatory $J_n > 0$; inhibitory $J_n < 0$) scaling the node's own synaptic self-current s_{nn}. Tunes resonance and distance to oscillatory regimes.
$s_{nm}(t)$	Synaptic activation from presynaptic population m to n; obtained by filtering r_m: $s_{nm} = \hat{K}_{nm}[r_m]$.
$\hat{K}_{nm}$	Synaptic filter (first- or second-order). E.g., for equal rise/decay: $\hat{K}[r]$ solves $\gamma^{-1}(\tau^2\ddot{s} + 2\tau\dot{s} + s) = r$; with distinct rise/decay use (τ_r, τ_d).
$\gamma_{nm},\ \tau_{nm}$	Synaptic gain and time constants (set per synapse type: AMPA/NMDA/$GABA_A$/$GABA_B$); determine amplitude, lag and band-selectivity.
C_{nm}	Long-range coupling weight from m to n (SC by default; FC/EC or synthetic graphs if needed).
t_{nm} (opt.)	Propagation delay on pathway $m \to n$; introduces frequency-dependent phase lags. Use by replacing $s_{nm}(t)$ by $s_{nm}(t - t_{nm})$ in Eq. (7.11).
N	Number of nodes/populations.
$\hat{F}_e^{(i)}(t)$	Exogenous drive (external forcing from nodes or elements outside the network or an electric field)—see Eq. (2.12)).
When to Use It — Next-Generation Neural Mass (NMM2)	
Use this when you need a *first-principles* link from spiking microdynamics to mesoscale variables: a dynamic "sigmoid" (r–v equations) with state-dependent gain/inertia, principled effects of self-coupling J, and clean integration of synaptic filtering and uniform field inputs.	
Assumptions all-to-all recurrence within each population, QIF spike mechanism, Lorentzian heterogeneity (MPR exactness), chemical synapses via $s = \hat{K}[r]$; extensions cover electrical synapses and plasticity.	
Best for analytic studies of resonance/entrainment to weak uniform drives (tACS-like), comparisons to heuristic NMMs.	
Avoid if a static transfer is sufficient and parameters must map directly onto classic NMM1 fits; or if detailed channel/compartment biophysics is required (prefer conductance-based masses).	
How to Use It — Minimal Guide (NMM2 Network)	
Provide $(\bar{\eta}_n, \Delta_n), J_n$; synaptic filters $\hat{K}_{nm}$ with (τ, γ) (or (τ_r, τ_d, γ)); network C_{nm} (SC/FC/EC or synthetic), optional delays t_{nm}; external $p_n(t)$ or field term $\vec{\lambda}_n \cdot \vec{E}_n(t)$.	
Defaults start from JR-style kinetics (use Table 4.1 for AMPA/NMDA/GABA ranges); row-normalize C and (optionally) scale by a global gain; initialize (r_n, v_n) near the desired fixed point; With non-zero delays $\tau_{ij} > 0$ in the network coupling and stochastic forcing in $\hat{F}_{e;n}$, Eqs. (7.11)–(7.13) are SDDEs and inherit the caveats discussed in Section 2: prefer method-of-steps DDE solvers in the deterministic limit; if a fixed-step Euler–Maruyama scheme is used on the delayed system as a controlled approximation, satisfy both the oscillation-resolution bound $\Delta t \leq 1/(200 f_{\max})$ and the delay-resolution bound $\Delta t \leq \min_{ij} \tau_{ij}/10$, verify convergence by step halving, and report the discretization scheme, interpolation on the delay buffer, and random number generator (RNG) seed alongside other simulation parameters.	
Readouts $r_n(t)$, $v_n(t)$, and $s_{nm}(t)$; PSD/cross-spectra; envelope/FC/FCD; resonance curves vs. J, τ and field amplitude; operating-point maps from the r–v nullclines.	

7.2. Applications

The NMM2 formalism has begun to power a range of concrete applications:

1. **Emergence of brain rhythms**: Several works have analyzed models based on the MPR theory to explore motifs allowing for the emergence of fast collective oscillations in one or two neural populations. The simplest instances include a single population of inhibitory neurons with synaptic delays [209,227–229], and excitatory–inhibitory population pairs [223,227,230–232].

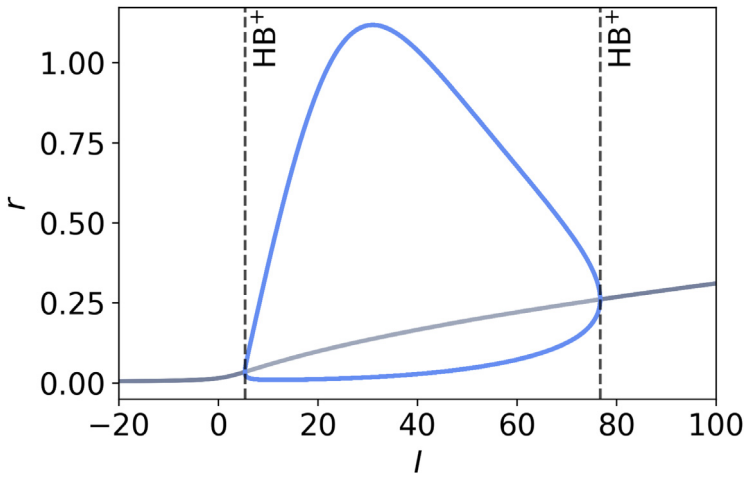

Fig. 7.2. Bifurcation diagram of the interneuron-gamma (ING) NMM2 self-coupled model (Eq. (7.8)) with bifurcation parameter I. Dark (light) gray lines represent the stable (unstable) fixed points, while the dark (light) blue curves indicate the maximum and minimum amplitudes of the stable (unstable) limit cycles. See Table A.1 for details.

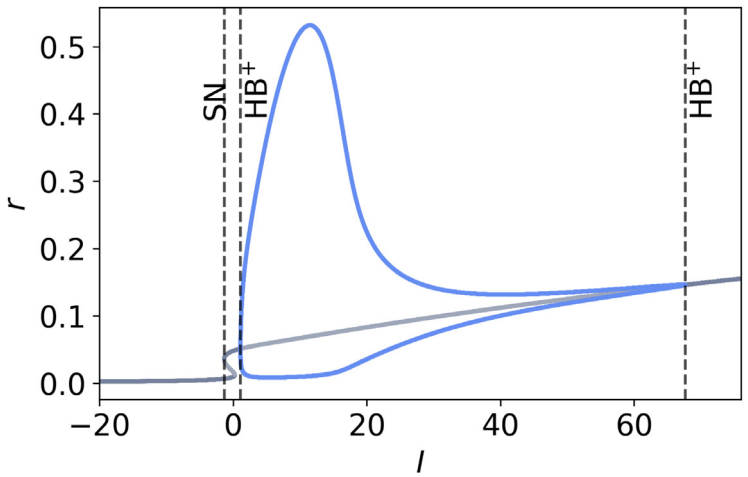

Fig. 7.3. Bifurcation diagram of the pyramidal-interneuron (PING) NMM2 model with bifurcation parameter I (Eq. (7.9)). Dark (light) gray lines represent the stable (unstable) fixed points, while the dark (light) blue curves indicate the maximum and minimum amplitudes of the stable (unstable) limit cycles. See Table A.1 for details.

2. **Whole-brain modeling**: Next-generation neural masses embedded on human connectomes offer an improved framework to analyze and reproduce brain dynamics captured by fMRI. Some works have started to explore this venue, focusing on capturing pathology and healthy states [233–236] and performing detailed mathematical analyses for the emergence of complex spatiotemporal behavior [229,237].
3. **Non-invasive stimulation theory**: Because NMM2 replaces a static sigmoid with dynamic firing-rate equations, it predicts state-dependent field sensitivity. With second-order synapses, it explains enhanced resonant responses to weak uniform AC electric fields (tACS-like) and how self-coupling and synaptic time constants tune this sensitivity [211]. Relatedly, NMM2 has been used to study population responses to brief exogenous pulses (TMS-like) and ERD/ERS phenomena [223,238].
4. **Cognition**: Exact mean-field models reproduce working-memory operations and associated oscillatory signatures, providing a coarse-grained yet mechanistic account [239,240].
5. **Neuromodulation and DBS**: Extensions that include adaptation/neuromodulatory variables have been used to explore mechanism-level effects of deep brain stimulation and dopamine on network dynamics [241,242].

Additionally, several works have put forward extensions to the MPR theory to increase its range of applicability by challenging some of the simplifying assumptions of the QIF formulation (7.1). Paired with synaptic dynamics, these extensions provide even further refined versions of NMM2:

1. **Dynamic noise**: Originally, the only source of microscopic disorder in the QIF formulation (7.1) was through the quenched variables η_j. Nonetheless, the exact mean-field theory also applies if $\eta_j(t)$ are considered to be dynamic Cauchy white noise [243]. Additionally, approximation theories exist for the case of Gaussian white noise [244,245].
2. **Quenched noise distribution**: The MPR theory requires η_j to be Lorentzian-distributed to obtain a closed low-dimensional model for r and v. Recent work generalized the theory to include q-Gaussian distributions, at the expense of increasing the number of independent variables in the resulting neural mass [246,247].
3. **Gap-junctions**: The MPR theory also applies for neurons communicating via electrical synapses mediated by gap-junctions and other diffusion-based coupling [44,248]. This allows for deriving NMM2 including electrical coupling, a major breakthrough considering that heuristic formulations cannot account for this microscopic effect.
4. **Adaptation variables**: In spite of its significance, the QIF model is a simplified model for neuron dynamics. Further biophysical mechanisms in the single unit dynamics, such as spike-frequency adaptation or ion channel dynamics, require the inclusion of additional dynamical variables for which the exact mean-field theory might not apply. To address this problem, some works propose including a mean-field adaptation as an approximation to networks with single unit adaptation [249,250]. A recent approach, instead, proposes including a suitable form of spike-frequency adaptation for which the MPR still holds exactly [251]. Beyond the QIF/theta line, Nicola & Campbell [252] derived an approximate mean-field reduction for heterogeneous networks of two-dimensional integrate-and-fire neurons.
5. **Full low-dimensional theory**: The MPR theory, which is strongly related to the Ott–Antonsen ansatz for the Kuramoto model [253], poses some challenging theoretical questions. The most relevant of them asks whether the low-dimensional manifold is attracting in the microscopic representation. A rigorous theoretical framework has been proposed recently, demonstrating that this is indeed the case provided the single units are not all identical ($\Delta > 0$) [254].
6. **Finite and asymmetric spikes**: The original theory requires QIF neurons with a spike apex and reset at $V_{\text{peak}} = -V_{\text{reset}} = \infty$. This poses a limitation resulting neural mass model, especially when gap-junctions are included. Montbrió and Pazó [255] introduced a model accounting for spike asymmetry in order to properly capture these effects in networks with gap junctions. Recently, Cestnik [256] extended the exact low-dimensional reduction to a two-phase model capturing the dynamics for neurons with finite spikes ($|V_{\text{peak}}|, |V_{\text{reset}}| < \infty$).

8. Summary and outlook

We have treated neural mass models as points on a continuous ladder connecting microscopic spiking descriptions to macroscopic whole-brain dynamics. Griffiths, Bastiaens & Kaboodvand [257] organize the same space along an orthogonal axis — spatial scale (cells → circuits → networks), whereas the present review uses the derivation–representation axes summarized in Fig. 8.1. The two organizations are complementary.

At the lowest rung, the harmonic and Stuart–Landau (SL) oscillators provide the normal-form language for local rhythms and their phase–amplitude structure. Wilson–Cowan (WILCO) models make the underlying excitatory–inhibitory push–pull architecture explicit and introduce sigmoidal transfer functionals as coarse-grained summaries of neuronal input–output relations. Second-order synaptic neural mass models (NMM1) add realistic synaptic filters with distinct rise and decay constants, thereby separating synapse from soma dynamics and producing realistic postsynaptic potentials, delays and phase shifts. Finally, next-generation models (NMM2) derived exactly from quadratic integrate-and-fire (QIF) networks close the loop from spikes to masses by replacing static sigmoids with analytically derived dynamic (r, v) transfer equations, showing how population firing rates and mean membrane potentials evolve jointly under recurrent and external drive [211,218–220].

A main message is that all these formalisms share a simple core: a push–pull motif between two effective degrees of freedom, coupled through linear filters and nonlinear transfer functions, and embedded in a network via structured coupling and delays. In the linear limit, this core reduces to damped resonators or complex Ornstein–Uhlenbeck processes, for which covariances and spectra can be obtained in closed form and mapped onto empirical functional connectivity [79,86]. Close to Hopf, SL-like normal forms capture the onset of self-sustained oscillations, metastability, and turbulence-like dynamics under connectome coupling [85,99,202]. WILCO and NMM1 add biophysical levers (synaptic gains, time constants, E/I balance, laminar circuits) without losing this dynamical structure, and NMM2 shows that, at least for QIF networks, these macroscopic descriptions can be derived exactly rather than postulated.

Looking ahead, one natural direction is to extend exact mean-field reductions beyond QIF neurons. Current next-generation neural mass models exploit specific analytic properties of the QIF nonlinearity and Lorentzian excitability distributions [218,219]. A major open problem is to obtain similarly low-dimensional closures for more realistic single-cell models, such as exponential integrate-and-fire or multi-variable Hodgkin–Huxley-type neurons, possibly via systematic approximations (e.g. moment closures, population-density expansions, or renormalization-group inspired coarse graining) [215,217,244]. Such derivations would clarify which aspects of spiking physiology (e.g. spike-frequency adaptation, active dendrites, NMDA currents) survive coarse graining and how they renormalize effective gains, time constants, and non-Gaussian noise at the neural-mass level.

A second axis concerns more realistic local circuits. Laminar neural mass models already capture distinct deep and superficial generator loops and their contribution to laminar LFP, CSD, and cross-frequency coupling [8,119]. Next steps include: (i) explicitly modeling multiple inhibitory subtypes (PV, somatostatin (SOM), vasoactive intestinal peptide (VIP))

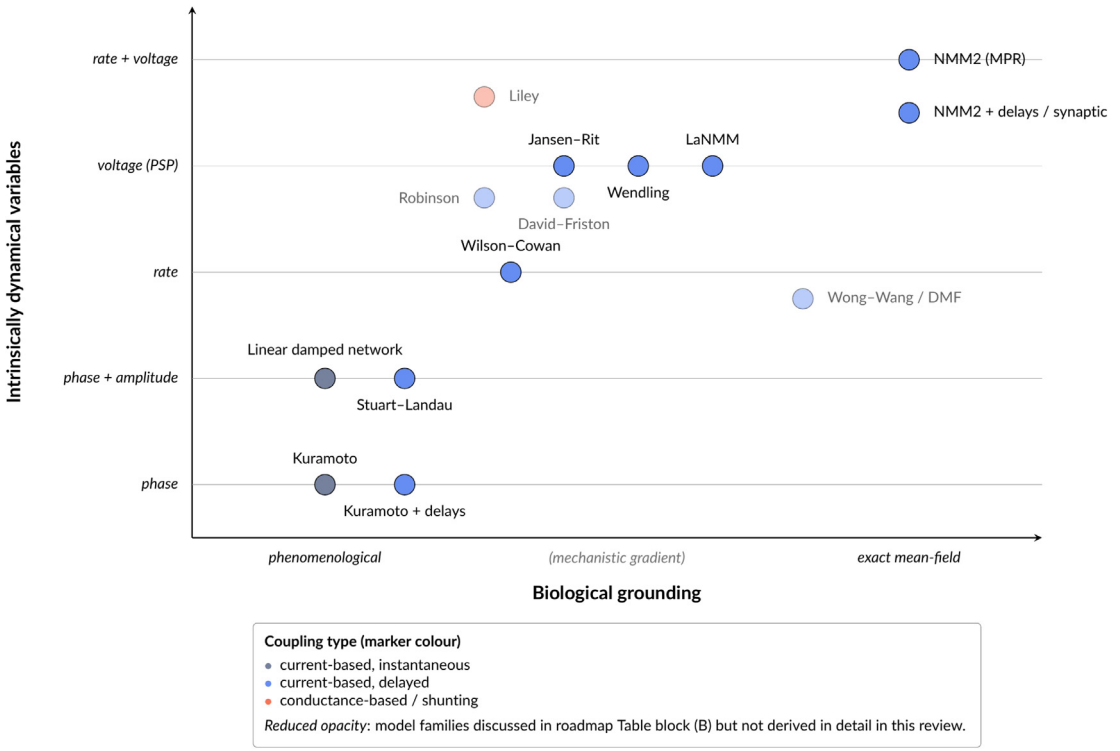

Fig. 8.1. Rosetta map of neural-mass and mean-field model families discussed in this review. The horizontal axis orders models along a mechanistic gradient, from purely phenomenological constructions (chosen to capture observed dynamics with minimal commitment to mechanism) to exact mean-field reductions (linked to underlying spiking dynamics via formal derivation, e.g., the Lorentzian ansatz of MPR). The vertical axis tracks the *intrinsically dynamical* variables, i.e., those that carry their own ODE, not the full set of state variables that appear in the equations. Wilson–Cowan sits at "rate" because only the rate variable has its own derivative; Jansen–Rit, Wendling, LaNMM, David–Friston, Liley and Robinson sit at "voltage (PSP)" because the post-synaptic potential filter supplies the dynamical equation while rate enters instantaneously through the sigmoid; NMM2 (MPR) and its delayed/synaptic extensions occupy "rate + voltage" because both variables have explicit ODEs. Wong–Wang/DMF is placed at "rate" because its gating variable evolves on synaptic timescale with first-order rate-like dynamics. Marker color encodes coupling type: current-based instantaneous, current-based with delays, and conductance-based/shunting. Models referenced in roadmap Table block (B) but not derived in detail in this review are shown at reduced opacity. Horizontal positions between the two endpoints are illustrative and reflect relative mechanistic specificity rather than a quantitative scale. The linear-versus-nonlinear coupling distinction is absorbed into model identity rather than encoded separately, and is discussed in Section 4.2.

with layer-specific projections; (ii) incorporating both chemical and electrical synapses in a unified mean-field description; and (iii) embedding short-term synaptic plasticity and intrinsic adaptation into next-generation masses in an exact or controlled approximate way [209,224,249]. These refinements would allow laminar models to speak more directly to cell-type and layer-resolved data, calcium imaging, and perturbation experiments, and to test hypotheses about how microcircuit motifs implement canonical computations (e.g., gain control, winner–take–all, and gating).

At the whole-brain scale, three modeling ingredients become increasingly important. First, heterogeneity across regions: empirical work shows that cortical areas differ systematically in local time scales, recurrent excitation, and laminar architecture, which in turn shape their role in large-scale hierarchies [258,259]. Future models should assign region-specific parameters (e.g., SL working points, WILCO gains, NMM1/NMM2 synaptic kinetics) informed by cytoarchitectonics, gene expression, and receptor densities, rather than using identical nodes everywhere. Second, directed and laminar-specific coupling: predictive-processing accounts suggest that feedforward and feedback pathways are implemented via distinct layers, with frequency-specific channels (gamma/beta) carrying prediction errors and predictions [260,261]. Embedding laminar neural masses in directed structural connectomes with frequency-dependent effective connectivity is a natural route to test such proposals against MEG/EEG and laminar recordings. Third, more refined parcellations and subcortical circuits: incorporating high-resolution cortical atlases (e.g. Glasser multimodal 360-area parcellation and its extensions) [262] and explicit thalamic, basal ganglia, and cerebellar masses [259,263,264] will be essential to capture cortico–subcortical loops that shape rhythms, state transitions, and neuromodulatory control.

Neuromodulatory systems provide a complementary, low-dimensional control axis over the same large-scale circuits. Gradients of receptor densities and gene expression co-localize with the structural and timescale hierarchies described above, suggesting that neuromodulatory tone shapes regional gain, effective time constants, and long-range coupling in a spatially specific way [265,266]. From a modeling standpoint, even when neuromodulatory nuclei are not explicitly represented, their effects can be approximated by treating external drives and gain parameters as proxies for neuromodulatory

axes—for example, using global or projection-specific changes in background input, SL working points, or WILCO gains to implement neuromodulation-like shifts in E/I balance, integration time and noise statistics, in line with classical circuit-level neuromodulation work [267]. Recent whole-brain modeling incorporates neurotransmission-weighted connectivity to account for a wide repertoire of task-evoked states, showing that neuromodulator-dependent changes in effective coupling can reproduce diverse cognitive configurations within a single structural scaffold [268]. These findings motivate configuring "external inputs" in large-scale models using receptor and gene-expression maps, or fitting low-dimensional neuromodulatory control variables to match state transitions induced by pharmacological, arousal, or task manipulations.

We see two further connections, with statistical inference and with information-theoretic analyses of state. Linear and SL-based whole-brain models already support perturbation-based measures of nonequilibrium, susceptibility, and information routing across states (wake, sleep, anesthesia, psychedelics) [85,99,101]. NMM1 and NMM2 provide richer, mechanistically grounded arenas in which to define and compute such quantities, including algorithmic-information or compression-based characterizations of oscillatory dynamics. Coupling these models to modern inference frameworks (variational data assimilation, Bayesian model comparison, active inference) can turn them into forward models for multimodal data (fMRI, M/EEG, SEEG, laminar probes) and for in silico perturbation experiments (TMS, DBS, tES) [9,80,157,269].

CRediT authorship contribution statement

Francesca Castaldo: Writing – original draft, Visualization, Project administration, Methodology, Investigation, Conceptualization. **Raul de Palma Aristides:** Writing – original draft, Methodology, Investigation. **Pau Clusella:** Writing – original draft, Methodology, Investigation. **Jordi Garcia-Ojalvo:** Writing – original draft, Methodology, Investigation, Conceptualization. **Giulio Ruffini:** Writing – original draft, Validation, Supervision, Methodology, Investigation, Funding acquisition, Conceptualization.

Declaration of Generative AI and AI-assisted technologies in the writing process

During the preparation of this work the author(s) used ChatGPT in order to streamline the narrative. After using this tool/service, the author(s) reviewed and edited the content as needed and take(s) full responsibility for the content of the published article.

Declaration of competing interest

The author is an Editorial Board Member/Editor-in-Chief/Associate Editor/Guest Editor for this journal and was not involved in the editorial review or the decision to publish this article.

The authors declare the following financial interests/personal relationships which may be considered as potential competing interests: Giulio Ruffini and Francesca Castaldo work for Neuroelectrics, a company developing brain stimulation solutions. Giulio Ruffini is a co-founder of Neuroelectrics.

Acknowledgments

GR and FC have received funding from the European Research Council (ERC) under the European Union's Horizon 2020 research and innovation programme (grant agreement No 855109, GALVANI) and from FET under the European Union's Horizon 2020 research and innovation programme (grant agreement No 101017716, NEUROTWIN). PC has received financial support from the grant PID2024-155942NB-I00 funded by MCIN/AEI/10.13039/501100011033. Raul de Palma Aristides and Jordi Garcia-Ojalvo are supported by the European Commission under European Union's Horizon 2020 research and innovation programme Grant Number 101017716 (NEUROTWIN). Jordi Garcia-Ojalvo was also financially supported by the European Research Council (ERC) under the Synergy grant 101167121 (CeLEARN), by the Spanish Ministry of Science and Innovation and FEDER under project PID2024-160263NB-I00, and by the ICREA Academia program.

Appendix A. Supplementary data

Supplementary material related to this article can be found online at https://doi.org/10.1016/j.physrep.2026.05.004.

References

[1] Stephen Coombes, Peter Beim Graben, Roland Potthast, James Wright (Eds.), Neural Fields: Theory and Applications, Springer Berlin Heidelberg, Berlin, Heidelberg, 2014.
[2] Gustavo Deco, et al., The dynamic brain: from spiking neurons to neural masses and cortical fields, PLoS Comput. Biol. 4 (8) (2008).
[3] Bard Ermentrout, Neural networks as spatio-temporal pattern-forming systems, Rep. Progr. Phys. 61 (4) (1998) 353.
[4] Peter Ashwin, Stephen Coombes, Rachel Nicks, Mathematical frameworks for oscillatory network dynamics in neuroscience, J. Math. Neurosci. 6 (1) (2016) 2.
[5] Joana Cabral, Etienne Hugues, Olaf Sporns, Gustavo Deco, Role of local network oscillations in resting-state functional connectivity, NeuroImage 57 (1) (2011) 130–139.

[6] Olivier David, Karl J. Friston, A neural mass model for MEG/EEG: coupling and neuronal dynamics, NeuroImage 20 (3) (2003) 1743–1755.
[7] Francesca Castaldo, Francisco Páscoa Dos Santos, Ryan C Timms, Joana Cabral, Jakub Vohryzek, Gustavo Deco, Mark Woolrich, Karl Friston, Paul Verschure, Vladimir Litvak, Multi-modal and multi-model interrogation of large-scale functional brain networks, NeuroImage 277 (2023) 120236.
[8] Roser Sanchez-Todo, André M. Bastos, Edmundo Lopez-Sola, Borja Mercadal, Emiliano Santarnecchi, Earl K. Miller, Gustavo Deco, Giulio Ruffini, A physical neural mass model framework for the analysis of oscillatory generators from laminar electrophysiological recordings, NeuroImage 270 (2023) 119938.
[9] Michael Breakspear, Dynamic models of large-scale brain activity, Nature Neurosci. 20 (3) (2017) 340–352, Publisher: Nature Publishing Group.
[10] Ernest Montbrió, Diego Pazó, Alex Roxin, Macroscopic description for networks of spiking neurons, Phys. Rev. X 021028 (2015).
[11] Paul So, Tanushree B. Luke, Ernest Barreto, Networks of theta neurons with time-varying excitability: Macroscopic chaos, multistability, and final-state uncertainty, Phys. D: Nonlinear Phenom. 267 (2014) 16–26.
[12] Tanushree B. Luke, Ernest Barreto, Paul So, Complete classification of the macroscopic behavior of a heterogeneous network of theta neurons, Neural Comput. 25 (12) (2013) 3207–3234.
[13] Thomas Trappenberg, Fundamentals of Computational Neuroscience, third ed., Oxford University Press, Oxford New York, NY, 2023.
[14] Peter Dayan, L.F. Abbott, Theoretical Neuroscience: Computational and Mathematical Modeling of Neural Systems, MIT Press, 2001.
[15] Mathew P. Dafilis, Federico Frascoli, Peter J. Cadusch, David T.J. Liley, Four dimensional chaos and intermittency in a mesoscopic model of the electroencephalogram, Chaos 23 (2) (2013) 023111.
[16] P.A. Robinson, C.J. Rennie, J.J. Wright, H. Bahramali, E. Gordon, D.L. Rowe, Prediction of electroencephalographic spectra from neurophysiology, Phys. Rev. E 63 (2) (2001) 021903.
[17] C.J. Rennie, P.A. Robinson, J.J. Wright, Unified neurophysical model of EEG spectra and evoked potentials, Biol. Cybernet. 86 (6) (2002) 457–471.
[18] Kong-Fatt Wong, Xiao-Jing Wang, A recurrent network mechanism of time integration in perceptual decisions, J. Neurosci. 26 (4) (2006) 1314–1328.
[19] Gustavo Deco, Adrián Ponce-Alvarez, Dante Mantini, Gian Luca Romani, Patric Hagmann, Maurizio Corbetta, Resting-state functional connectivity emerges from structurally and dynamically shaped slow linear fluctuations, J. Neurosci. 33 (27) (2013) 11239–11252.
[20] Steven H. Strogatz, Nonlinear Dynamics and Chaos, Addison–Wesley, 1994.
[21] Bard Ermentrout, Nancy Kopell, Multiple traveling waves in neuronal networks, SIAM J. Appl. Math. 51 (1991) 179–194.
[22] Eugene M. Izhikevich, Dynamical Systems in Neuroscience: The Geometry of Excitability and Bursting, MIT Press, 2007.
[23] Arkady Pikovsky, Michael Rosenblum, Jürgen Kurths, Synchronization: A universal concept in nonlinear sciences, Camb. Nonlinear Sci. Ser. 12 (2003).
[24] Daniel M. Abrams, Steven H. Strogatz, Chimera states for coupled oscillators, Phys. Rev. Lett. 93 (2004) 174102.
[25] Steven H. Strogatz, Nonlinear dynamics and chaos with student solutions manual, 2018, (No Title).
[26] Frank C. Hoppensteadt, Eugene M. Izhikevich, Weakly Connected Neural Networks, vol. 126, Springer Science & Business Media, 2012.
[27] Yuri A. Kuznetsov, Elements of applied bifurcation theory, fourth ed., in: Applied Mathematical Sciences, Springer Cham, 2023, p. XXVI, 703.
[28] D.T.J. Liley, P.J. Cadusch, J.J. Wright, A continuum theory of electro-cortical activity, Neurocomputing 26–27 (1999) 795–800.
[29] D.T.J. Liley, P.J. Cadusch, M.P. Dafilis, A spatially continuous mean field theory of electrocortical activity, Netw., Comput. Neural Syst. 13 (1) (2002) 67–113.
[30] Adrián Ponce-Alvarez, Gustavo Deco, The Hopf whole-brain model and its linear approximation, Sci. Rep. 14 (2024) 2615.
[31] Matthieu Gilson, Gustavo Deco, Katsumi Friston, Patric Hagmann, Dante Mantini, Michael L.L.M. van Mieghem, D.J.O. de Pasquale, Viktor Jirsa, Andrea J.R. Messé, H.R.W.R. Senden, Estimation of directed effective connectivity from fMRI functional connectivity hints at asymmetries of cortical connectome, PLoS Comput. Biol. 12 (1) (2016) e1004762.
[32] Selen Atasoy, Leor Roseman, Mendel Kaelen, Morten L. Kringelbach, Gustavo Deco, Robin L. Carhart-Harris, Connectome-harmonic decomposition of human brain activity reveals dynamical repertoire re-organization under LSD, Sci. Rep. 7 (2017) 17661.
[33] Steven H. Strogatz, Nonlinear Dynamics and Chaos: With Applications to Physics, Biology, Chemistry, and Engineering, second ed., Westview Press, Boulder, CO, 2018.
[34] Arthur T. Winfree, The Geometry of Biological Time, second ed., Springer, New York, NY, 2001.
[35] Giulio Ruffini, Fabrice Wendling, Isabelle Merlet, Behnam Molaee-Ardekani, Abeye Mekonnen, Ricardo Salvador, Aureli Soria-Frisch, Carles Grau, Stephen Dunne, Pedro C. Miranda, Transcranial Current Brain Stimulation (tCS): Models and Technologies, IEEE Trans. Neural Syst. Rehabil. Eng. 21 (3) (2013) 333–345, Conference Name: IEEE Transactions on Neural Systems and Rehabilitation Engineering.
[36] Giulio Ruffini, Michael D Fox, Oscar Ripolles, Pedro Cavaleiro Miranda, Alvaro Pascual-Leone, Optimization of multifocal transcranial current stimulation for weighted cortical pattern targeting from realistic modeling of electric fields, Neuroimage 89 (2014) 216–225.
[37] Adrià Galan-Gadea, Ricardo Salvador, Fabrice Bartolomei, Fabrice Wendling, Giulio Ruffini, Spherical harmonics representation of the steady-state membrane potential shift induced by tDCS in realistic neuron models, J. Neural Eng. 20 (2) (2023).
[38] Aman S. Aberra, Angel V. Peterchev, Warren M. Grill, Biophysically realistic neuron models for simulation of cortical stimulation, J. Neural Eng. 15 (6) (2018) 066023.
[39] Aman S. Aberra, Boshuo Wang, Warren M. Grill, Angel V. Peterchev, Simulation of transcranial magnetic stimulation in head model with morphologically-realistic cortical neurons, Brain Stimul. 13 (1) (2020) 175–189.
[40] David C. Roberts, Linear reformulation of the kuramoto model of self-synchronizing oscillators, Phys. Rev. E 77 (3) (2008) 031114.
[41] Laurie Conteville, Elena Panteley, Linear reformulation of the kuramoto model: Asymptotic mapping and stability properties, in: Proceedings of the 2013 European Control Conference, ECC, 2013, pp. 821–826.
[42] Yoshiki Kuramoto, Chemical oscillations, waves, and turbulence, in: Springer Series in Synergetics, vol. 19, Springer, Berlin, Heidelberg, 1984.
[43] Hiroya Nakao, Phase reduction approach to synchronization of nonlinear oscillators, Contemp. Phys. 57 (2) (2016) 188–214.
[44] Bastian Pietras, Federico Devalle, Alex Roxin, Andreas Daffertshofer, Ernest Montbrió, Exact firing rate model reveals the differential effects of chemical versus electrical synapses in spiking networks, Phys. Rev. E 100 (2019) 042412.
[45] Yoshiki Kuramoto, Self-entrainment of a population of coupled non-linear oscillators, in: Huzihiro Araki (Ed.), International Symposium on Mathematical Problems in Theoretical Physics, Springer, Berlin, Heidelberg, 1975, pp. 420–422.
[46] Steven H. Strogatz, Nonlinear Dynamics and Chaos: with Applications to Physics, Biology, Chemistry, and Engineering, Westview Press, a member of the Perseus Books Group, Boulder, CO, 2015.
[47] Juan A. Acebrón, L.L. Bonilla, Conrad J. Pérez Vicente, Félix Ritort, Renato Spigler, The Kuramoto model: A simple paradigm for synchronization phenomena, Rev. Modern Phys. 77 (1) (2005) 137–185.
[48] G. Bard Ermentrout, David H. Terman, Mathematical Foundations of Neuroscience, Springer, New York, NY, 2010.
[49] Steven H. Strogatz, From Kuramoto to Crawford: Exploring the onset of synchronization in populations of coupled oscillators, Phys. D: Nonlinear Phenom. 143 (1) (2000) 1–20.
[50] Arthur T. Winfree, Biological rhythms and the behavior of populations of coupled oscillators, J. Theoret. Biol. 16 (1) (1967) 15–42.
[51] Yoshiki Kuramoto, Lecture notes in physics, international symposium on mathematical problems in theoretical physics, in: Lecture Notes in Physics, in: Lecture Notes in Physics, vol. 30, 1975.

[52] Steven H. Strogatz, From kuramoto to crawford: Exploring the onset of synchronization in populations of coupled oscillators, Phys. D: Nonlinear Phenom. 143 (1–4) (2000) 1–20.
[53] J.A. Acebrón, L.L. Bonilla, C.J. Pérez Vicente, F. Ritort, R. Spigler, The kuramoto model: A simple paradigm for synchronization phenomena, Rev. Modern Phys. 77 (1) (2005) 137–185.
[54] Michael Breakspear, Stewart Heitmann, Andreas Daffertshofer, Generative models of cortical oscillations: neurobiological implications of the kuramoto model, Front. Hum. Neurosci. 4 (2010) 190.
[55] Joana Cabral, Henry Luckhoo, Mark Woolrich, Morten Joensson, Hamid Mohseni, Adam Baker, Morten L. Kringelbach, Gustavo Deco, Exploring mechanisms of spontaneous functional connectivity in MEG: How delayed network interactions lead to structured amplitude envelopes of band-pass filtered oscillations, NeuroImage 90 (2014) 423–435.
[56] J. Cabral, E. Hugues, M.L. Kringelbach, G. Deco, Role of local network oscillations in resting-state functional connectivity, NeuroImage 57 (2014) 130–139.
[57] György Buzsáki, Rhythms of the Brain, Oxford University Press, Oxford, UK, 2006.
[58] Joana Cabral, Emmanuel Hugues, Olaf Sporns, Gustavo Deco, Role of local network oscillations in resting-state functional connectivity, NeuroImage 57 (1) (2011) 130–139.
[59] Ruben Schmidt, Karl J.R. LaFleur, Marcel A. de Reus, Leonard H. van den Berg, Martijn P. van den Heuvel, Kuramoto model simulation of neural hubs and dynamic synchrony in the human cerebral connectome, BMC Neurosci. 16 (2015) 54.
[60] Murray Shanahan, Metastable chimera states in community-structured oscillator networks, Chaos 20 (1) (2010) 013108.
[61] Johanne Hizanidis, Nikos E. Kouvaris, Gorka Zamora-López, Albert Díaz-Guilera, Chris G. Antonopoulos, Chimera-like states in modular neural networks, Sci. Rep. 6 (2016) 19845.
[62] Joana Cabral, Morten L. Kringelbach, Gustavo Deco, Exploring the network dynamics underlying brain activity during rest, Prog. Neurobiol. 114 (2014) 102–131.
[63] Changgui Gu, Zonghua Liu, William J. Schwartz, Premananda Indic, Photic desynchronization of two subgroups of circadian oscillators in a network model of the suprachiasmatic nucleus with dispersed coupling strengths, PLoS ONE 7 (5) (2012) e36900.
[64] Spase Petkoski, Andreas Spiegler, Timothée Proix, Parham Aram, Jean-Jacques Temprado, Viktor K. Jirsa, Heterogeneity of time delays determines synchronization of coupled oscillators, Phys. Rev. E 94 (1) (2016) 012209.
[65] Spase Petkoski, J. Matias Palva, Viktor K. Jirsa, Phase-lags in large-scale brain synchronization: Methodological considerations and in-silico analysis, PLoS Comput. Biol. 14 (7) (2018) e1006160.
[66] Spase Petkoski, Andreas Spiegler, Timothée Proix, Parham Aram, Jean-Jacques Temprado, Viktor K. Jirsa, Transmission time delays organize the brain network synchronization, Phil. Trans. R. Soc. A 377 (2153) (2019) 20180132.
[67] P. Fries, Rhythms for Cognition: Communication through Coherence, Neuron 88 (1) (2015) 220–235.
[68] Peter A. Tass, Desynchronization by means of a coordinated reset of neural sub-populations, Progr. Theoret. Phys. Suppl. 150 (2003) 281–296.
[69] Oleksandr V. Popovych, Serhiy Yanchuk, Peter A. Tass, Multisite delayed feedback for electrical brain stimulation, Front. Neurosci. 12 (2018) 644.
[70] Gihan Weerasinghe, Hayriye Cagnan, Peter Brown, Rafal Bogacz, Predicting the effects of deep brain stimulation using a reduced coupled oscillator model, PLoS Comput. Biol. 15 (7) (2019) e1006575.
[71] Gihan Weerasinghe, Hayriye Cagnan, Peter Brown, Rafal Bogacz, Optimal closed-loop deep brain stimulation using multiple independently controlled contacts, PLoS Comput. Biol. 17 (8) (2021) e1009281.
[72] Maximilian Sadilek, Stefan Thurner, Physiologically motivated multiplex kuramoto model describes phase diagram of cortical activity, Sci. Rep. 5 (2015) 10015.
[73] Lukas G. Bauer, Fabian Hirsch, Craig Jones, Michael Hollander, Philipp Grohs, Amit Anand, Chris Plant, Andreas Wohlschläger, Quantification of kuramoto coupling between intrinsic brain networks applied to fMRI data in major depressive disorder, Front. Comput. Neurosci. 16 (2022) 729556.
[74] H. Sakaguchi, Y. Kuramoto, A soluble active rotator model showing phase transitions via mutual entrainment, Progr. Theoret. Phys. 76 (3) (1986) 576–581.
[75] Adrián Ponce-Alvarez, Gustavo Deco, The Hopf whole-brain model and its linear approximation, Sci. Rep. 14 (2024) 2615.
[76] Marco Aqil, Selen Atasoy, Morten L. Kringelbach, Rikkert Hindriks, Graph neural fields: A framework for spatiotemporal dynamical models on the human connectome, PLoS Comput. Biol. 17 (1) (2021) e1008310.
[77] Ashish Raj, Chang Cai, Xihe Xie, Eva Palacios, Julia Owen, Pratik Mukherjee, Srikantan S. Nagarajan, Spectral graph theory of brain oscillations, Hum. Brain Mapp. 41 (11) (2020) 2980–2998.
[78] Parul Verma, Srikantan S. Nagarajan, Ashish Raj, Spectral graph theory of brain oscillations—Revisited and improved, NeuroImage 249 (2022) 118919.
[79] Erfan Nozari, Maxwell A. Bertolero, Jennifer Stiso, Lorenzo Caciagli, Eli J. Cornblath, Xiaosong He, Arun S. Mahadevan, George J. Pappas, Dani S. Bassett, Macroscopic resting-state brain dynamics are best described by linear models, Nat. Biomed. Eng. 8 (2024) 68–84.
[80] Benoit Duchet, Rafal Bogacz, How to design optimal brain stimulation to modulate phase-amplitude coupling? J. Neural Eng. 21 (4) (2024) 10.1088/1741–2552/ad5b1a.
[81] Felix Effenberger, Pedro Carvalho, Igor Dubinin, Wolf Singer, The functional role of oscillatory dynamics in neocortical circuits: A computational perspective, Proc. Natl. Acad. Sci. 122 (4) (2025) e2412830122, Publisher: Proceedings of the National Academy of Sciences.
[82] Gustavo Deco, Christopher W. Lynn, Yonatan Sanz Perl, Morten L. Kringelbach, Violations of the fluctuation–dissipation theorem reveal distinct nonequilibrium dynamics of brain states, Phys. Rev. E 108 (6) (2023) 064410.
[83] Joana Cabral, Gustavo Deco, Morten L. Kringelbach, Remote synchronization in the human cortex, Sci. Rep. 14 (1) (2024) 5678.
[84] Gustavo Deco, Juan Cruzat, Joana Cabral, Enzo Tagliazucchi, Helmut Laufs, Nikos K. Logothetis, Morten L. Kringelbach, Modeling the impact of LSD on whole-brain dynamics using the Hopf model, NeuroImage 218 (2020) 116871.
[85] Gustavo Deco, Morten L. Kringelbach, Turbulent-like dynamics in the human brain, Cell Rep. 33 (10) (2020) 108471, Publisher: Elsevier BV.
[86] Adrián Ponce-Alvarez, Gustavo Deco, The Hopf whole-brain model and its linear approximation, Sci. Rep. 14 (1) (2024) 2615, Publisher: Nature Publishing Group.
[87] Jurij A. Kuznecov, Elements of applied bifurcation theory, in: Applied mathematical sciences, (112) Springer, New York Berlin Heidelberg, 1995.
[88] Ana P. Millán, David Poyato, David N. Reynolds, Francesco Tudisco, Synchronization of coupled Stuart-Landau oscillators: How heterogeneity can facilitate synchronization, 2025.
[89] Roberto C. Budzinski, Tung T. Nguyen, Gabriel B. Benigno, Jacqueline Doàn, Ján Mináč, Terrence J. Sejnowski, Lyle E. Muller, Analytical prediction of specific spatiotemporal patterns in nonlinear oscillator networks with distance-dependent time delays, Phys. Rev. Res. 5 (1) (2023) 013159.
[90] L.D. Landau, On the problem of turbulence, Dokl. Akad. Nauk SSSR 44 (8) (1944) 339–349.
[91] J.T. Stuart, On the non-linear mechanics of hydrodynamic stability, J. Fluid Mech. 4 (1) (1958) 1–21.
[92] J.T. Stuart, On the non-linear mechanics of wave disturbances in stable and unstable parallel flows. Part 1. The basic behaviour in plane poiseuille flow, J. Fluid Mech. 9 (3) (1960) 353–370.

[93] Gustavo Deco, Morten L. Kringelbach, Viktor K. Jirsa, Petra Ritter, The dynamics of resting fluctuations in the brain: metastability and its dynamical cortical core, Sci. Rep. 7 (1) (2017) 3095.
[94] Joana Cabral, Francesca Castaldo, Jakub Vohryzek, Vladimir Litvak, Christian Bick, Renaud Lambiotte, Karl Friston, Morten L. Kringelbach, Gustavo Deco, Metastable oscillatory modes emerge from synchronization in the brain spacetime connectome, Commun. Phys. 5 (2022) 184.
[95] Gustavo Deco, Joana Cabral, Mark W. Woolrich, Angus B.A. Stevner, Tim J. van Hartevelt, Morten L. Kringelbach, Single or multiple frequency generators in on-going brain activity: A mechanistic whole-brain model of empirical MEG data, NeuroImage 152 (2017) 538–550.
[96] Felix Siebenhühner, Francesca Castaldo, Joana Cabral, J. Matias Palva, Gustavo Deco, Satu Palva, Spectral patterns of MEG oscillatory coupling emerge from meta-stable dynamics with small coupling delays, BioRxiv (2025) preprint.
[97] Yonatan Sanz Perl, Anira Escrichs, Enzo Tagliazucchi, Morten L. Kringelbach, Gustavo Deco, Strength-dependent perturbation of whole-brain model working in different regimes reveals the role of fluctuations in brain dynamics, PLoS Comput. Biol. 18 (11) (2022) e1010662.
[98] Frank Freyer, James A. Roberts, Petra Ritter, Michael Breakspear, A canonical model of multistability and scale-invariance in biological systems, PLoS Comput. Biol. 8 (8) (2012) e1002634.
[99] Anira Escrichs, Yonatan Sanz Perl, Camila Uribe, et al., Unifying turbulent dynamics framework distinguishes different brain states, Commun. Biology 5 (2022) 638.
[100] Beatrice M. Jobst, Selen Atasoy, Adrián Ponce-Alvarez, Ana Sanjuán, Leor Roseman, Mendel Kaelen, Robin Carhart-Harris, Morten L. Kringelbach, Gustavo Deco, Increased sensitivity to strong perturbations in a whole-brain model of LSD, NeuroImage 230 (2021) 117809.
[101] Josephine Cruzat, Yonatan Sanz Perl, Anira Escrichs, Jakub Vohryzek, Christopher Timmermann, Leor Roseman, Andrea I. Luppi, Agustin Ibañez, David Nutt, Robin Carhart-Harris, Enzo Tagliazucchi, Gustavo Deco, Morten L. Kringelbach, Effects of classic psychedelic drugs on turbulent signatures in brain dynamics, Netw. Neurosci. (Cambridge, Mass.) 6 (4) (2022) 1104–1124.
[102] Giulio Ruffini, Edmundo Lopez-Sola, Jakub Vohryzek, Roser Sanchez-Todo, Neural geometrodynamics, complexity, and plasticity: a psychedelics perspective, Entropy 26 (1) (2024) 90, Publisher: MDPI.
[103] Jakub Vohryzek, Joana Cabral, Francesca Castaldo, Yonatan Sanz-Perl, Louis-David Lord, Henrique M Fernandes, Vladimir Litvak, Morten L Kringelbach, Gustavo Deco, Dynamic sensitivity analysis: Defining personalised strategies to drive brain state transitions via whole brain modelling, Comput. Struct. Biotechnol. J. 21 (2023) 335–345, Publisher: Elsevier.
[104] D. Hillis, H.C. Heller, S.D. Hacker, D. Hall, D. Sadava, M. Laskowski, Life: The Science of Biology, Macmillan Learning, 2020.
[105] Daniel A. Goodenough, David L. Paul, Gap Junctions, Cold Spring Harb. Perspect. Biology 1 (1) (2009) a002576.
[106] Alberto E. Pereda, Electrical synapses and their functional interactions with chemical synapses, Nature Rev. Neurosci. 15 (4) (2014) 250–263.
[107] Pepe Alcamí, Alberto E. Pereda, Beyond plasticity: The dynamic impact of electrical synapses on neural circuits, Nature Rev. Neurosci. 20 (5) (2019) 253–271.
[108] Mitchell J. Vaughn, Julie S. Haas, On the diverse functions of electrical synapses, Front. Cell. Neurosci. 16 (2022).
[109] Alain Destexhe, Zachary F. Mainen, Terrence J. Sejnowski, Synthesis of models for excitable membranes, synaptic transmission and neuromodulation using a common kinetic formalism, J. Comput. Neurosci. 1 (3) (1994) 195–230.
[110] A. Destexhe, Z.F. Mainen, T.J. Sejnowski, Kinetic models of synaptic transmission, in: Methods in Neuronal Modeling: from Ions To Networks, second ed., MIT Press, Cambridge, MA, 1998, pp. 1–25.
[111] Peter Dayan, L.F. Abbott, Theoretical neuroscience: Computational and mathematical modeling of neural systems, in: Computational Neuroscience, Massachusetts Institute of Technology Press, Cambridge, Mass, 2001.
[112] Wulfram Gerstner, Werner M. Kistler, Richard Naud, Liam Paninski, Neuronal Dynamics: From Single Neurons to Networks and Models of Cognition, First, Cambridge University Press, 2014.
[113] W. Rall, R.E. Burke, T.G. Smith, P.G. Nelson, K. Frank, Dendritic location of synapses and possible mechanisms for the monosynaptic EPSP in motoneurons, J. Neurophysiol. 30 (5) (1967) 1169–1193.
[114] R.E. Burke, Composite nature of the monosynaptic excitatory postsynaptic potential, J. Neurophysiol. 30 (5) (1967) 1114–1137.
[115] P.G. Nelson, K. Frank, Anomalous rectification in cat spinal motoneurons and effect of polarizing currents on excitatory postsynaptic potential, J. Neurophysiol. 30 (5) (1967) 1097–1113.
[116] W. Rall, Distinguishing theoretical synaptic potentials computed for different soma-dendritic distributions of synaptic input, J. Neurophysiol. 30 (5) (1967) 1138–1168.
[117] Ben H. Jansen, Vincent G. Rit, Electroencephalogram and visual evoked potential generation in a mathematical model of coupled cortical columns, Biol. Cybernet. 73 (4) (1995) 357–366.
[118] F. Wendling, F. Bartolomei, J.J. Bellanger, P. Chauvel, Epileptic fast activity can be explained by a model of impaired GABAergic dendritic inhibition, Eur. J. Neurosci. 15 (9) (2002) 1499–1508.
[119] Giulio Ruffini, Roser Sánchez-Todo, Laura Dubreuil, Ricardo Salvador, Dimitris Pinotsis, Earl K. Miller, André M. Bastos, P118: A biophysically realistic laminar neural mass modeling framework for transcranial current stimulation, Clin. Neurophysiol. 131 (2020) e78.
[120] Roser Sánchez-Todo, André M. Bastos, Edmundo Lopez-Sola, Borja Mercadal, Emiliano Santarnecchi, Earl K. Miller, Gustavo Deco, Giulio Ruffini, A physical neural mass model framework for the analysis of oscillatory generators from laminar electrophysiological recordings, NeuroImage 270 (2023) 119938.
[121] G. Bard Ermentrout, David H. Terman, Mathematical Foundations of Neuroscience, in: Interdisciplinary Applied Mathematics, vol. 35, Springer, New York, NY, 2010.
[122] Hugh R. Wilson, Jack D. Cowan, Excitatory and inhibitory interactions in localized populations of model neurons, Biophys. J. 12 (1) (1972) 1–24.
[123] Arnold J.F. Siegert, On the first passage time probability problem, Phys. Rev. 81 (1951) 617–623.
[124] D. Amit, Model of global spontaneous activity and local structured activity during delay periods in the cerebral cortex, Cerebral Cortex 7 (3) (1997) 237–252.
[125] Nicolas Brunel, Vincent Hakim, Fast global oscillations in networks of integrate-and-fire neurons with low firing rates, Neural Comput. 11 (7) (1999) 1621–1671.
[126] Nicolas Fourcaud-Trocmé, David Hansel, Carl van Vreeswijk, Nicolas Brunel, How spike generation mechanisms determine the neuronal response to fluctuating inputs, J. Neurosci. 23 (37) (2003) 11628–11640.
[127] Nicolas Fourcaud-Trocmé, Nicolas Brunel, Dynamics of the instantaneous firing rate in response to changes in input statistics, J. Comput. Neurosci. 18 (3) (2005) 311–321.
[128] Nicolas Brunel, Peter E. Latham, Firing rate of the noisy quadratic integrate-and-fire neuron, Neural Comput. 15 (10) (2003) 2281–2306.
[129] Ernest Montbrió, Diego Pazó, Alex Roxin, Macroscopic description for networks of spiking neurons, Phys. Rev. X 5 (2) (2015) 021028.
[130] Pau Clusella, Ernest Montbrió, Regular and sparse neuronal synchronization are described by identical mean field dynamics, 2022.
[131] Walter J. Freeman, Mass Action in the Nervous System, Elsevier, 1975.
[132] Walter J. Freeman, Nonlinear gain mediating cortical stimulus-response relations, Biol. Cybernet. 33 (4) (1979) 237–247.
[133] T.P. Vogels, H. Sprekeler, F. Zenke, C. Clopath, W. Gerstner, Inhibitory plasticity balances excitation and inhibition in sensory pathways and memory networks, Science 334 (6062) (2011) 1569–1573.

[134] Hugh R. Wilson, Jack D. Cowan, Excitatory and Inhibitory interactions in localized populations of model neurons, Biophys. J. 12 (1) (1972) 1–24.
[135] Michael Breakspear, Dynamic models of large-scale brain activity, Nature Neurosci. 20 (3) (2017) 340–352.
[136] Lea Fredrickson-Hemsing, Seung Ji, Robijn Bruinsma, Dolores Bozovic, Mode-locking dynamics of hair cells of the inner ear, Phys. Rev. E 86 (2) (2012) 021915, Publisher: American Physical Society.
[137] John Guckenheimer, Philip Holmes, Nonlinear oscillations, dynamical systems, and bifurcations of vector fields, Corrected seventh printing, in: Applied mathematical sciences, (42) Springer Science+Business Media, New York, NY, 2002.
[138] G. Ermentrout, David H. Bard, Mathematical Foundations of Neuroscience, Springer-Verlag New York, 2010.
[139] Bastian Pietras, Andreas Daffertshofer, Network dynamics of coupled oscillators and phase reduction techniques, Phys. Rep. 819 (2019) 1–105.
[140] Roman M. Borisyuk, Alexandr B. Kirillov, Bifurcation analysis of a neural network model, Biol. Cybernet. 66 (4) (1992) 319–325.
[141] Frank C. Hoppensteadt, Eugene M. Izhikevich, Weakly connected neural networks, in: Applied Mathematical Sciences, vol. 126, Springer, New York, 1997.
[142] Andreas Daffertshofer, Bernadette C.M. van Wijk, On the influence of amplitude on the connectivity between phases, Front. Neuroinformatics 5 (2011) 6.
[143] Stephen Coombes, Áine Byrne, Next generation neural mass models, 2019, pp. 1–16.
[144] Jaroslav Hlinka, Stephen Coombes, Using computational models to relate structural and functional brain connectivity, Eur. J. Neurosci. 36 (6) (2012) 2137–2145.
[145] Hugh R. Wilson, Jack D. Cowan, Excitatory and inhibitory interactions in localized populations of model neurons, Biophys. J. 12 (1) (1972) 1–24.
[146] Hugh R. Wilson, Jack D. Cowan, A mathematical theory of the functional dynamics of nervous tissue, Kybernetik 13 (1973) 55–80.
[147] Alain Destexhe, Terrence J. Sejnowski, The Wilson–Cowan model, 36 years later, Biol. Cybernet. 101 (1) (2009) 1–2.
[148] Jack D. Cowan, Jeremy Neuman, Wim van Drongelen, Wilson–Cowan equations for neocortical dynamics, J. Math. Neurosci. 6 (1) (2016) 1.
[149] Carson C. Chow, Yasaman Karimipanah, Before and beyond the Wilson–Cowan equations, J. Math. Neurosci. 10 (1) (2020) 61.
[150] Romesh G. Abeysuriya, Jonathan Hadida, Stamatios N. Sotiropoulos, Saad Jbabdi, Robert Becker, Benjamin A.E. Hunt, Matthew J. Brookes, Mark W. Woolrich, A biophysical model of dynamic balancing of excitation and inhibition in fast oscillatory large-scale networks, PLoS Comput. Biol. 14 (2) (2018) e1006007.
[151] S.L. Keeley, et al., Firing rate models for brain rhythms, J. Neurophysiol. 122 (4) (2019) 1561–1588.
[152] Guoshi Li, Yujie Liu, Yanting Zheng, Ye Wu, Danian Li, Xinyu Liang, Yaoping Chen, Ying Cui, Pew-Thian Yap, Shijun Qiu, Han Zhang, Dinggang Shen, Multiscale neural modeling of resting-state fMRI reveals executive–limbic malfunction as a core mechanism in major depressive disorder, NeuroImage: Clin. 31 (2021) 102758.
[153] Paula Sanz Leon, Stuart A. Knock, Andreas Spiegler, Viktor K. Jirsa, The virtual brain: a simulator of primate brain network dynamics, Front. Neuroinformatics 7 (2013) 10.
[154] Paula Sanz-León, Stuart A. Knock, Andreas Spiegler, Viktor K. Jirsa, Mathematical framework for large-scale brain network modeling in *The Virtual Brain*, NeuroImage 111 (2015) 385–430.
[155] Thomas F. Varley, Prejaas Tewarie, et al., Non-reversibility as a quantitative marker of neurophysiological change from MEG, NeuroImage 273 (2023) 120002, Uses WC local dynamics as a generative benchmark.
[156] Rustam Masharipov, Dongha Shin, Qisheng Zhao, Quinn K. Telesford, Paula Sanz-Leon, et al., Task-modulated functional connectivity: a comprehensive evaluation of state-of-the-art methods, Commun. Biol. 7 (1) (2024) ???, Includes WC generative simulations.
[157] Sadjad Sadeghi, Daniela Mier, Martin F. Gerchen, Susanne N.L. Schmidt, Joachim Hass, Dynamic causal modeling for fMRI with Wilson–Cowan–based neuronal equations, Front. Neurosci. 14 (2020) 593867.
[158] Hil G.E. Meijer, Tahra L. Eissa, Bert Kiewiet, Jeremy F. Neuman, Catherine A. Schevon, Robert G. Emerson, Robert R. Goodman, Guy M. McKhann, Charles J. Marcuccilli, Andrew K. Tryba, Jack D. Cowan, Stephan A. van Gils, Wim van Drongelen, Modeling focal epileptic activity in the Wilson–Cowan model with depolarization block, J. Math. Neurosci. 5 (1) (2015) 7.
[159] Laura M. Sánchez-Rodríguez, Miriam Vila-Vidal, Perrine Berroir, Arnau Méndez, Gustavo Deco, Morten L. Kringelbach, Joana Cabral, Bridging scales in Alzheimer's disease by whole-brain modelling: from the braak staging scheme to functional connectivity, Commun. Biol. 7 (1) (2024) ???.
[160] Antonio de Candia, Alessandro Sarracino, Ilenia Apicella, Lucilla de Arcangelis, Critical behaviour of the stochastic Wilson–Cowan model, PLoS Comput. Biol. 17 (8) (2021) e1008884.
[161] Ilenia Apicella, Antonio de Candia, Daniele Conte, Lucilla de Arcangelis, Alessandro Sarracino, Power spectrum and critical exponents in the 2D stochastic Wilson–Cowan model, Sci. Rep. 12 (1) (2022) 22612.
[162] Hamed Alvankar Golpayegan, Andrea Cavagna, Serena di Santo, Édgar Roldán, Massimiliano Viale, Alessio Attanasi, Massimiliano Viale, Bistability and criticality in the stochastic Wilson–Cowan model, Phys. Rev. E 107 (3) (2023) 034404.
[163] J.W.M. Domhof, S.B. Eickhoff, O.V. Popovych, Reliability and subject specificity of personalized whole-brain dynamical models, NeuroImage 257 (2022) 119321.
[164] Giulio Ruffini, Michael D. Fox, Oscar Ripolles, Pedro Cavaleiro Miranda, Alvaro Pascual-Leone, Optimization of multifocal transcranial current stimulation for weighted cortical pattern targeting from realistic modeling of electric fields, NeuroImage 89 (2014) 216–225.
[165] Borja Mercadal, Maria Guasch-Morgades, Lucia Mencarelli, Giacomo Koch, Giulio Ruffini, Bridging local and global dynamics: a biologically grounded model for cooperative and competitive interactions in the brain, BioRxiv (2025) 1–33, Publisher: Cold Spring Harbor Laboratory.
[166] Michael Forrester, Jonathan J. Crofts, Stamatios N. Sotiropoulos, Stephen Coombes, Reuben D. O'Dea, The role of node dynamics in shaping emergent functional connectivity patterns in the brain, Netw. Neurosci. 4 (2) (2020) 467–483.
[167] B.H. Jansen, G. Zouridakis, M.E. Brandt, A neurophysiologically-based mathematical model of flash visual evoked potentials, Biol. Cybernet. 68 (3) (1993) 275–283.
[168] F. Grimbert, Olivier Faugeras, Analysis of Jansen's model of a single cortical column, INRIA RR-5597 (2006) 34.
[169] Fabrice Wendling, Pascal Benquet, Fabrice Bartolomei, Viktor Jirsa, Computational models of epileptiform activity, J. Neurosci. Methods 260 (2016) 233–251.
[170] G. Ruffini, R. Sanchez-Todo, L. Dubreuil, R. Salvador, D. Pinotsis, E.K. Miller, F. Wendling, E. Santarnecchi, A. Bastos, P118 a Biophysically realistic Laminar Neural Mass Modeling framework for transcranial Current Stimulation, Clin. Neurophysiol. 131 (4) (2020) e78–e79.
[171] Behnam Molaee-Ardekani, Pascal Benquet, Fabrice Bartolomei, Fabrice Wendling, Computational modeling of high-frequency oscillations at the onset of neocortical partial seizures: from 'altered structure' to 'dysfunction'., Neuroimage 52 (3) (2010) 1109–1122.
[172] György Buzsáki, Xiao-Jing Wang, Mechanisms of Gamma oscillations, Annu. Rev. Neurosci. 35 (2012) 203–225.
[173] Paul Tiesinga, Terrence J. Sejnowski, Cortical enlightenment: are attentional gamma oscillations driven by ING or PING? Neuron 63 (6) (2009) 727–732.
[174] Christoph Börgers, Nancy Kopell, Synchronization in networks of excitatory and inhibitory neurons with sparse, random connectivity, Neural Comput. 15 (3) (2003) 509–538.

[175] Miles A. Whittington, Roger D. Traub, Nancy Kopell, Bard Ermentrout, E.H. Buhl, Inhibition-based rhythms: experimental and mathematical observations on network dynamics, Int. J. Psychophysiol. 38 (3) (2000) 315–336.
[176] F. Grimbert, O. Faugeras, Bifurcation analysis of Jansen's neural mass model, Neural Comput. 18 (12) (2006) 3052–3068.
[177] A. Spiegler, T.R. Knösche, K. Schwab, J. Haueisen, V.K. & Jirsa, Dynamic causal modelling revisited: A computational modelling approach for EEG/MEG, Philos. Trans. R. Soc. B 365 (2010) 2479–2492.
[178] Rosalyn J. Moran, Klaas E. Stephan, Thomas Seidenbecher, Hans-Christian Pape, Raymond J. Dolan, Karl J. Friston, Dynamic causal models of steady-state responses, NeuroImage 44 (3) (2009) 796–811.
[179] Rosalyn J. Moran, Dimitris A. Pinotsis, Karl J. Friston, Neural masses and fields in dynamic causal modeling, Front. Comput. Neurosci. 7 (2013) 57.
[180] Fabrice Wendling, Fabrice Bartolomei, Jean-Jacques Bellanger, Patrick Chauvel, Epileptic fast activity can be explained by a model of impaired GABAergic dendritic inhibition in the hippocampus, Eur. J. Neurosci. 15 (9) (2002) 1499–1508.
[181] Fabrice Wendling, Pascal Benquet, Fabrice Bartolomei, Viktor Jirsa, Computational models of epileptiform activity, J. Neurosci. Methods 260 (2016) 233–251.
[182] Edmundo Lopez-Sola, Roser Sanchez-Todo, Èlia Lleal, Elif Köksal-Ersöz, Maxime Yochum, Julia Makhalova, Borja Mercadal, Maria Guasch-Morgades, Ricardo Salvador, Diego Lozano-Soldevilla, Julien Modolo, Fabrice Bartolomei, Fabrice Wendling, Pascal Benquet, Giulio Ruffini, A personalizable autonomous neural mass model of epileptic seizures, J. Neural Eng. 19 (5) (2022).
[183] Dong Cui, Han Li, Hongyuan Shao, Guanghua Gu, Xiaonan Guo, Xiaoli Li, Construction and analysis of a new resting-state whole-brain network model, Brain Sci. 14 (3) (2024) 240, Wendling nodes on human connectome.
[184] Elif Köksal-Ersöz, Julia Makhalova, Maxime Yochum, Christian-G. Bénar, Maxime Guye, Fabrice Bartolomei, Fabrice Wendling, Isabelle Merlet, Whole-brain simulation of interictal epileptic discharges for patient-specific interpretation of interictal SEEG data, Neurophysiol. Clin. / Clin. Neurophysiol. 54 (5) (2024) 103005.
[185] Edmundo López-Solà, Borja Mercadal, Èlia Lleal-Custey, Ricardo Salvador, Roser Sanchez-Todo, Fabrice Wendling, Fabrice Bartolomei, Giulio Ruffini, Personalized whole-brain models of seizure propagation, J. Neural Eng. 22 (5) (2025) 056019.
[186] Raul de Palma Aristides, Pau Clusella, Roser Sanchez-Todo, Giulio Ruffini, Jordi Garcia-Ojalvo, Emergence of multifrequency activity in a laminar neural mass model, PLoS Comput. Biol. 22 (4) (2026) e1014022.
[187] Diego Mendoza-Halliday, Alex James Major, Noah Lee, Maxwell J. Lichtenfeld, Brock Carlson, Blake Mitchell, Patrick D. Meng, Yihan (Sophy) Xiong, Jacob A. Westerberg, Xiaoxuan Jia, Kevin D. Johnston, Janahan Selvanayagam, Stefan Everling, Alexander Maier, Robert Desimone, Earl K. Miller, André M. Bastos, A ubiquitous spectrolaminar motif of local field potential power across the primate cortex, Nature Neurosci. (2024) 1–14, Publisher: Nature Publishing Group.
[188] Elizabeth A. Buffalo, Pascal Fries, Rogier Landman, Timothy J. Buschman, Robert Desimone, Laminar differences in gamma and alpha coherence in the ventral stream, Proc. Natl. Acad. Sci. 108 (27) (2011) 11262–11267, Publisher: Proceedings of the National Academy of Sciences.
[189] Eelke Spaak, Mathilde Bonnefond, Alexander Maier, David A. Leopold, Ole Jensen, Layer-specific entrainment of gamma-band neural activity by the alpha rhythm in monkey visual cortex, Curr. Biology : CB 22 (24) (2012) 2313.
[190] Roberto C. Sotero, Aleksandra Bortel, Shmuel Naaman, Victor M. Mocanu, Pascal Kropf, Martin Y. Villeneuve, Amir Shmuel, Laminar distribution of phase-amplitude coupling of spontaneous current sources and sinks, Front. Neurosci. 9 (2015).
[191] Roser Sanchez-Todo, Borja Mercadal, Edmundo Lopez-Sola, Maria Guasch-Morgades, Gustavo Deco, Giulio Ruffini, Fast interneuron dysfunction in laminar neural mass model reproduces Alzheimer's oscillatory biomarkers, Hum. Brain Mapp. 47 (1) (2026) e70428.
[192] Jan C. Gendra, Edmundo López-Solà, Francesca Castaldo, Èlia Lleal-Custey, Roser Sanchez-Todo, Jakub Vohryzek, Ricardo Salvador, Ralph G. Andrzejak, Giulio Ruffini, Alzheimer's Disease Neuroimaging Initiative, Restoring oscillatory dynamics in Alzheimer's disease: a laminar whole-brain model of serotonergic psychedelic effects, Netw. Neurosci. 10 (2) (2026) 303–328.
[193] Borja Mercadal, Finn Möller, Bernadette C.M. van Wijk, Gustavo Deco, et al., A biologically grounded model for cooperative and competitive interactions in the brain, BioRxiv (2025) preprint; PING nodes in whole-brain networks.
[194] Giulio Ruffini, Edmundo Lopez-Sola, Raul Palma, Roser Sanchez-Todo, Jakub Vohryzek, Francesca Castaldo, Karl Friston, Cross-Frequency Coupling as a Neural Substrate for Prediction Error Evaluation: A Laminar Neural Mass Modeling Approach, BioRxiv (2025) 2003–2025, Publisher: Cold Spring Harbor Laboratory.
[195] FH Lopes da Silva, A Hoek, H Smits, LH (1974) Kyber-netik 15: Zetterberg, Model of brain rhythmic activity: the alpha rhythm of the thalamus, Kybernetik 15 (1) (1974) 27–37.
[196] FH Lopes da Silva, van Rotterdam A, P Barts, E Heusden, W van Burr, Model of neuronal populations: the basic mechanism of rhythmicity, Prog Brain Res 45 (1976).
[197] B.H. Jansen, V.G. Rit, Electroencephalogram and visual evoked potential generation in a mathematical model of coupled cortical columns, Biol. Cybernet. 73 (4) (1995) 357–366.
[198] F. Wendling, F. Bartolomei, J.J. Bellanger, P. Chauvel, Epileptic fast activity can be explained by a model of impaired GABAergic dendritic inhibition, Eur. J. Neurosci. 15 (9) (2002) 508–1499.
[199] Giulio Ruffini, Fabrice Wendling, Roser Sanchez-Todo, Emiliano Santarnecchi, Targeting brain networks with multichannel transcranial current stimulation (tCS), Curr. Opin. Biomed. Eng. (2018).
[200] R Sanchez-Todo, R Salvador, E Santarnecchi, F Wendling, G Deco, G Ruffini, Personalization of hybrid brain models from neuroimaging and electrophysiology data, 2018, Publication Title: bioRxiv Publisher: bioRxiv.
[201] Roser Sanchez-Todo, Edmundo Lopez Sola, Ricardo Salvador, Maria Chiara Biagi, Gustavo Deco, Giulio Ruffini, TH-230. Mechanistic understanding of Alzheimer's disease through hybrid brain models: from mesoscale to macroscale, and design of personalized stimulation protocols, Clin. Neurophysiol. 141 (2022) S158, Publisher: Elsevier.
[202] Joana Cabral, Francesca Castaldo, Jakub Vohryzek, Vladimir Litvak, Christian Bick, Renaud Lambiotte, Karl Friston, Morten L. Kringelbach, Gustavo Deco, Metastable oscillatory modes emerge from synchronization in the brain spacetime connectome, Commun. Phys. 5 (1) (2022) 1–13, Publisher: Nature Publishing Group.
[203] Gustavo Deco, Josephine Cruzat, Joana Cabral, Enzo Tagliazucchi, Helmut Laufs, Nikos K Logothetis, Morten L Kringelbach, Awakening: Predicting external stimulation to force transitions between different brain states, Proc. Natl. Acad. Sci. USA 116 (36) (2019) 18088–18097, Publisher: Proceedings of the National Academy of Sciences.
[204] A. Destexhe, Z.F. Mainen, T.J. Sejnowski, in: C. Koch, I. Segev (Eds.), Kinetic Models of Synaptic Transmission, second ed., MIT Press, Cambridge, MA., 1998, pp. 1–25.
[205] Jurgis Pods, Johannes Schönke, Peter Bastian, Electrodiffusion models of neurons and extracellular space using the Poisson-nernst-Planck equations—Numerical simulation of the intra- and extracellular potential for an axon model, Biophys. J. 105 (2013) 242–254.
[206] W.J. Freeman, Mass Action in the Nervous System, Academic Press, New York, 1975.
[207] Leslie M. Kay, The physiological foresight in Freeman's work, J Conscious Stud. 25 (1–2) (2018) 50–63.
[208] F.H. Eeckman, Freemanm W.J., Asymmetric sigmoid non-linearity in the rat olfactory system, Brain Res. 557 (1–2) (1991) 13–21.
[209] Federico Devalle, Alex Roxin, Ernest Montbrió, Firing rate equations require a spike synchrony mechanism to correctly describe fast oscillations in inhibitory networks, PLoS Comput. Biol. 13 (12) (2017).

[210] Giulio Ruffini, Analysis and extension of exact mean-field theory with dynamic synaptic currents, 2022, Pages: 2021.09.01.458563 Section: New Results.
[211] Pau Clusella, Elif Köksal-Ersöz, Jordi Garcia-Ojalvo, Giulio Ruffini, Comparison between an exact and a heuristic neural mass model with second-order synapses, Biol. Cybernet. 117 (1–2) (2023) 5–19, Publisher: Springer Science and Business Media LLC.
[212] Leo P. Kadanoff, Scaling laws for ising models near {T}_{c}, Phys. Phys. Fiz. 2 (6) (1966) 263–272, Publisher: American Physical Society.
[213] Kenneth G. Wilson, The renormalization group: Critical phenomena and the Kondo problem, Rev. Modern Phys. 47 (4) (1975) 773–840.
[214] Leenoy Meshulam, Coarse graining, fixed points, and scaling in a large population of neurons, Phys. Rev. Lett. 123 (17) (2019).
[215] D.Q. Nykamp, D. Tranchina, A population density approach that facilitates large-scale modeling of neural networks: analysis and an application to orientation tuning, J. Comput. Neurosci. 8 (1) (2000) 19–50.
[216] A. Omurtag, B.W. Knight, L. Sirovich, Dynamics of neuronal populations: The equilibrium solution, SIAM J. Appl. Math. 60 (6) (2000) 2009–2028, Publisher: Society for Industrial and Applied Mathematics.
[217] Michael A. Buice, Jack D. Cowan, Carson C. Chow, Systematic fluctuation expansion for neural network activity equations, Neural Comput. 22 (2) (2010) 377–426.
[218] Ernest Montbrió, Diego Pazó, Alex Roxin, Macroscopic description for networks of spiking neurons, Phys. Rev. X 5 (2) (2015) 021028, Publisher: American Physical Society.
[219] Stephen Coombes, Áine Byrne, Next generation neural mass models, in: Fernando Corinto, Alessandro Torcini (Eds.), Nonlinear Dynamics in Computational Neuroscience, Springer International Publishing, Cham, 2019, pp. 1–16.
[220] Áine Byrne, Reuben D. O'Dea, Michael Forrester, James Ross, Stephen Coombes, Next-generation neural mass and field modeling, J. Neurophysiol. 123 (2) (2020) 726–742, Publisher: American Physiological Society.
[221] Stephen Coombes, Next generation neural population models, Front. Appl. Math. Stat. 9 (2023) Publisher: Frontiers.
[222] Christian Bick, Marc Goodfellow, Carlo R. Laing, Erik A. Martens, Understanding the dynamics of biological and neural oscillator networks through exact mean-field reductions: a review, J. Math. Neurosci. 10 (1) (2020) 9.
[223] Áine Byrne, Reuben D. O'Dea, Michael Forrester, James Ross, Stephen Coombes, Next-generation neural mass and field modeling, J. Neurophysiol. 123 (2) (2020) 726–742.
[224] Halgurd Taher, Alessandro Torcini, Simona Olmi, Exact neural mass model for synaptic-based working memory, PLoS Comput. Biol. 16 (12) (2020) e1008533, Publisher: Public Library of Science.
[225] Aman S. Aberra, Angel V. Peterchev, Warren M. Grill, Biophysically realistic neuron models for simulation of cortical stimulation, J. Neural Eng. 15 (6) (2018) 066023.
[226] Adriá Galan, Realistic Modeling of Neocortical Neurons and Electric Field Effects Under Direct Current Stimulation, (Master's thesis), Elite Master Program in Neuroengineering, Department of Electrical and Computer Engineering, Technical University of Munich, 2021.
[227] Grégory Dumont, Boris Gutkin, Macroscopic phase resetting-curves determine oscillatory coherence and signal transfer in inter-coupled neural circuits, PLoS Comput. Biol. 15 (6) (2019).
[228] Hongjie Bi, Marco Segneri, Matteo di Volo, Alessandro Torcini, Coexistence of fast and slow gamma oscillations in one population of inhibitory spiking neurons, Phys. Rev. Res. 2 (2020) 013042.
[229] Pau Clusella, Gustavo Deco, Morten L. Kringelbach, Giulio Ruffini, Jordi Garcia-Ojalvo, Complex spatiotemporal oscillations emerge from transverse instabilities in large-scale brain networks, PLoS Comput. Biol. 19 (4) (2023) e1010781, Publisher: Public Library of Science.
[230] Marco Segneri, Hongjie Bi, Simona Olmi, Alessandro Torcini, Theta-Nested Gamma oscillations in next generation neural mass models, Front. Comput. Neurosci. 14 (2020) 47.
[231] Gemma Reyner-Parra, Phase-locking patterns underlying effective communication in exact firing rate models of neural networks, PLoS Comput. Biol. 18 (5) (2022) 1–41.
[232] Ana Mayora-Cebollero, Roberto Barrio, Lin Li, Carmen Mayora-Cebollero, Lourdes Pérez, Dynamics of coupled neural populations: The role of synaptic dynamics, Chaos: An Interdiscip. J. Nonlinear Sci. 35 (6) (2025) 063140.
[233] Moritz Gerster, Halgurd Taher, Antonín Škoch, Jaroslav Hlinka, Maxime Guye, Fabrice Bartolomei, Viktor Jirsa, Anna Zakharova, Simona Olmi, Patient-specific network connectivity combined with a next generation neural mass model to test clinical hypothesis of seizure propagation, Front. Syst. Neurosci. 15 (2021) 675272.
[234] Giovanni Rabuffo, Jan Fousek, Christophe Bernard, Viktor Jirsa, Neuronal cascades shape whole-brain functional dynamics at rest, ENeuro 8 (5) (2021) ENEURO.0283–21.2021.
[235] Yonatan Sanz Perl, Sebastian Geli, Eider Pérez-Ordoyo, Lou Zonca, Sebastian Idesis, Jakub Vohryzek, Viktor K. Jirsa, Morten L. Kringelbach, Enzo Tagliazucchi, Gustavo Deco, Whole-brain modelling of low-dimensional manifold modes reveals organising principle of brain dynamics, 2023, Pages: 2023.11.20.567824 Section: New Results.
[236] Michael Forrester, Sammy Petros, Oliver Cattell, Yi Ming Lai, Reuben D. O'Dea, Stamatios Sotiropoulos, Stephen Coombes, Whole brain functional connectivity: Insights from next generation neural mass modelling incorporating electrical synapses, PLoS Comput. Biol. 20 (12) (2024) e1012647.
[237] Rosa Maria Delicado-Moll, Gemma Huguet, Pau Clusella, Emergent spatiotemporal dynamics in large-scale brain networks with next generation neural mass models, Phys. D: Nonlinear Phenom. 493 (2026) 135232.
[238] Áine Byrne, James Ross, Rachel Nicks, Stephen Coombes, Mean-field models for EEG/MEG: from oscillations to waves, Brain Topogr. 35 (1) (2022) 36–53.
[239] Helmut Schmidt, Daniele Avitabile, Ernest Montbrió, Alex Roxin, Network mechanisms underlying the role of oscillations in cognitive tasks, PLoS Comput. Biol. 14 (9) (2018) 1–24.
[240] Halgurd Taher, Alessandro Torcini, Simona Olmi, Exact neural mass model for synaptic-based working memory, PLoS Comput. Biol. 16 (12) (2020) e1008533.
[241] David Depannemaecker, colleagues, A next generation neural mass model with neuromodulation, BioRxiv (2024) preprint.
[242] Liang Chen, Sue Ann Campbell, Exact mean-field models for spiking neural networks with adaptation, J. Comput. Neurosci. 50 (4) (2022) 445–469.
[243] Pau Clusella, Ernest Montbrió, Exact low-dimensional description for fast neural oscillations with low firing rates, Phys. Rev. E 109 (1) (2024) 014229.
[244] Denis S. Goldobin, Matteo di Volo, Alessandro Torcini, Reduction methodology for fluctuation driven population dynamics, Phys. Rev. Lett. 127 (2021) 038301.
[245] Denis S. Goldobin, Mean-field models of populations of quadratic integrate-and-fire neurons with noise on the basis of the circular cumulant approach, Chaos: An Interdiscip. J. Nonlinear Sci. 31 (8) (2021) 083112.
[246] Viktoras Pyragas, Kestutis Pyragas, Mean-field equations for neural populations with q-Gaussian heterogeneities, Phys. Rev. E 105 (2022) 044402.
[247] Viktoras Pyragas, Kestutis Pyragas, Mean-field models of neural populations with Gaussian noise and non-Cauchy heterogeneities, Phys. Rev. E 110 (2024) 064211.

[248] Ernest Montbrió, Diego Pazó, Exact mean-field theory explains the dual role of electrical synapses in collective synchronization, Phys. Rev. Lett. 125 (248101) (2020).
[249] Liang Chen, Sue Ann Campbell, Exact mean-field models for spiking neural networks with adaptation, J. Comput. Neurosci. 50 (4) (2022) 445–469.
[250] Alberto Ferrara, David Angulo-Garcia, Alessandro Torcini, Simona Olmi, Population spiking and bursting in next-generation neural masses with spike-frequency adaptation, Phys. Rev. E 107 (2) (2023) 024311.
[251] Bastian Pietras, Pau Clusella, Ernest Montbrió, Low-dimensional model for adaptive networks of spiking neurons, Phys. Rev. E 111 (2025) 014422.
[252] Wilten Nicola, Sue Ann Campbell, Mean-field models for heterogeneous networks of two-dimensional integrate and fire neurons, Front. Comput. Neurosci. 7 (2013) 184.
[253] Edward Ott, Thomas M. Antonsen, Low dimensional behavior of large systems of globally coupled oscillators, Chaos: An Interdiscip. J. Nonlinear Sci. 18 (3) (2008) 037113.
[254] Bastian Pietras, Rok Cestnik, Arkady Pikovsky, Exact finite-dimensional description for networks of globally coupled spiking neurons, Phys. Rev. E 107 (2023) 024315.
[255] Ernest Montbrió, Diego Pazó, Exact mean-field theory explains the dual role of electrical synapses in collective synchronization, Phys. Rev. Lett. 125 (24) (2020) 248101.
[256] Rok Cestnik, Two-phase quadratic integrate-and-fire neurons: Exact low-dimensional description for ensembles of finite-voltage neurons, Phys. Rev. Res. 8 (1) (2026) L012049.
[257] John D. Griffiths, Sorenza P. Bastiaens, Neda Kaboodvand, Computational modelling of the brain: Modelling approaches to cells, circuits and networks, in: Computational Modelling of the Brain, in: Advances in Experimental Medicine and Biology, vol. 1359, Springer, 2021, pp. 313–355.
[258] Jorge F. Mejias, John D. Murray, Henry Kennedy, Xiao-Jing Wang, Feedforward and feedback frequency-dependent interactions in a large-scale laminar network of the primate cortex, Sci. Adv. 2 (11) (2016) e1601335.
[259] Ryan V Raut, Anish Mitra, Scott Marek, Mario Ortega, Abraham Z Snyder, Aaron Tanenbaum, Timothy O Laumann, Nico U F Dosenbach, Marcus E Raichle, Organization of propagated intrinsic brain activity in individual humans, Cerebral Cortex 30 (3) (2020-03-14) 1716–1734.
[260] Andre M. Bastos, W. Martin Usrey, Rick A. Adams, George R. Mangun, Pascal Fries, Karl J. Friston, Canonical microcircuits for predictive coding, Neuron 76 (4) (2012) 695.
[261] Karl Friston, The free-energy principle: a unified brain theory? Nature Rev. Neurosci. 11 (2) (2010) 127–138, Publisher: Springer Science and Business Media LLC.
[262] Matthew F. Glasser, Timothy S. Coalson, Emma C. Robinson, Carl D. Hacker, John Harwell, Essa Yacoub, Kamil Ugurbil, Jesper Andersson, Christian F. Beckmann, Mark Jenkinson, Stephen M. Smith, David C. Van Essen, A multi-modal parcellation of human cerebral cortex, Nature 536 (7615) (2016) 171–178.
[263] Morten L Kringelbach, Josephine Cruzat, Joana Cabral, Gitte Moos Knudsen, Robin Carhart-Harris, Peter C Whybrow, Nikos K Logothetis, Gustavo Deco, Dynamic coupling of whole-brain neuronal and neurotransmitter systems, Proc. Natl. Acad. Sci. 117 (17) (2020) 9566–9576, Publisher: National Acad Sciences.
[264] Rodrigo Cofré, Rubén Herzog, Pedro A.M. Mediano, Juan Piccinini, Fernando E. Rosas, Yonatan Sanz Perl, Enzo Tagliazucchi, Whole-Brain models to explore altered states of consciousness from the bottom up, Brain Sci. 10 (9) (2020) 626.
[265] Murat Demirtaş, Joshua B. Burt, Markus Helmer, Jie Lisa Ji, Brendan D. Adkinson, Matthew F. Glasser, David C. Van Essen, Stamatios N. Sotiropoulos, Alan Anticevic, John D. Murray, Hierarchical heterogeneity across human cortex shapes large-scale neural dynamics, Neuron 101 (6) (2019) 1181–1194.e13, Publisher: Elsevier.
[266] Joshua B. Burt, Murat Demirtaş, William J. Eckner, Natasha M. Navejar, Jie Lisa Ji, William J. Martin, Alberto Bernacchia, Alan Anticevic, John D. Murray, Hierarchy of transcriptomic specialization across human cortex captured by structural neuroimaging topography, Nature Neurosci. 21 (9) (2018) 1251–1259, Publisher: Nature Publishing Group.
[267] Eve Marder, Neuromodulation of Neuronal Circuits: Back to the Future, Neuron 76 (1) (2012) 1–11, Publisher: Elsevier.
[268] Gustavo Deco, Yonatan Sanz Perl, Jakub Vohryzek, Andrea Luppi, Morten L. Kringelbach, Evolution's boldest trick: Neurotransmission modulated whole-brain computation captures full task repertoire, 2025, Pages: 2025.06.02.657368 Section: New Results.
[269] Giulio Ruffini, Francesca Castaldo, Edmundo Lopez-Sola, Roser Sanchez-Todo, Jakub Vohryzek, The algorithmic agent perspective and computational neuropsychiatry: From etiology to advanced therapy in major depressive disorder, Entropy 26 (11) (2024) 953, Number: 11 Publisher: Multidisciplinary Digital Publishing Institute.